Implementing dynamic boundary conditions with the material point method

Do Chinh Phuong

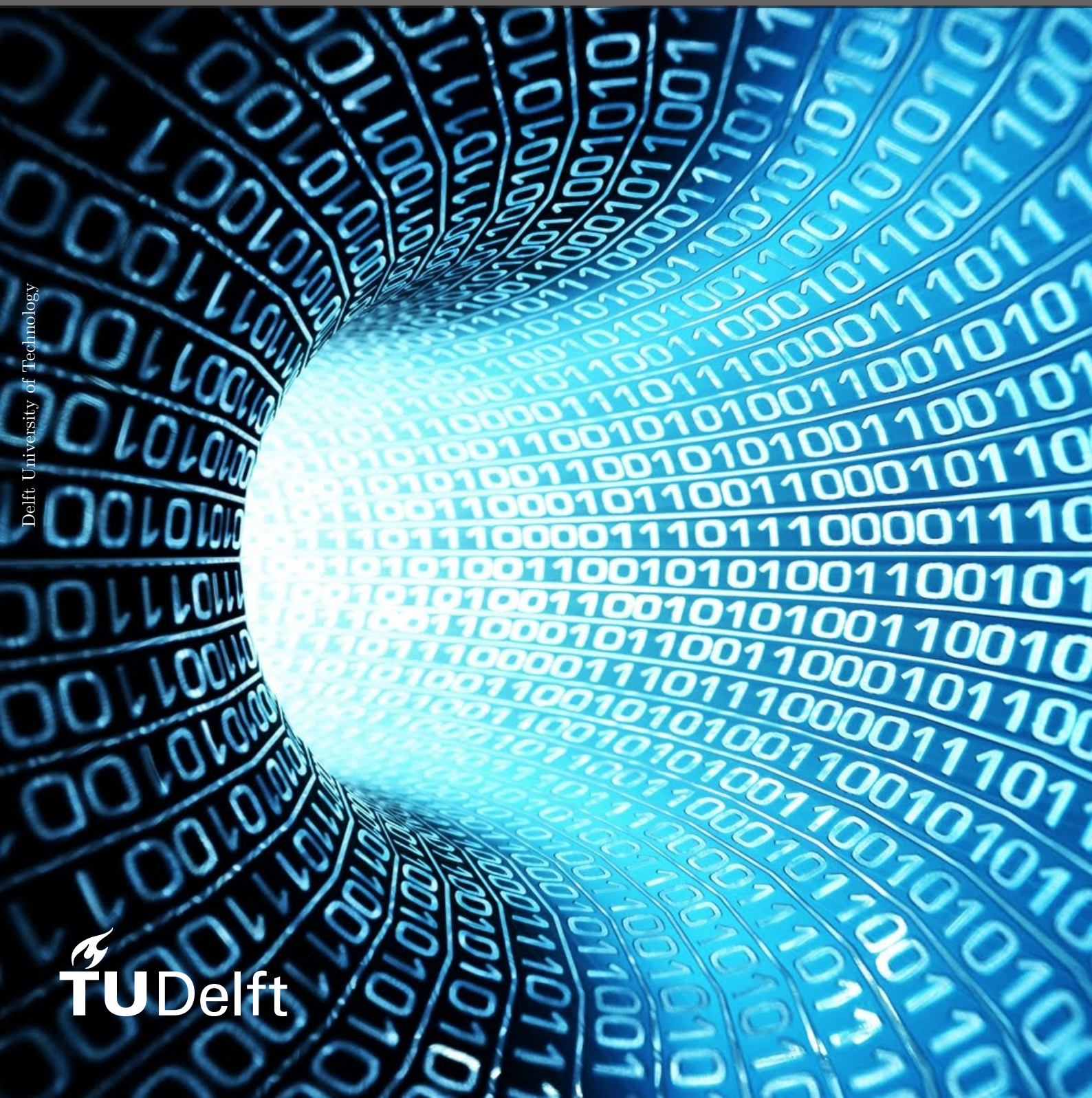

Delft University of Technology

TU Delft

Implementing dynamic boundary conditions with the material point method

by

Do Chinh Phuong

in partial fulfillment of the requirements for the degree of

Master of Science
in Civil Engineering

at the Delft University of Technology,
to be defended publicly on Thursday December 9, 2021 at 03:00 PM

Student number:	5156319
Institution:	Delft University of Technology
Faculty:	Faculty of Civil Engineering and Geosciences

Thesis committee:

Professor of Soil Mechanics Michal A. Hicks (Chairman)
Section Head of Geo-Engineering, Department of Geosciences and Engineering

Associate Professor Philip J. Vardon
Section Geo-Engineering, Department of Geosciences and Engineering

Assistant Professor in Offshore Soil Mechanics Federico Pisanò
Section of Geo-Engineering, Department of Geosciences and Engineering

Doctor of Philosophy José León González Acosta
Section Geo-Engineering, Department of Geosciences and Engineering

TU Delft

Preface

This master thesis was written as a completion of my Master track in Geo-Engineering at Delft University of Technology. During my time as a Master student, I have not only gained solid theoretical background in civil engineering, but also firmly developed my mentality to evaluate and solve encountered problems as an engineer.

I have had the opportunity to explore many interesting and challenging topics, but working with numerical analyses, especially the material point method, was and still is extremely exciting for me. From the first day I started my thesis to the end, I was fascinated by all the ideas and equations that together form the basis of the method. The journey has taught me the value of staying ambitious with my work and persevering through all the mistakes I made and the ideas that did not work out. I have enjoyed it till the very last bit.

It is impossible for me to finish the thesis without the presence of my supervisors. I want to thank Professor Michael Hicks for your patience and time to guide me whenever I needed. I would like to thank Professor Phil Vardon for your valuable comments, for always pushing me to my full potential. Of course, I could never neglect to thank Dr. León González for always being on my side. I treasure every online meeting we had, and every moment we discussed the work at the university. Finally I would like to thank Professor Federico Pisanò, for your productive feedback during our meetings. Last but not least, from the depth of my heart, I cannot describe how grateful I am to have been your student. Thank you for everything.

To my beloved friends, our dinners and meetings have given me energy and love that I will never forget. We may be separated, but your voices will echo in my heart forever. To my parents, family and my sweetheart, you have always been my cornerstones, unconditionally, through thick and thin.

Do Chinh Phuong
Delft, December 2021

"*Our greatest glory is not in never falling, but in rising every time we fall*" — Confucius

Abstract

The material point method (MPM) is gaining increasing amounts of attention due to its capacity to solve geotechnical problems involving large-deformations. While some problems require dynamic analysis, simulating the (infinite) continuous domain using typical Dirichlet (fixed) boundary conditions induce spurious reflections causing (1) unrealistic stress increments at the domain boundary and (2) the appearance of multiple unnatural stress waves in the domain. Aiming to eliminate this numerical artifact in MPM, two solutions for absorbing boundary conditions found in FEM are implemented and investigated; these are (1) a viscous boundary condition and (2) a viscoelastic boundary condition. The use of such dynamic boundary conditions in MPM is scarce and no validation of them has yet been presented in the literature. In this work, these absorbing conditions are implemented alongside other recent developments, which improves the numerical stability (Double-Mapping, Generalized Material Point Method, Composite Material Point Method), using two approaches: (1) directly imposing at the external active boundary nodes and (2) imposing via shape function interpolation. The proposed solutions are then validated with a one-dimensional benchmark: a soil column under dynamic load in small-deformation and large-deformation, and a 2D symmetric plane strain model under one loading pulse. The benchmark results demonstrate that the numerical reflections that lead to inaccuracies of stress and velocity can be removed using GIMP interpolation and, together with the other numerical technics, render high-quality and realistic results. A study of shallow foundation failure under repeated loading is also presented, showing the potential of applications of the proposed solution for modelling extreme geotechnical events.

Contents

Nomenclature

Latin symbols

In tables and lists, tensors are noted in bold, scalars are noted in regular font.

A	Domain area
A_{bound}	Boundary area of a node/material point
a	Viscous boundary coefficient
$\{\mathbf{a}\}$	Acceleration vector
$\{\bar{\mathbf{a}}\}$	Nodal acceleration vector
$\bar{a}_i^t$	Nodal acceleration of node i
$\bar{a}_p^t$	Material point's acceleration
b	Viscous boundary coefficient
$bmps$	Number of boundary material points
$\boldsymbol{b}$	Body force tensor
$[\mathbf{B}]$	Integration matrix
$[\mathbf{B}_{ip}]$	Integration matrix with GIMP shape function
$[\boldsymbol{C}]$	Wave-velocity matrix
C_p	Compressional wave velocity
C_s	Dilational wave velocity
c_p	Peak cohesion
c_r	Residual cohesion
Δx	Discretised element size
Δt	Time step
$[\mathbf{D}]$	Constitutive elastic matrix of the material
$[\mathbf{D}_i]$	Elastic matrix of node i
$[\mathbf{D}_p]$	Elastic matrix of material point p
$[\mathbf{D}_g]$	Elastic matrix computed at Gauss's locations
$\{\Delta\bar{\boldsymbol{u}}\}^{ext}$	Nodal displacement vector in the extended domain
E	Young's modulus
$\{\mathbf{F}\}_{ext}$	External force vector
$\{\mathbf{F}\}_{int}$	Internal force vector
$\{\mathbf{F}\}_{kin}$	Kinematic force vector
$\{\mathbf{F}\}_{spring}$	Boundary spring force vector computed using interpolation of shape functions
$\{\mathbf{F}\}_{vis}$	Boundary viscous force vector computed using interpolation of shape functions
f	Displacement solution (reflected)
$\{\mathbf{f}\}_{spring}$	Boundary spring force vector imposing at boundary nodes
$\{\mathbf{f}\}_{vis}$	Boundary viscous force vector imposing at boundary nodes
$\{\mathbf{f}\}^{viscoe}$	Viscoelastic force vector
G	Shear modulus
g	Displacement solution (transmitted)
H	Softening modulus
$\lvert J\rvert$	Determinant of the Jacobian
$[\mathbf{K}]$	Global stiffness matrix
K_n	Normal spring stiffness of the viscoelastic boundary
K_s	Tangential spring stiffness of the viscoelastic boundary
$[\mathbf{K}]_{spring}]$	Boundary spring stiffness matrix using interpolation with shape functions
$[\mathbf{K}]_{vis}$	Boundary viscous stiffness matrix using interpolation with shape functions
k	Newton-Raphson iteration subscript
$[\mathbf{k}]_{spring}$	Boundary spring stiffness matrix imposing at the boundary nodes
$[\mathbf{k}]_{vis}$	Boundary viscous stiffness matrix imposing at the boundary nodes
l_i	Boundary area of node i

l_p	A half of material point support domain
$\mathbf{m}_{ij}$	Mass matrix component of row i column j
$[\mathbf{m}]$	Global consistent mass matrix
N	Normal force
n	Number of nodes in the extended domain
N^2	Composite material point shape function value
N_j^2	CMPM shape function value at node j
∇N^2	CMPM shape function gradient matrix
∇N_i	linear shape function gradient
∇S_{ip}	GIMP shape function gradient
nbn	Number of boundary nodes
$[\boldsymbol{N}]$	Shape function matrix
$ngauss$	Number of Gauss's integration points
N_i	Shape function value at node i
$N_i(x_g)$	Shape function value at node i computed with Gauss's coordinate
$nmps$	Number of material points
nn	Number of nodes
nstatic	Number of static steps
ngrastep	Number of incremental gravitation steps
r_b	Distance from boundary to the source of excitation
S_{ip}^*	Local GIMP shape function value
S_{ip}	GIMP shape function value
$\boldsymbol{S}_{ip}(j)$	1D GIMP shape function in the direction j
smp	Number of material points having support domain inside the element
$\{\boldsymbol{s^s}\}$	Traction
$[\boldsymbol{T}]$	Transformation matrix
t	Configuration at time t
tol	Tolerance value
$\{\Delta\bar{\mathbf{u}}\}$	Incremental nodal displacement vector
$\{\bar{\mathbf{u}}\}$	Nodal displacement vector
u_i	Nodal displacement of node i
$\{\mathbf{u_{n,s}}\}$	Displacement matrix in normal and tangential direction
$\{\mathbf{u_{x,y}}\}$	Displacement matrix in Cartesian coordinate system
u_{xi}	Horizontal displacement value of node i
u_{yi}	Vertical displacement value of node i
$\mathbf{v}$	Velocity tensor
$\{\bar{\mathbf{v}}\}$	Nodal velocity vector
V	Volume
v_n	Particle's velocity in normal direction
$\{\mathbf{v_{n,s}}\}$	Velocity matrix in normal and tangential direction
$\{\mathbf{v_{x,y}}\}$	Velocity matrix in Cartesian coordinate system
V_p	Material point's volume
v_p	Material point velocity
v_s	Particle's velocity in tangential direction
W^*	Modified weight of material point
W^{Gauss}	Gauss's residual weight
W_p	Material point weight
x_g	Gauss's integration point coordinate
x_i	Nodal coordinate
x_{ip}	Distance between material point p and node i
$[x_p]$	Nodal coordinates matrix
x_p	Material point's location
$Y[\sigma_p]$	Yield function of a material point with given stress state

Greek symbols

χ_p	Activation function of material point support domain
$[\Delta\boldsymbol{\sigma}]$	Incremental stress tensor
η	Vertical local coordinate
$\{\boldsymbol{\varepsilon}\}$	Strain increment vector
$\bar{\varepsilon}_p$	Plastic invariant
Γ	Boundary
ν	Poisson's ration
omp	Number of original material points inside the element
Ω	Domain of element
Ω_p	Material point's support domain
ρ	Soil density
ρ_p	Soil density of the material point p
$\boldsymbol{\sigma}$	Cauchy stress tensor
$[\boldsymbol{\sigma}_0]$	Initial stress matrix
$[\boldsymbol{\sigma}_p]$	Stress tensor of the material point p
$[\boldsymbol{\sigma}_p]^{dyn}$	Dynamic stress state tensor
$[\boldsymbol{\sigma}_p]^{ini}$	Initial stress state tensor
$[\boldsymbol{\sigma}_p]_{k+1}^{trial}$	Trial stress tensor of the material point
τ	Shear stress
ξ	Horizontal local coordinate in an element
ξ_m	Local coordinate of remaining node to compute CMPM shape function
ξ_j	Local coordinate of the CMPM shape function

List of acronyms

CMPM	Composite Material Point Method
DBC	Dynamic boundary condition
DM	Double-Mapping
DM-GC	Double Mapping with GIMP and CMPM
FEM	Finite Element Method
GIMP	Generalized Interpolation Material Point Method
MPM	Material Point Method

List of Figures

List of Tables

1 Introduction

1.1. Material Point Method and large-deformation

For many years, the finite element method (FEM) has dominated the computational analysis of structures and solid mechanics. A vast specialisation under the umbrella of the mechanical engineering discipline commonly integrates FEM in the design and development processes, including the geotechnical aspect. However, since the method is purely based on the concept of the Lagrangian description, in which the geometry of the problem is attached to the mesh, any large-deformation will cause computations to not be able to finish. Attempting to overcome this issue, Sulsky et al. (1994a, 1995) have combined both the Lagrangian and the Eulerian approaches with the material point method (MPM). With MPM's discretisation, two meshes are defined: (1) the Eulerian mesh served as the background mesh and (2) the spatial or Lagrangian mesh which defines a set of material points (or particles) covering the domain of interest. Since the Eulerian mesh can freely moved, the mesh distortion problem is well avoided compared to FEM. This benefit allows the use of MPM to simulate extreme geotechnical events which relate to large-deformation such as: explosions (Zhang. et al., 2009), screwpile installation (Wang et al., 2017), landfill settlement (Zhou et al., 1999), slope failure (Bhandari et al., 2016, Wang and Hicks, 2016, Wang and Vardon, 2016), CPT installation (Ceccato et al., 2016) or ice movement (Sulsky et al., 2007).

Despite MPM's advantages, the method's computation cost is highly expensive as large storage is required to save particle and mesh data. Moreover, its accuracy particularly in the stress field is far from the desired level. This problem is commonly addressed as stress oscillations and stress inaccuracies, mostly due to the use of discontinuous finite element shape functions (or the choose of basis functions) and shape function gradients (Bardenhagen et al. (2000), Gonzalez Acosta et al. (2020), and Tielen et al. (2017)). In some publications, full results of the stresses are often not displayed, and only deformation or limited data is presented. Moreover, the majority of work presented in the literature so far can only use simple constitutive models which lead to the inability to capture complex behaviours that arises over the domain. Another common problem in MPM is that as the Eulerian particles displace over the background mesh, applying boundary conditions to moving surfaces is challenging. Therefore, further developments are required to improve MPM's accuracy.

1.2. Boundary conditions with dynamic analysis using MPM

Commonly in FEM and MPM, the computational domain is truncated using two types of boundary: free boundary and fixed boundary. This basic approach may give satisfactory results for quasi-static analysis, but it performs worse for problems involving propagation of waves or load. The problem is induced because these two boundaries are unable to represent the continuity and the radiation condition for dynamic waves to transmit through the boundary. Readers are directed to Lysmer and Kuhlemeyer (1969) for further reading. Many solutions are introduced in FEM (Basu and Chopra (2004), Clayton and Engquist (1977), Deeks and Randolph (1994), Liao and Wong (1984), Lysmer and Kuhlemeyer (1969), and Smith (1974)), but none of these applications in MPM can be found in the literature. Hence, to extend the applications of MPM to simulate large-deformation problems involving dynamic

loading, it is compulsory to have the boundary treated properly.

1.3. Problem statement

It is known that some of the most extreme events with large-deformation are commonly related to seismic loading to a porous medium. In order to accurately perform dynamic analyses, the boundary condition must be treated with care. A problem often encountered during dynamic simulations is that loading waves are unable to transmit smoothly at the numerical boundary. In other words, spurious reflection of waves generated due to incapability of constructing the radiation condition at the bounded domain can cause stress oscillation over time.

In conclusion, it is needed to improve the dynamic boundary setting of MPM during dynamic analyses.

1.4. Objectives

This thesis work is intended to derive the theoretical framework and algorithms for implementations of non-reflection boundaries into MPM. Nevertheless, these implementations should also consider the common drawback in MPM, i.e., stress oscillation and material points crossing elements. The main goal is to have the dynamic boundary implemented properly, while at the same time mitigating the stress oscillations problem.

Lastly, a study of a geotechnical problem will be simulated to compare the outcomes of the improved MPM frameworks with the conventional MPM ones.

1.5. Research questions

To make sure the objectives mentioned above can be achieved, a main research has been set:

"How can dynamic boundary conditions improve the accuracy of the material point method?"

This main question is separated into sub-questions, in order to answer it clearly. Finding appropriate dynamic boundary conditions is a must, then it is vital to have a proper modification of these conditions in MPM, as well validations of these proposed settings.

Why is the presence of dynamic boundary conditions necessary?

"Which boundary conditions can be implemented in MPM? How to implement them?"

"How to validate these implementations?"

"What can be done to improve the implementations?"

1.6. Thesis outline

This section presents the outline of the thesis report:

1. **Chapter 1: Introduction** gives the overview tasks, the main questions which are going to be answered.
2. In **Chapter 2: Theoretical background**, the MPM framework will be described in detail.
3. **Chapter 3: Wave-absorbing boundaries** will discuss some of the most used wave-transmitting conditions, to give a short overview about these conditions. Based on this, implementation of the standard viscous boundary and the viscoelastic boundary into MPM is provided.
4. **Chapter 4: Benchmarks** validates the implementations with 2 benchmarks. The first one is a 1D soil column under dynamic loading, with small deformation and large deformation conditions. The second one is a 2D symmetrical plane strain model.
5. **Chapter 5: Study of a foundation under repeated loading with implicit MPM** applies the proposed solutions to study the geotechnical examples, in order to verify its applications
6. **Chapter 6: Conclusions and Recommendations** is where the research questions are answered. Summaries of the main conclusions of the thesis and recommendations for further studies are provided.

2

MPM Background

The Material Point Method introduced by Sulsky et al. (1994a, 1995) can be considered as the evolution of the Particle - In - Cell Method (PIC) (Buneman (1959), Dawson (1962), Harlow (1964)) and the Fluid Implicit Particle (FLIP) method (Brackbill, 1986). PIC method is originally made for usage in computational fluid mechanics, with the interpolation between the mesh and particles resulting in a part of the state variables stored in the grid and the rest ascribed to the particles. Later development has improved the numerical diffusion with the introduction of the FLIP method (Brackbill et al., 1988). While these particle methods are suited for fluid mechanics, MPM appeared to be advantageous in solid mechanics after it was released with the ability of storing state variable data on particles. Similar to FEM, MPM also utilizes an Eulerian mesh to solve equations of equilibrium, while a set of Lagrangian particles represents the physical shape of the simulated body and contains its inherent properties. Serving as the temporary step to solve equations of motion, the background grid therefore carries no permanent information and will be reset to its initial configuration at the end of each calculation step, while the solution is updated to each particle resulting in the convection of these points and the changes in state variables such as stress, velocity or displacement. Considering these aspects, MPM is advantageous in simulations of extreme geotechnical events in which the deformation occurs to be large, such as explosions (Wang et al., 2011; Zhang. et al., 2009), screwpile installation (Wang et al., 2017), slope failure (Bhandari et al., 2016, Wang and Vardon, 2016; Wang and Hicks, 2016), CPT installation (Ceccato et al., 2016) or ice movement (Sulsky et al., 2007).

Generally, explicit time integration is used due to its simplicity. This scheme is characterized by solving nodal accelerations as a primary state variable. The scheme uses forward Euler time integration technique to estimate the state of the domain at time $t + \Delta t$. In this formulation, small time steps are needed to avoid the divergence of the system and consistent matrices are not required (i.e. lumped matrices are used). This results in overall expensive computational cost.

Later, Sulsky et al. (1994b) developed an implicit dynamic solver in MPM, with a matrix-free implementation method. The method, however, requires improvements to make it capable to simulate complicated problems. A more straightforward implicit approach with adapted FEM implementation, was carried out by Guilkey and Weiss (2003), Wang et al. (2016), providing descriptions of assembling global matrices and iterative procedure. Since implicit time integration is unconditionally stable, larger time steps can be employed during simulation. Some works using the implicit MPM framework can be found in: the computational of multicellular constructs by Guilkey et al. (2006), improvement of implicit MPM by Buzzi et al. (2008), development of implicit contact MPM by Gonzalez Acosta et al. (2021) or study of slope stability by Wang and Vardon (2016). This implicit dynamic MPM with constructions of global matrices will be used as the starting point for this thesis' work.

2.1. Spatial discretisation

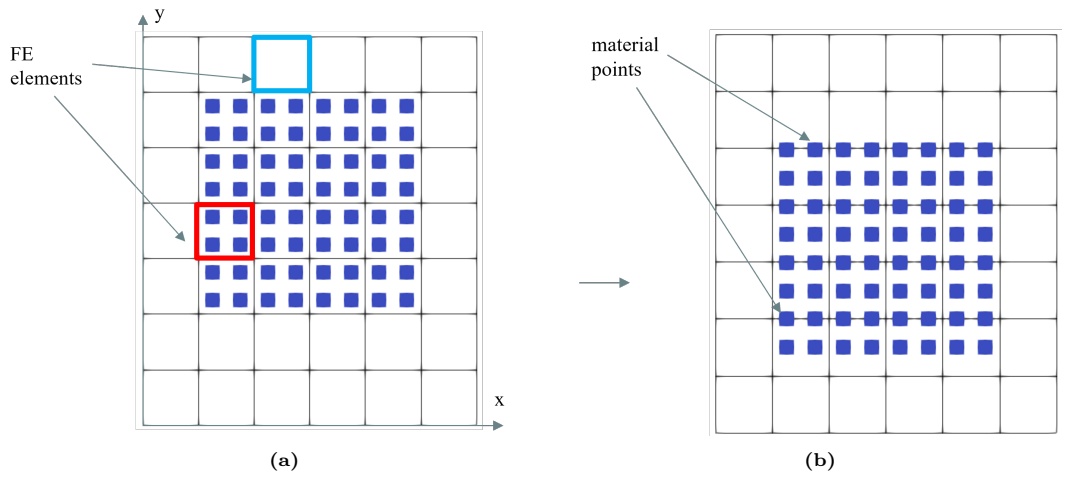

Figure 2.1: MPM discrestisation, a) initial configuration and b) configuration after solution phase

The MPM employs two set of discretisations: a set of material points representing the physical body and a background Eulerian mesh covering the entire computational space. Nevertheless, the MPM's background mesh can only use linear elements, because the use of non-linear elements with high order basis functions will result in the non-physical negative nodal mass, refer to Andersen and Andersen (2010) for further reading. In figure 2.1a, an example of background mesh with 4-node quadrilateral elements is shown. In the beginning of each time step, elements without particles are deactivated (shown as blue box), while state variables stored at material points (MPs) are interpolated and integrated to all nodes of the activated elements (indicated with the red box) which cover all the MPs, by using shape functions (SFs) and shape function gradients (SF gradients). Material points can move freely throughout the mesh, allowing the advection of state variables to the computational grid, as shown in figure 2.1b. This also means the list of activated and deactivated elements is often changed for each time step. In this thesis, a background mesh with four noded linear element with four material points initially placed inside each element with be used for simulations.

2.2. Continuum equations

The equations of motion are solved at the background grid similar to FEM where the material points serve as the Gauss integration points for the integration of global matrices. Even though, that the discrete form of equations of motion can be found in many sources, it is worth to review its derivation.

Considering a solid body with a volume V and a density ρ at an arbitrary configuration at time t. The conservation of mass in which the net change in mass density over time and the change of mass density over space should be equal to zero:

$$\frac{d\rho}{dt} + \rho\nabla.\mathbf{v} = 0 \tag{2.1}$$

where $\mathbf{v}$ is the velocity tensor subjected to the divergence operator ∇ and $\frac{d}{dt}$ designates the time derivative.

Equation (2.1) is implicitly satisfied considering the unchanged mass system. The conservation of linear momentum is expressed as:

$$\rho\frac{d\mathbf{v}}{dt} = \nabla.\boldsymbol{\sigma} + \rho\mathbf{b} \tag{2.2}$$

where $\mathbf{b}$ is the body force due to gravity and $\boldsymbol{\sigma}$ is the Cauchy stress tensor.

The stress-strain laws and incremental strain can be written as:

$$\{d\boldsymbol{\varepsilon}\} = \frac{1}{2}([\nabla\mathbf{u}] + [\nabla\mathbf{u}^T])dt \tag{2.3}$$

$$[d\boldsymbol{\sigma}] = [\mathbf{D}]\{d\boldsymbol{\varepsilon}\} \tag{2.4}$$

where $\{\boldsymbol{\varepsilon}\}$ is the strain increment vector, $[\mathbf{D}]$ represents the constitutive elastic matrix of the material, with plane strain analysis, which is defined as:

$$[\mathbf{D}] = \frac{E}{(1+\nu)(1-2\nu)} \begin{bmatrix} 1-\nu & \nu & 0 & \nu \\ \nu & 1-\nu & 0 & \nu \\ 0 & 0 & \frac{1-2\nu}{2} & 0 \\ \nu & \nu & 0 & 1-\nu \end{bmatrix} \tag{2.5}$$

where E is the Young's modulus and ν is the Poisson's ratio.

Rewriting equation (2.2) for the static equilibrium (i.e. neglecting the change in velocity over time) yields:

$$\nabla.\boldsymbol{\sigma} + \rho\mathbf{b} = 0 \tag{2.6}$$

Then, using the principle of virtual work, expressing that the difference between internal work and external work should be zero, together with the Gauss's divergence theorem, the weak from of equation (2.6) is obtained, similar to what has been shown in Griffiths (2004) and Bathe (2004):

$$\Pi = \frac{1}{2}\int_V \{\boldsymbol{\varepsilon}^T\}[\mathbf{D}]\{\boldsymbol{\varepsilon}\}dV - \left[\int_V \{\bar{\mathbf{u}}\}^T\rho\Big(\{\mathbf{b}\} - \{\mathbf{a}\}\Big)dV + \int_\Gamma \{\bar{\mathbf{u}}\}^T\{\boldsymbol{s}^{\boldsymbol{s}}\}d\Gamma\right] \tag{2.7}$$

where the inertia term (i.e. $\{\mathbf{a}\}$) is the acceleration vector included as part of body forces using D'Alembert's principle of internal forces, $\{\boldsymbol{s}^{\boldsymbol{s}}\}$ displays the traction applying at the boundaries and $\{\mathbf{b}\}$ is the body force, $\{\bar{\mathbf{u}}\}$ is the vector of nodal displacement and it is defined as:

$$\{\bar{\mathbf{u}}\} = \begin{Bmatrix} u_{x1} \\ u_{y1} \\ u_{x2} \\ u_{y2} \\ u_{x3} \\ u_{y3} \\ u_{x4} \\ u_{y4} \end{Bmatrix} \tag{2.8}$$

Internal force, body force (i.e. $\{\mathbf{b}\}$) and inertia force (i.e. $\{\mathbf{a}\}$) are integrated over the volume V of the domain while traction is integrated at the boundary Γ.

The test function (virtual displacements or strains) $\{\delta\bar{\mathbf{u}}\}$ and $\{\delta\boldsymbol{\varepsilon}\}$ are evaluated so that $\delta\Pi = 0$. Using what is shown by Davies (2011) (i.e. $\{\delta\boldsymbol{\varepsilon}^2\} = 2\{\boldsymbol{\varepsilon}\}\{\delta\boldsymbol{\varepsilon}\}$), equation (2.7) becomes:

$$\int_V \{\delta\boldsymbol{\varepsilon}^T\}[\mathbf{D}]\{\boldsymbol{\varepsilon}\}dV = \int_V \{\delta\mathbf{u}\}^T\rho\Big(\{\mathbf{b}\} - \{\mathbf{a}\}\Big)dV + \int_\Gamma \{\delta\mathbf{u}\}^T\{\boldsymbol{s}^{\boldsymbol{s}}\}d\Gamma \tag{2.9}$$

Using the strain-displacement relation $[\boldsymbol{\varepsilon}] = [\mathbf{B}]\{\bar{\mathbf{u}}\}$, where $[\mathbf{B}]$ is the integration matrix containing the derivatives of shape function. Considering quadratic four noded elements, the nodal and integration matrices are determined as follows:

$$[\mathbf{B}] = \begin{bmatrix} \frac{\partial N1}{\partial x} & 0 & \frac{\partial N2}{\partial x} & 0 & \frac{\partial N3}{\partial x} & 0 & \frac{\partial N4}{\partial x} & 0 \\ 0 & \frac{\partial N1}{\partial y} & 0 & \frac{\partial N2}{\partial y} & 0 & \frac{\partial N3}{\partial y} & 0 & \frac{\partial N4}{\partial y} \\ \frac{\partial N1}{\partial y} & \frac{\partial N1}{\partial x} & \frac{\partial N2}{\partial y} & \frac{\partial N2}{\partial x} & \frac{\partial N3}{\partial y} & \frac{\partial N3}{\partial x} & \frac{\partial N4}{\partial y} & \frac{\partial N4}{\partial x} \\ 0 & 0 & 0 & 0 & 0 & 0 & 0 & 0 \end{bmatrix} \tag{2.10}$$

with:

$$\mathbf{N} = \begin{bmatrix} N1 \\ N2 \\ N3 \\ N4 \end{bmatrix} = \begin{bmatrix} \frac{1}{4}(1-\xi)(1-\eta) \\ \frac{1}{4}(1-\xi)(1+\eta) \\ \frac{1}{4}(1+\xi)(1+\eta) \\ \frac{1}{4}(1+\xi)(1-\eta) \end{bmatrix} \tag{2.11}$$

where $\boldsymbol{N}$ is the shape function matrix, ξ and η are local coordinates.

Rewriting equation (2.9) as follows:

$$\int_V \{\delta\mathbf{u}\}^T[\mathbf{B}]^T[\mathbf{D}]\{\boldsymbol{\varepsilon}\}dV = \int_V \{\delta\mathbf{u}\}^T\rho\Big(\{\mathbf{b}\} - \{\mathbf{a}\}\Big)dV + \int_\Gamma \{\delta\mathbf{u}\}^T\{\boldsymbol{s^s}\}d\Gamma \tag{2.12}$$

Eliminating the term $\{\delta\mathbf{u}\}^T$ in both sides and rewriting the stress (i.e. $[d\boldsymbol{\sigma}] = [\mathbf{D}]\{d\boldsymbol{\varepsilon}\}$) in incremental form (i.e. $[\boldsymbol{\sigma}] = [\boldsymbol{\sigma}_0] + [\Delta\boldsymbol{\sigma}]$) yields:

$$\int_V [\mathbf{B}]^T[\Delta\boldsymbol{\sigma}]dV = \int_V \rho\{\mathbf{b}\}dV - \int_V \rho\{\mathbf{a}\}dV - \int_V [\mathbf{B}]^T[\Delta\boldsymbol{\sigma}_0]dV + \int_\Gamma \{\boldsymbol{s^s}\}d\Gamma \tag{2.13}$$

The incremental stress is written using the strain-stress and strain-displacement laws $[\Delta\boldsymbol{\sigma}] = [\mathbf{D}]\{\mathbf{B}\}\{\Delta\bar{\mathbf{u}}\}$ where $\{\Delta\bar{\mathbf{u}}\}$ is the vector of nodal displacements. This gives:

$$\int_V [\mathbf{B}]^T[\mathbf{D}]\{\mathbf{B}\}\{\Delta\bar{\mathbf{u}}\}dV = \int_V \rho\{\mathbf{b}\}dV - \int_V \rho\{\mathbf{a}\}dV - \int_V [\mathbf{B}]^T[\boldsymbol{\sigma}_0]dV + \int_\Gamma \{\boldsymbol{s^s}\}d\Gamma \tag{2.14}$$

At this stage, MPM is similar to FEM where the governing equations are solved at the background mesh. equation (2.14) can be rewritten in the global matrix form as:

$$[\mathbf{K}]\{\Delta\bar{\mathbf{u}}\} = \{\mathbf{F}\}_{ext} - \{\mathbf{F}\}_{int} - [\mathbf{m}]\{\bar{\mathbf{a}}\} \tag{2.15}$$

where $[\mathbf{K}]$ is the global stiffness matrix, $\{\mathbf{F}\}_{ext}$ and $\{\mathbf{F}\}_{int}$ are the external and internal vector, respectively, and $[\mathbf{m}]$ is the consistent mass matrix.

In which:

$$[\mathbf{K}] = \int_V [\mathbf{B}]^T[\mathbf{D}]\{\mathbf{B}\}dV \tag{2.16}$$

$$\{\mathbf{F}\}_{ext} = \int_V \rho\{\mathbf{b}\}dV + \int_\Gamma \{\boldsymbol{s^s}\}d\Gamma \tag{2.17}$$

$$\{\mathbf{F}\}_{int} = \int_V [\mathbf{B}]^T[\boldsymbol{\sigma}_0]dV \tag{2.18}$$

$$[\mathbf{m}] = \int_V \rho dV \tag{2.19}$$

The volume and surface integral of the matrices are then approximated with a quadrature rule. Therefore, these matrices can be computed as weighted sums of function values at integration points; in other words, material points, as follows:

$$[\mathbf{K}] = \sum_{p=1}^{nmps} [\mathbf{B}]^T[x_p][\mathbf{D}][\mathbf{B}][x_p]|J|W_p \tag{2.20}$$

$$\{\mathbf{F}\}_{ext} = \sum_{p=1}^{nmps} \rho_p[\mathbf{N}]^T[x_p]\{\mathbf{b}\}|J|W_p + \sum_{p=1}^{bmps} [\mathbf{N}]^T[x_p]\{\boldsymbol{s^s}\} \tag{2.21}$$

$$\{\mathbf{F}\}_{int} = \sum_{p=1}^{nmps} [\mathbf{B}]^T[x_p][\mathbf{D}][\boldsymbol{\sigma}_0]|J|W_p \tag{2.22}$$

$$[\mathbf{m}] = \sum_{p=1}^{nmps} \rho_p [\mathbf{N}]^T [x_p][\mathbf{N}][x_p]|J|W_p \tag{2.23}$$

While the stiffness matrix and the internal force vector are integrated over the body with the *nmps* as a total of material points, the external load vector is integrated with *bmps* as a number of boundary material points that have traction load acting on. The Jacobian $[J]$ and material point weight W_p are calculated for each integration points (i.e. material points). The element consistent mass matrix is computed in equation (2.23) with the elemental shape functions. However, this approach leads to a higher computational cost as the solution requires matrix inversion. The element lumped mass matrix claimed by Deshpande et al. (2016) therefore is used here instead, and it is computed by summing all diagonal and off diagonal terms each row as follows:

$$\mathbf{m}_{ii} = \sum_j \mathbf{m}_{ij} \tag{2.24}$$

Finally, the (element) discretised equation in matrix form can be writen:

$$\begin{aligned}\sum_{p=1}^{nmps} [\mathbf{B}]^T [x_p][\mathbf{D}][\mathbf{B}][x_p]\{\Delta\bar{\mathbf{u}}\}^{t+\Delta t}|J|W_p = \sum_{p=1}^{nmps} \rho_p [\mathbf{N}]^T [x_p][\mathbf{b}]^{t+\Delta t}|J|W_p - \sum_{p=1}^{nmps} [\mathbf{B}]^T [x_p][\mathbf{D}][\boldsymbol{\sigma}]^t|J|W_p \\ - \sum_{p=1}^{nmps} \rho_p [\mathbf{N}]^T [x_p][\mathbf{N}][x_p]\{\bar{\mathbf{a}}\}^{t+\Delta t}|J|W_p + \sum_{p=1}^{bmps} [\mathbf{N}]^T [x_p]\{\boldsymbol{s}^{\boldsymbol{s}}\}^{t+\Delta t}\end{aligned} \tag{2.25}$$

2.3. Newmark's time integration scheme

The Newmark's time integration scheme is used to approximate the solution at time $t + \Delta t$. The dynamic terms at the configuration $t + \Delta t$ will be evaluated with the obtained solution of the previous time step t velocity as:

$$\{\bar{\mathbf{v}}\}^{t+\Delta t} = \Big[\{\bar{\mathbf{v}}\}^t + [(1-\gamma]\{\bar{\mathbf{a}}\}^t + \gamma\{\bar{\mathbf{a}}\}^{t+\Delta t}\Big]\Delta t \tag{2.26}$$

$$\{\bar{\mathbf{u}}\}^{t+\Delta t} = \{\bar{\mathbf{u}}\}^t + \{\bar{\mathbf{v}}\}^t \Delta t + \Big[\big(\frac{1}{2} - \alpha\big)\{\bar{\mathbf{a}}\}^t + \alpha\{\bar{\mathbf{a}}\}^{t+\Delta t}\Big]\Delta t^2 \tag{2.27}$$

Choosing the constant-average-acceleration approach, the stepping parameters needed are: $\alpha = 0.25$ and $\gamma = 0.5$. Isolating the acceleration in equation (2.27):

$$\{\bar{\mathbf{a}}\}^{t+\Delta t} = \frac{4\{\Delta\bar{\mathbf{u}}\}^{t+\Delta t}}{\Delta t^2} - \frac{4\{\bar{\mathbf{v}}\}^t}{\Delta t} - \{\bar{\mathbf{a}}\}^t \tag{2.28}$$

Substituting equation (2.28) into equation (2.26) yields:

$$\{\bar{\mathbf{v}}\}^{t+\Delta t} = \frac{2\{\Delta\bar{\mathbf{u}}\}^{t+\Delta t}}{\Delta t} - \{\bar{\mathbf{v}}\}^t \tag{2.29}$$

Substituting equations (2.28) and (2.29) into equation (2.15) and then using the modified Newton-Raphson (constant stiffness) iteration scheme, results in the final equation:

$$\left([\mathbf{K}]^t + \frac{4[\mathbf{m}]^t}{\Delta t}\right)\{\Delta\bar{\mathbf{u}}\}_{k+1}^{t+\Delta t} = \{\mathbf{F}\}_{ext}|_k^{t+\Delta t} - [\mathbf{m}]^t\left(\frac{4\{\Delta\bar{\mathbf{u}}\}_k^{t+\Delta t}}{\Delta t^2} - \frac{4\{\bar{\mathbf{v}}\}^t}{\Delta t} - \{\bar{\mathbf{a}}\}^t\right) - \{\mathbf{F}\}_{int}|_k^{t+\Delta t} \tag{2.30}$$

or:

$$[\bar{\mathbf{K}}]\{\Delta\mathbf{u}\}_{k+1}^{t+\Delta t} = \Big(\{\mathbf{F}\}_{ext} - \{\mathbf{F}\}_{kin} - \{\mathbf{F}\}_{int}\Big)|_k^{t+\Delta t} \tag{2.31}$$

with:

$$[\bar{\mathbf{K}}] = [\mathbf{K}]^t + \frac{4[\mathbf{m}]^t}{\Delta t} = \sum_{p=1}^{nmps} [\mathbf{B}]^T [x_p][\mathbf{D}][\mathbf{B}][x_p]|J|W_p + \frac{4[\mathbf{m}]^t}{\Delta t} \tag{2.32}$$

$$\{\mathbf{F}\}_{kin}^{t+\Delta t} = [\mathbf{m}]^t \left(\frac{4\{\Delta\bar{\mathbf{u}}\}_k^{t+\Delta t}}{\Delta t^2} - \frac{4\{\bar{\mathbf{v}}\}^t}{\Delta t} - \{\bar{\mathbf{a}}\}^t \right) \tag{2.33}$$

$$\{\mathbf{F}\}_{ext}^{t+\Delta t} = \sum_{p=1}^{nmps} \rho_p [\mathbf{N}]^T [x_p] \{\mathbf{b}\}^t |J| W_p + \sum_{p=1}^{bmps} [\mathbf{N}]^T [x_p] \{\boldsymbol{s}^{\boldsymbol{s}}\}^{t+\Delta t} \tag{2.34}$$

$$\{\mathbf{F}\}_{int}^{t+\Delta t} = \sum_{p=1}^{nmps} [\mathbf{B}]^T [x_p] [\mathbf{D}] [\boldsymbol{\sigma}_p]^t |J| W_p \tag{2.35}$$

The stiffness matrix is determined for the previous configuration at time t while contributions of external force $\{\mathbf{F}_{ext}\}$, internal force $\{\mathbf{F}_{int}\}$ and kinematic force $\{\mathbf{F}_{kin}\}$ are updated at iteration k at the same time step $t + \Delta t$. The subscripts k and $k+1$ refer to the modified Newton-Raphson iteration scheme. The scheme evaluates $\{\mathbf{F}_{ext}\}$, $\{\mathbf{F}_{int}\}$ and $\{\mathbf{F}_{kin}\}$ to give the correction of the incremental nodal displacements. The tolerance value *tol* is chosen to stop the looping activity once desired the solution is obtained:

$$\frac{|\Delta u_k|}{|u_k|} < tol \tag{2.36}$$

This criteria is proven to be sufficient to prevent convergence due to iteration stagnation as claimed by Gonzalez Acosta et al. (2021).

2.4. Quasi-static formulation

By ignoring the inertia terms (or the kinematic force), a quasi-static equilibrium is reached:

$$[\mathbf{K}]\{\Delta\bar{\mathbf{u}}\} = \left(\{\mathbf{F}\}_{ext} - \{\mathbf{F}\}_{int} \right) \tag{2.37}$$

Since the quasi-static equilibrium eliminates all of kinematic energy, it can be used to analysed the long-term behaviour of the domain with some special treatments. In practice, the quasi-static analysis is performed to calculate and generate the initial stress of a simulated body.

2.5. Nodal mapping and interpolation

At the beginning of each time step, interpolation of nodal mass, velocity and acceleration is performed. Recall that information of material points at the configuration t are mapped to nodes using shape functions, before the assemble of global matrices and the solutions phase are performed. The acceleration of node i is determined as:

$$\bar{a}_i^t = \frac{\sum_{p=1}^{nmps} \rho_p a_p^t N_i(x_p) |J| W_p}{\sum_{p=1}^{nmps} a_p^t N_i(x_p) |J| W_p} \tag{2.38}$$

After assembling the global stiffness matrix by using equation (2.32), a quasi-loop is performed to estimate nodal displacements (equation (2.30)) in which the internal force vector, the external force and internal force are updated every iteration.

Then the material point's acceleration is updated with the use of shape function as:

$$a_p^{t+\Delta t} = \sum_{i=1}^{nn} N_i x_p \bar{a}_i^{t+\Delta t} \tag{2.39}$$

where nn is the number of nodes of the element in which the material point p is lying inside.

After equilibrium is reached, the material point's stresses are computed as:

$$[\boldsymbol{\sigma}_p]^{t+\Delta t} = [\mathbf{D}][\mathbf{B}][x_p]\{\bar{\mathbf{u}}\}^{t+\Delta t} + [\boldsymbol{\sigma}_p]^t \tag{2.40}$$

Finally, velocity and locations of material points are determined with nodal displacements:

$$v_p^{t+\Delta t} = \mathbf{v}_p^t + \frac{\Delta t}{2} \left(\sum_{i=1}^{nn} N_i x_p \bar{a}_i^{t+\Delta t} + a_p^t \right) \tag{2.41}$$

$$x_p^{t+\Delta t} = \sum_{i=1}^{nn} \mathbf{N}_i x_p \bar{u}_i^{t+\Delta t} + \mathbf{x}_p^t \tag{2.42}$$

Note that the material point's stresses are updated every iteration whereas material points acceleration, velocity and position are updated after equilibrium is reached.

2.6. Generalised Interpolation Material Point Method

Stress oscillations are widely known as one of the main drawbacks of MPM which significantly affect the output quality. Some recent studies have attempted to address the main reasons for these stress inaccuracies as well as introduced some solutions to this. The origins of this problem have been analysed to be a combination of: (a) choice of basis function; (b) the quadrature error; and (c) cell crossing problem. Refer to Bardenhagen et al. (2000), Gonzalez Acosta et al. (2021), Steffen, Kirby, et al. (2008), and Tielen et al. (2017) for more detailed explanations. Major improvements which have contributed to this problem and have been widely proven to be effective are the generalized material point method (i.e. GIMP) proposed by Bardenhagen et al. (2000) and the use of quadratic B-spline basis function introduced by Steffen, Kirby, et al. (2008). Many studies have analysed the advantages of these two methods in reducing stress oscillations. These methods have been discussed to be similar to each other. It is because both methods construct basis functions by convolving piecewise-constant shape functions with themselves. Direct to Steffen, Wallstedt, et al. (2008) for further reading. Only the GIMP shape functions and shape function gradients are integrated to this work, and will be discussed in detail.

With the GIMP method, each material point has its own physical domain, and the activated elements are now determined by the material's physical domain instead of using material points location.

Figure 2.2 shows the way of activating elements with GIMP and conventional MPM. Figure 2.2a shows a simulated domain Ω is discretised into four 4-node quadratic elements of size Δx and a material point (red dot) with its support domain Ω_p. In figure 2.2b, the material point which lays inside completely inside the lower left element will result in the activation of only element $E1$. While with GIMP (figure 2.2a), four elements E_1, E_2, E_3, E_4 are all activated as the material point's support domain overlaps all four element's regions.

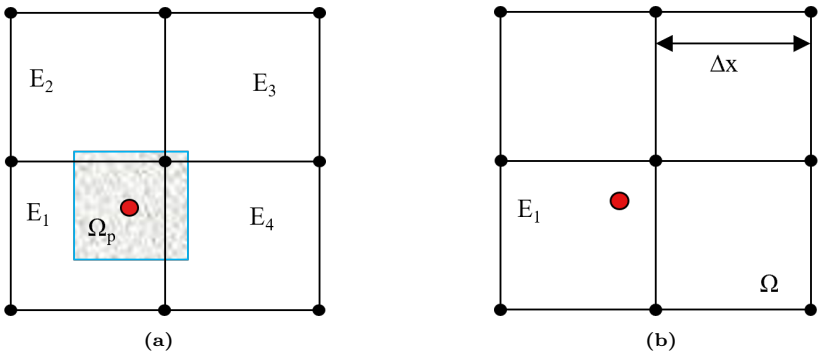

Figure 2.2: GIMP element activation and normal MPM element activation, a) GIMP and b) MPM

The GIMP shape function (S_{ip}) and its gradient (∇S_{ip}) are determined in one dimensional form as:

$$\mathbf{S}_{ip}(x) = \frac{1}{V_p} \int_{\Omega_p \cap \Omega} \chi_p(x) \mathbf{N}_i(x) dx \tag{2.43}$$

$$\nabla \mathbf{S}_{ip}(x) = \frac{1}{V_p} \int_{\Omega_p \cap \Omega} \chi_p(x) \nabla \mathbf{N}_i(x) dx \tag{2.44}$$

where V_p is the particle volume. GIMP shape functions are integrated over the joining domain of a material point support domain Ω_p and the problem domain Ω. $\mathbf{N}_i$ and $\nabla \mathbf{N}_i$ are standard FE shape

function and derivatives of shape function, respectively. While the activation function χ_p delimiting the support domain of the material point is given as:

$$\chi_p(x) = \begin{cases} 1, & \text{if x} \cap \Omega_p \\ 0, & \text{otherwise} \end{cases} \tag{2.45}$$

The 2D and 3D form of the GIMP shape function are determined by taking products of 1D GIMP shape function in each direction as:

$$\mathbf{S}_{ip}^{2D} = \mathbf{S}_{ip}(x).\mathbf{S}_{ip}(y) \tag{2.46}$$

$$\mathbf{S}_{ip}^{3D} = \mathbf{S}_{i}p(x).\mathbf{S}_{ip}(y).\mathbf{S}_{ip}(z) \tag{2.47}$$

where $\mathbf{S}_{ip}(j)$ is the 1D GIMP shape function corresponding to the j-direction. This thesis uses the 2D weighting functions (or shape functions) obtained from equation (2.46) as:

$$\mathbf{S}_{ip}^{2D}(x) = \begin{cases} 0 & \Delta x + l_p < |x_{ip}| \\ \frac{(\Delta x + l_p - x_{ip})^2}{4\Delta x l_p} & \Delta x - l_p < x_{ip} \leq \Delta x + l_p \\ 1 - \frac{x_{ip}}{\Delta x} & l_p < x_{ip} \leq \Delta x - l_p \\ 1 - \frac{x_{ip}^2 + l_p^2}{2\Delta x l_p} & -l_p < x_{ip} \leq l_p \\ 1 - \frac{x_{ip}}{\Delta x} & -\Delta x + l_p < x_{ip} \leq -l_p \\ \frac{(\Delta x + l_p + x_{ip})^2}{4\Delta x l_p} & -\Delta x - l_p < x_{ip} \leq \Delta x + l_p \end{cases} \tag{2.48}$$

where $x_{ip} = x_p - x_i$ where x_p is the x-coordinate of the material point p and x_i is the x-coordinate of node i, Δx is the element size in the x-direction and l_p is a half of the material support domain, in which $l_p(x) = l_p(y)$ corresponding to the square support domain of each material point. The GIMP shape function gradient are computed as:

$$\nabla\mathbf{S}_{ip}^{2D}(x) = \begin{cases} 0 & \Delta x + l_p < |x_{ip}| \\ -\frac{\Delta x + l_p + x_{ip}}{2\Delta x l_p} & \Delta x - l_p < x_{ip} \leq \Delta x + l_p \\ -\frac{1}{\Delta x} & l_p < x_{ip} \leq \Delta x - l_p \\ -\frac{x_{ip}}{\Delta x l_p} & -l_p < x_{ip} \leq l_p \\ \frac{1}{\Delta x} & -\Delta x + l_p < x_{ip} \leq -l_p \\ \frac{\Delta x + l_p + x_{ip}}{2\Delta x l_p} & -\Delta x - l_p < x_{ip} \leq \Delta x + l_p \end{cases} \tag{2.49}$$

The weighting function and its gradient in the y-direction can be computed following the exact procedure shown in equations (2.48) and (2.49) as a function of $y_{ip} = y_p - y_i$.

2.7. Double Mapping

The generalized material point method has been proven to be effective in reducing the stress oscillation derived from cell-crossing issue in MPM. However, it is proven that errors generated from the integration of the stiffness matrix are not vanished. Gonzalez Acosta et al. (2020) proved that it is because the GIMP gradients drop to zero at the inter-element boundaries. The author has proposed a double-mapping (DM) procedure to enhance the accuracy of nodal stiffness integration. The idea is to have the material elastic matrix additionally mapped to the Gauss point locations. In other words, FEM mapping will be performed to compute the elastic matrix, prior to the integration of stiffness matrix. This approach will be integrated later in order to improve the accuracy of the output solution.

First, linear shape function or FE shape function is used to compute the elastic matrix at nodes by interpolation from material points as:

$$[\mathbf{D}_i] = \sum_{p=1}^{nmp} N_i(x_p)[\mathbf{D}_p]W^* \tag{2.50}$$

where $[\mathbf{D}_i]$ is the elastic matrix at node i, $[\mathbf{D}_p]$ is the elastic matrix of material point p, nmp here is the current number of material points inside the element, $N_i(x_p)$ is the value of the shape function at node i computed with material point p and W^* is the modified weight of material points that is computed as:

$$W^* = W_p \frac{omp}{nmp} \tag{2.51}$$

where W_p is the material integration weight which is dimensionless and equal to the material point's volume corresponding to local coordinates, omp is the number of original material points inside the element and nmp is the number of current material points inside the element.

After interpolation from material points to the background nodes, the information is again distributed to the Gauss point's locations as follows:

$$[\mathbf{D}_g] = \sum_{i=1}^{nn} N_i(x_g)[\mathbf{D}_i] \tag{2.52}$$

where $[\mathbf{D}_g]$ is the elastic matrix at the Gauss's locations, $N_i(x_g)$ is the shape function value at node i computed with the Gauss's coordinates x_g and nn is the number of nodes of the element.

Finally, the elastic matrix $[\mathbf{D}_g]$ can be computed by combining equations (2.50) and (2.51). Then performing integration of stiffness matrix yields:

$$[\mathbf{K}]^t = \sum_{g=1}^{ngauss} [\mathbf{B}]^T[x_g]\left(\sum_{i=1}^{nn} N_i(x_g) \sum_{p=1}^{nmp} N_i(x_p)[\mathbf{D}_p]W^*\right)[\mathbf{B}][x_g]|J|W^{Gauss} \tag{2.53}$$

Here, $ngauss$ represents the number of Gauss integration points original in the element and W^{gauss} is the weight of each Gauss point (similar to FEM).

2.8. Composite Material Point Method (CMPM)

To increase the accuracy of stress recovery, Gonzalez Acosta et al. (2017) proposed the composite material point method (CMPM) which is modified from the composite finite element method (CFEM) introduced by Sadeghirad and Vaziri Astaneh (2011). The method extends the support domain used to recover the stresses therefore improving the accuracy of the stresses computed. CMPM shape functions which envelop all neighbouring elements of the element containing the material point are computed using Lagrange interpolation. Figure 2.3 shows the C^2 shape functions in 1D, in which each shape function N^2 now envelopes all the local element plus the neighbouring elements.

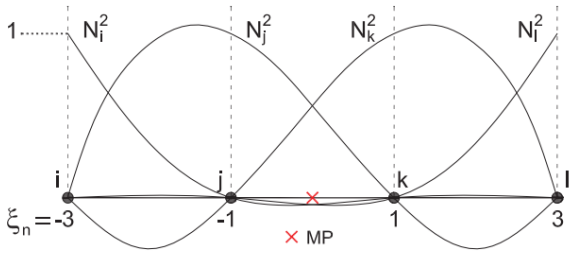

Figure 2.3: CMPM shape function with C^2 continuity for a central element, adopted from Gonzalez Acosta et al. (2017)

The N^2 shape function is computed using the Lagrange interpolation as:

$$N_n^2(\xi) = \prod_{m=1, m\neq j}^{n} \frac{\xi - \xi_m}{\xi_j - \xi_m} \tag{2.54}$$

where ξ is the nodal local coordinate in the extended domain, n is the number of nodes, ξ_j is the local coordinate of the N_n^2 shape function, and ξ_m is the local coordinate of the remaining nodes inside the

element. The CMPM shape functions for an element with two neighboring elements considering the material point (MP) is at the central element, can be computed by solving equation (2.54) at each node shown in figure 2.3 as:

$$\begin{bmatrix} N_i^2 \\ N_j^2 \\ N_k^2 \\ N_l^2 \end{bmatrix} = \frac{1}{16} \begin{bmatrix} -\dfrac{\xi^3 - 3\xi^2 - \xi + 3}{3} \\ \xi^3 - \xi^2 - 9\xi + 9 \\ -\xi^3 - \xi^2 + 9\xi + 9 \\ \dfrac{\xi^3 + 3\xi^2 - \xi - 3}{3} \end{bmatrix} \tag{2.55}$$

In case the MP is located at the boundary, the 1D CMPM shape functions are now computed as:

$$\begin{bmatrix} N_i^2 \\ N_j^2 \\ N_k^2 \end{bmatrix} = \frac{1}{4} \begin{bmatrix} -\dfrac{\xi^2 - 4\xi + 3}{2} \\ -\xi^2 + 2\xi + 3 \\ \dfrac{\xi^2 + 4\xi - 3}{2} \end{bmatrix} \tag{2.56}$$

Note that even though the CMPM shape function extends the domain, the local coordinates is still kept in range: $-1 \leq \xi \leq 1$. Similar to GIMP shape functions, the 2D CMPM shape functions are the product of the 1D CMPM shape function in each direction.

2.9. DM-GC technique

As discussed in section 2.7, GIMP method cannot diminish the inaccuracies derived from integration of stiffness matrix. To deal with this issue, Gonzalez Acosta et al. (2020) proposed a procedure to combine DM-GIMP and CMPM. This technique will be used as an advanced framework of MPM. The internal and external forces are computed with GIMP shape functions and shape function gradients, while the stiffness matrix is computed by the DM-GIMP technique, and finally the incremental stress is updated using CMPM shape function.

DM-GIMP technique employs local GIMP shape functions instead of the contiguous GIMP for interpolation to Gauss' points. Therefore, the local GIMP shape functions S_{ip}^* are constructed in a similar way as shown in equation (2.48), but the contributions of nearby element's GIMP shape functions is neglected. In other words, influence of the material point's support domain is limited inside the considering element. Refer to Charlton et al. (2017) for more detailed explanation of local GIMP shape functions and shape function gradients.

DM technique is now integrated with the use of iGIMP shape functions (or local GIMP shape function) S_{ip}^* in a similar way to what has been shown in section 2.7. The stiffness matrix $[\mathbf{K}]^t$ is determined as follows:

$$[\mathbf{K}]^t = \sum_{g=1}^{ngauss} [\mathbf{B}_{ip}]^T [x_g] \left(\sum_{i=1}^{nn} N_i(x_g) \sum_{p=1}^{smp} S_{ip}^*(x_p) [\mathbf{D}_p] W_p \right) [\mathbf{B}_{ip}] [x_g] |J| W^{Gauss} \tag{2.57}$$

where *smp* is the number of material points that have their support domains inside the element, S_{ip}^* is the iGIMP shape functions value of node i evaluated at the material point p. With the use of iGIMP method, the material point volume (i.e. weight) W_p is replaced by the modified weight W^*.

Finally, the incremental material point stresses are updated inside the quasi loop using CMPM method as:

$$[\Delta \boldsymbol{\sigma}_p] = [\boldsymbol{D}_p] [\nabla N^2] [x_p] \{\Delta \bar{\boldsymbol{u}}\}^{ext} \tag{2.58}$$

where $[\nabla N^2]$ is the matrix containing derivatives of CMPM shape functions and $\{\Delta \bar{\boldsymbol{u}}\}^{ext}$ is the nodal displacements vector in the extended domain. Besides, the extended domain in CMPM is not necessarily equal to GIMP support domain stencil. Moreover, all the state variables are still interpolated with GIMP shape functions.

3

Wave-absorbing boundaries

In the field of computation with dynamic analyses, one major issue is to accurately model the far - field medium or the semi - finite domains. To be able to work out the approximate solutions, numerical methods commonly resort to the finite domain or discrete domain. With this approach, the continuity in the real domain is replaced by a finite - dimensional domain truncated with fixed boundaries. This leads to feasible computations, but at the same time generates spurious reflections as the seismic wave cannot transmit through this boundary and hence bounces back. In reality, seismic waves should travel to the infinite region without getting any hindrances at these fixed boundary locations. First, a literature review section elaborates on the most common boundary conditions used in FEM to overcome the problem with numerical reflections at the boundaries. Then, the derivation and implementation of the viscous and the viscoelastic boundary using the MPM framework is discussed in detail. Finally, a procedure to improve the computational accuracy with the use of these boundaries will be introduced.

3.1. Literature review

A standard approach used to reduce wave reflection effects is using common elementary boundary conditions which are the Neumann condition (zero stress) and the Dirichlet condition (zero displacement), but placing them far away from the interested domain. This results in uneconomical and time - consuming computations since it requires large meshes. Besides, this technique is not able to represent the radiation condition at theses boundaries physically.

The most widely used solution to this problem is known as the *absorbing boundary condition* (also known as non - reflecting boundary, standard viscous boundary), derived by Lysmer and Kuhlemeyer (1969). This boundary is equivalent to a series of dashpots attached tangentially and normally to the interested surface. The condition has been proven to be effective in terms of absorbing waves of non-harmonic and harmonic frequency, while its simplicity lead to straightforward implementations into finite element framework. Later, Deeks and Randolph (1994) proposed a *viscoelastic boundary* which shares similarities with the viscous boundary. The boundary schematizes a Kelvin-Voigt element attached normally and tangentially to the surface. It is well known that this boundary can simulate the elastic recovery of the unbounded domain to a certain amount.

Smith (1974) introduced the *superposition boundary.* This condition uses the superposition principle, applying two "boundary problems": zero normal displacement and shear stress; zero tangential displacement and normal stress. Each of these conditions will generate one separate reflection of waves, with the same amplitude but opposite direction. Therefore, waves entering this zone still deduct spurious reflections, but will be cancelled out by each other. The author suggested that this solution can deal with surface waves, but often fails to prevent high order terms of reflections.

Clayton and Engquist (1977) proposed the *paraxial boundary* for scalar waves and elastic waves. The *paraxial family* is defined based on the key idea to make the boundary "transparent" to outward - going waves. However, this method is not suitable for direct implementation in finite element programs (Kontoe (2006)). Cohen (1980) modified the condition for direct implementation in FE programs. The theoretical derivation is shown to be superior over the *standard viscous boundary*, but the numerical

performances illustrate only slight improvement as proven by Cohen (1980).

Liao and Wong (1984) introduced a new condition called the *extrapolation boundary* which has close connection to the paraxial family conditions. The radiation condition is represented by extrapolating present and past data along a line normal to the boundary surface. However, this approach requires large storage for computation and its results are quite low - quality in case there are many impinging waves at the boundary, as pointed out by Kontoe (2006).

Underwood (1981) derived the *doubly - asymptotic boundary (DA)* which numerically adds the viscous forces at the boundary in case of high frequency and the spring stiffness in case of low frequency problem. The nature of this condition is that with low frequencies, the velocity component is small relative to the displacement component so that the boundary force is characterized by a springs system while a damping system is replaced in case of high frequencies where the velocity is dominant. As a result, this boundary is less accurate in the simulation of medium range frequencies.

Another boundary introduced by Buneman (1959) is the *multi - directional boundary* calculated based on the angle of incidence of waves. Kellezi (2000) and Kontoe (2006) show that the boundary is sophisticated while the accuracy is not high.

The *perfectly matched layer (PML)* is originally derived for the use of electromagnetic waves, but later became widely used to absorb the reflected waves. The idea is to replace parts of the region adjacent to the interested boundary with additionally numerical layers which have the ability to attenuate all the spurious reflections. Later, Basu and Chopra (2004) formulated a PML in the time domain using inverse Fourier transformation. The authors also claimed that this method can achieve higher accuracy than the *standard viscous* method with a higher computation cost of 50% - 70%. A similar form of this condition was derived by Semblat (2011) called the *Caughey absorbing layer method*. The idea is similar to PML, but this method allows multi - directional wave attenuation.

While some of the proposed boundary conditions are straightforward and easy to implement, others have been claimed to be complicated to apply numerically while the results are not desirable. Summarizing, the *standard viscous boundary* and *viscoelastic boundary* are chosen to be developed in the MPM framework as they are simple and their absorption of reflections are widely proved to be effective.

3.1.1. Standard Viscous boundary

Figure 3.1 shows a visulization of the viscous boundary. As can be seen, the boundary simulates a series of dashpots attached tangentially and normally to the interested surface.

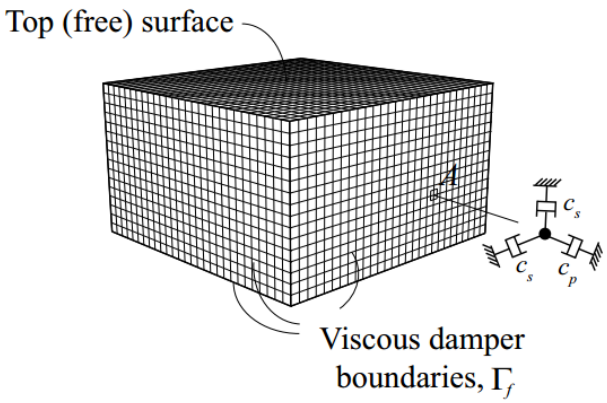

Figure 3.1: Illustration of viscous boundary in 3D simulation, after Løkke and Chopra (2019)

To derive the expression for the viscous boundary based on the one-dimensional wave theory, a soil column with P-wave load that propagates in the y^- direction is investigated, as shown in figure 3.2:

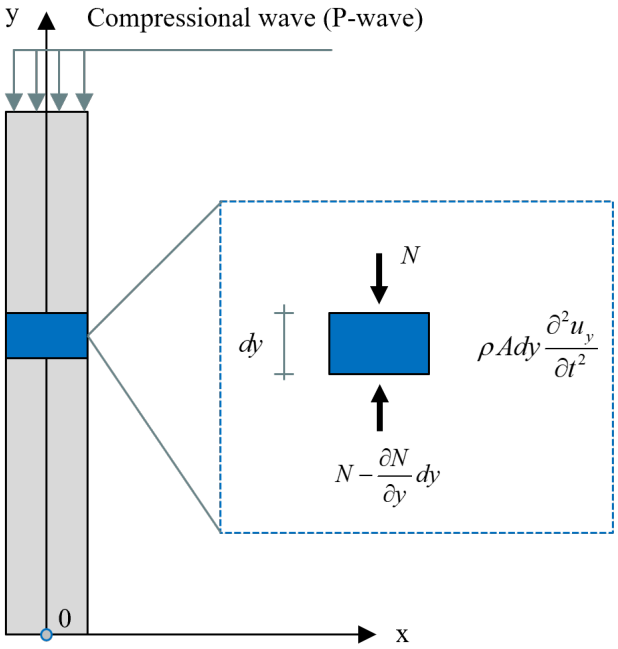

Figure 3.2: Illustration of a soil column model

The compressional wave induced by normal force N acting on an infinitesimal element, in which the equilibrium equation can be expressed as:

$$N - \left(N - \frac{\partial N}{\partial y}dy\right) = \rho A dy \frac{\partial^2 u_y}{\partial t^2} \tag{3.1}$$

$$\frac{\partial N}{\partial y}dy - \rho A dy \frac{\partial^2 u_y}{\partial t^2} = 0 \tag{3.2}$$

where dy is the thickness of the element and u_y is the vertical displacement. With plane strain analysis, the normal force can be computed with the force-displacement relation as:

$$N = \sigma A = \frac{E(1-\nu)}{(1+\nu)(1-2\nu)} A \frac{\partial u_y}{\partial y} \tag{3.3}$$

$$N = \rho \frac{E(1-\nu)}{\rho(1+\nu)(1-2\nu)} A \frac{\partial u_y}{\partial y} = \rho C_p^2 A \frac{\partial u_y}{\partial y} \tag{3.4}$$

where E is Young's modulus, ν is Poisson's ratio, $C_p = \sqrt{\dfrac{E(1-\nu)}{\rho(1+\nu)(1-2\nu)}}$ is the compressional velocity of the soil body and A represents element area. Substituting equation (3.4) into equation (3.2) yields:

$$\frac{\partial^2 u_y}{\partial y^2} - \frac{1}{C_p^2}\frac{\partial^2 u_y}{\partial t^2} = 0 \tag{3.5}$$

The general solution for this equation is the function of location and time as:

$$u_y(y,t) = f(y + C_p t) + g(y - C_p t) \tag{3.6}$$

As can be seen in figure 3.3, when the incoming load or signal (i.e. $F_{load}(y,t)$) propagates to the boundary, it induces a reflection (i.e. $f(y+C_p t)$) and a transmitting part (i.e. $g(y-C_p t)$). Considering the boundary can absorb all reflections, only the transmitting part of the solution is kept as:

$$u_y(y,t) = g(y - C_p t) \tag{3.7}$$

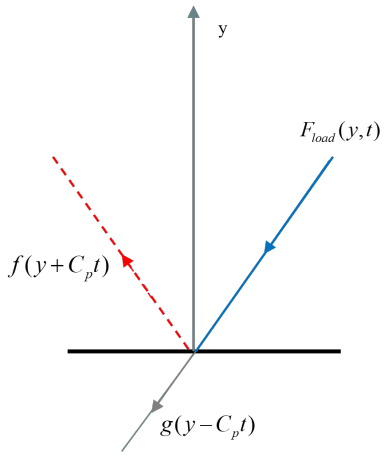

Figure 3.3: Solution for displacement at the boundary

This solution satisfies equation (3.5). The velocity, strain and stress at the boundary now can be computed as:

$$v(y,t) = \frac{\partial u_y}{\partial t} = -C_p g'(y - C_p t) \tag{3.8}$$

$$d\varepsilon = \frac{\partial u_y}{\partial y} = g'(y - C_p t) \tag{3.9}$$

$$d\sigma = \frac{E(1-\nu)}{(1+\nu)(1-2\nu)} d\varepsilon = \frac{E(1-\nu)}{(1+\nu)(1-2\nu)} g'(y - C_p t) \tag{3.10}$$

$$d\sigma = \rho C_p^2 g'(y - C_p t) = -\rho C_p v(y,t) \tag{3.11}$$

where $v(y,t)$ is the velocity of soil particle in the y-direction. Following the exact solution with a P-wave load, one can determine the incremental shear stress by deriving the equilibrium equation with shear force Q based on the shear velocity:

$$d\tau = \rho C_s^2 g'(x - C_s t) = -\rho C_s v(x,t) \tag{3.12}$$

with:

$$C_s = \sqrt{\frac{E}{2\rho(1+\nu)}} \tag{3.13}$$

where C_s is the S-wave velocity property of the soil body. Based on these solutions, Lysmer and Kuhlemeyer (1969) regulated the viscous condition as follows:

$$\sigma = -a\rho C_p v_n \tag{3.14}$$

$$\tau = -b\rho C_s v_s \tag{3.15}$$

where a, b are given coefficients, which are set to $a = b = 1$ for better accuracy, σ, τ are the normal stress and shear stress components respectively (different from stress tensor $\boldsymbol{\sigma}$) and v_n and v_s are the normal and shear velocities of a soil particle, which can also be expressed in terms of normal displacement u and tangential displacement v of soil particle at that location:

$$\begin{bmatrix} v_n \\ v_s \end{bmatrix} = \begin{bmatrix} \dfrac{\partial u}{\partial t} \\ \dfrac{\partial v}{\partial t} \end{bmatrix} \tag{3.16}$$

This boundary condition is independent of frequency, and therefore it absorbs both harmonic and non-harmonic waves. Nearly perfect absorption can be achieved when one is dealing with one - dimensional problems with the propagation of body waves (P - wave and S - wave). This formulation has been proven to be effective absorbing the incoming waves, while it is also straightforward to implement.

3.1.2. Viscoelastic boundary

Figure 3.4 visualizes the viscoelastic boundary with dashpot elements functioning as the absorption component while the spring elements represent the stiffness of the far field domain.

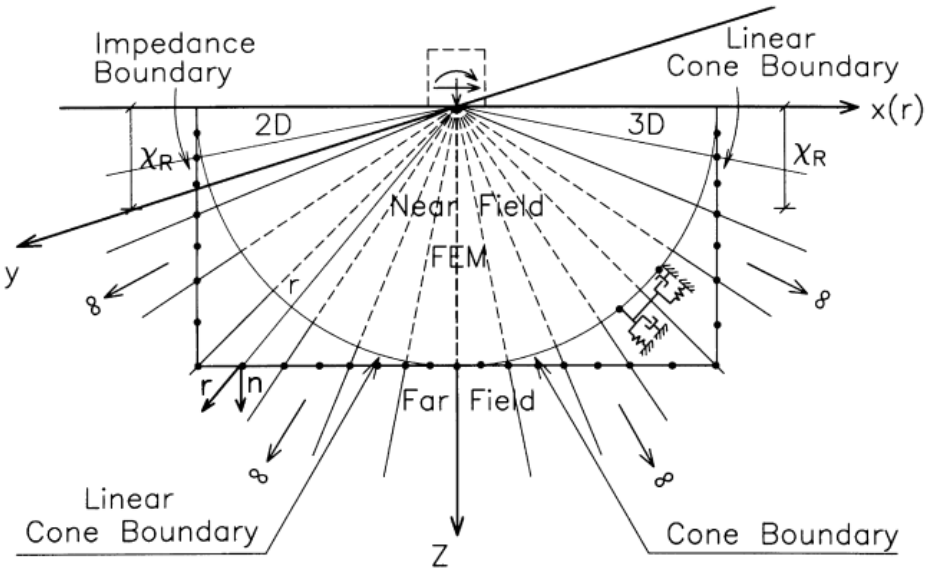

Figure 3.4: Local transmitting boundary after Kellezi (2000)

The viscoelastic (or cone boundary) can be derived following a similar procedure to the viscous boundary. Kellezi (2000) derived the formulation in plane strain analysis based on the context of 1D wave theory, in which body waves should propagate radially outward from the excitation location. The displacement solution at the boundary with propagation of a P-wave signal, discussed in Kontoe (2006), can be expressed as:

$$u_y(y,t) = \frac{f(y+C_pt)}{y} + \frac{g(y-C_pt)}{y} \tag{3.17}$$

Eliminating the reflection term, the particle velocity, strain and y-direction stress at the boundary can be computed as:

$$v(y,t) = \frac{\partial u_y}{\partial t} = -\frac{C_p g'(y-C_pt)}{y} \tag{3.18}$$

$$d\varepsilon = \frac{\partial u_y}{\partial y} = \frac{g'(y-C_pt)}{y} - \frac{g(y-C_pt)}{y^2} \tag{3.19}$$

$$d\sigma = \rho C_p^2 \left[\frac{g'(y-C_pt)}{y} - \frac{g(y-C_pt)}{y^2} \right] \tag{3.20}$$

Substituting equation (3.18) into equation (3.20) yields:

$$d\sigma = -\rho C_p v(y,t) - \frac{\rho C_p^2}{y} u_y(y,t) \tag{3.21}$$

Let r_b be the distance from the excitation location to the boundary location, equation (3.21) is rewritten as:

$$d\sigma = -\rho C_p v(y,t) - \frac{\rho C_p^2}{r_b} u_y(y,t) \tag{3.22}$$

Again, the shear stress condition can also be derived, by evaluating the equilibrium equation with shear force Q and shear-wave velocity C_s, resulting in:

$$d\tau = -\rho C_s v(y,t) - \frac{\rho C_s^2}{r_b} u_y(y,t) \tag{3.23}$$

The viscoelastic boundary condition therefore can be written as:

$$\sigma = -\rho C_p v_n - K_n u \tag{3.24}$$

$$\tau = -\rho C_s v_n - K_s u \tag{3.25}$$

where $K_n = \rho C_p^2 / r_b$ and $K_s = \rho C_s / r_b$ are the spring stiffnesses of the far field medium in normal and tangential direction, according to Kellezi (2000), where r_b is the distance from the boundary to the source of excitation. Deeks and Randolph (1994) introduced another solution to calculate the stiffness part as:

$$K_n = \frac{G}{2r_b};\ \ K_s = \frac{G}{2r_b} \tag{3.26}$$

where G is the shear modulus.

In this thesis, the Deek's formulations will be used, since it renders better results than the Kellezi's formulations.

One can recognize the viscous part as the same as the standard viscous boundary, which simulates a series of dashpots, while the remaining part stands for a series of springs oriented normal and tangential to the boundary. The name "viscoelastic" derived from the idea that the elastic recovery from the infinite region is also added to the condition. Later, Kellezi (2000) also introduced the cone boundary which shares similar idea.

With the contribution of the spring terms, the model can eliminate the spurious "movement" of the region near the bounded boundary due to low frequency influence since it is now constrained by the numerical recovery. However, determination of the spring stiffnesses K_n, K_s is based on the distance from the excitations to the boundary (r_b) Therefore, it limits the use of this boundary to problems with known source of excitations. Similar to the standard viscous boundary, this solution is frequency - independent. Moreover, the boundary can also be modified to cope with Rayleigh waves (Kellezi (2000)). Kontoe (2006) shows that the overall accuracy of the viscoelastic boundary is similar to the standard viscous boundary applied to high frequency problems, for low frequency problems however, the use of the viscoelastic boundary is preferredx.

3.2. Imposing DBC to MPM at boundary nodes

In FEM, the equations of motion are solved at the background grid and the boundary condition can be imposed directly at the surface nodes. This will be used as a starting point of the implementation. First, the MPM extended equation with dynamic boundary will be discussed following the conventional way to imply boundary conditions in FEM in detail. Based on this, the viscous and viscoelastic boundary can be implemented into basic MPM following FEM's approach. Then, the approach will be discussed to impose these boundary conditions to the advanced framework of MPM, i.e., the DM-GC formulation.

3.2.1. Dynamic boundary conditions with basic MPM

In MPM, the equilibrium equation is solved at the background grid mesh, with global matrices integrated from material point's locations to corresponding nodes. This means a straightforward approach to apply boundary conditions is imposing the boundary formulation directly at the background's boundary nodes.

Viscous boundary

The viscous boundary can be implement into the MPM framework imposing the viscous traction converted from the stress determined with the boundary conditions. Based on equations (3.14) and (3.15), viscous traction at the boundary can be determined as:

$$\{\mathbf{f}_{\mathbf{n,s}}^{\mathbf{vis}}\} = -\rho A_{bound} \begin{Bmatrix} a \\ b \end{Bmatrix} \begin{bmatrix} C_p & 0 \\ 0 & C_s \end{bmatrix} \begin{Bmatrix} v_n \\ v_s \end{Bmatrix} \tag{3.27}$$

or:

$$\{\mathbf{f}_{\mathbf{n,s}}^{\mathbf{vis}}\} = -a\rho A_{bound}[\mathbf{C}]\{\mathbf{v}_{\mathbf{n,s}}\} \tag{3.28}$$

where A_{bound} is the surface area.

The normal force (subscript n) and tangential force (subscript s) are determined based on multiplication

of normal stress and tangential (shear) stress with corresponding boundary surface areas. Then, the traction can be added into the governing equation similar to the external force, as an additional source of load traction $\{\mathbf{s}^s\}$.

Calculation of MPM is performed using a Cartesian coordinate system. Hence, it is important to transform the normal and tangential direction into the global coordinate system.

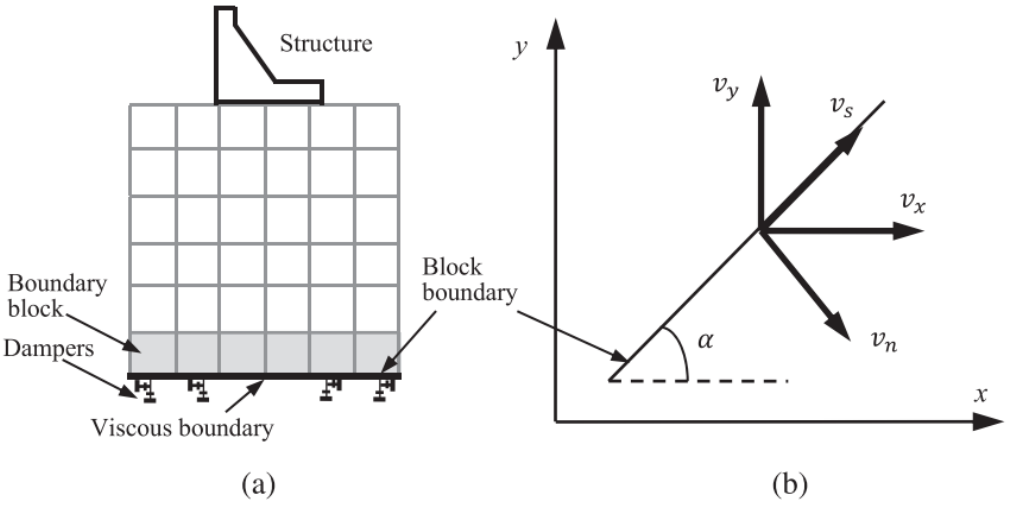

Figure 3.5: Schematic of the transformation matrix, after Fu et al. (2015)

The directional angle α between the axis x and the direction of the viscous boundary will be used to perform the transformation as follows:

$$[\mathbf{T}] = \begin{bmatrix} sin\alpha & -cos\alpha \\ cos\alpha & sin\alpha \end{bmatrix} \tag{3.29}$$

Since the equilibrium equation (2.30) is solved at the background mesh. Integration of the viscous stiffness and the viscous force can be done directly at the boundary (i.e. surface) nodes in a similar way as shown in the previous section.

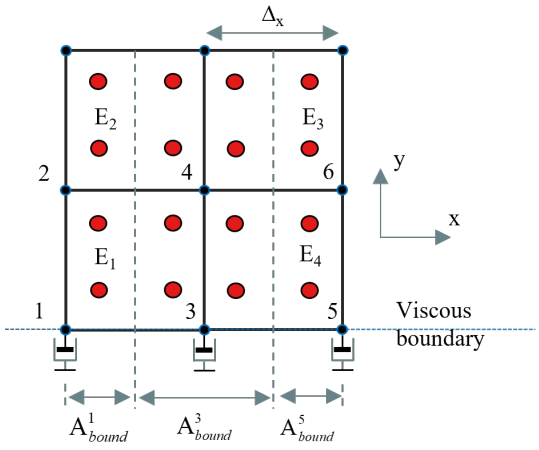

Figure 3.6: Schematize the viscous boundary illustration

The boundary area A_{bound} needs to be determined for each corresponding node. As can be seen in figure 3.6, the viscous force expressed by the dashpots are applying only at the surface nodes (node 1, 3 and 5 of element E_1, E_2). Each element (E_1, E_2) has 2 surface nodes covering equal boundary

areas which are a half of the cell size (i.e. $\Delta x/2$). This results in the boundary area of the inner node (node 3) as two times larger than the ones of the outer nodes (side nodes 1 and 5); in other words, $A^1_{bound} = A^5_{bound} = A^3_{bound}/2 = \Delta x/2$ where A^i_{bound} is the boundary area of node i.

Adding the viscous traction to 2.15 yields:

$$[\mathbf{K}]\{\Delta\mathbf{u}\} = \{\mathbf{F}\}_{ext} - \{\mathbf{F}\}_{int} - [\mathbf{m}]\{\mathbf{a}\} + \{\mathbf{f}\}^{vis} \tag{3.30}$$

with:

$$\{\mathbf{f}\}_{vis} = -a\rho A_{bound}[\mathbf{T}]^T[\mathbf{C}][\mathbf{T}]\{\mathbf{v}_{\mathbf{x},\mathbf{y}}\} \tag{3.31}$$

The Newmark's time integration is applied, the velocity determined by equation (2.29) yields the viscous force as:

$$\{\mathbf{f}\}_{vis} = -a\rho \sum_{i=1}^{nbn} A_{bound}[\mathbf{T}]^T[\mathbf{C}][\mathbf{T}]\Big(\frac{2\{\Delta\bar{\mathbf{u}}\}^{t+\Delta t}}{\Delta t} - \{\bar{\mathbf{v}}\}^t\Big) \tag{3.32}$$

where $\{\Delta\bar{\mathbf{u}}\}^{t+\Delta t}$, $\{\bar{\mathbf{v}}\}^t$ are the displacement and velocity vector of node i of the background mesh, respectively, nbn is the number of boundary nodes determined after the update phase is performed. The surface nodes are defined in MPM by locating surface edge nodes of all activated boundary elements (similar to FEM). Therefore, in case a material point jumps from one element to another, the surface nodes will be changed as well. As can be seen in figure 3.7a there are four elements activated: E_3, E_4, E_5, E_6 and the surface nodes are node 2, 4 and 6, while in case that material points displaced (figure 3.7b), the surface nodes now are node 1, 3 and 5. In practice, one can pre-define the outer layer of material points, then based on theses point's locations, surface nodes can be determined. For examples in figure 3.7b, the nodes 1, 3 and 5 can be located by finding all nodes that have the y-coordinate value lower than this value of material points at the last row of material points.

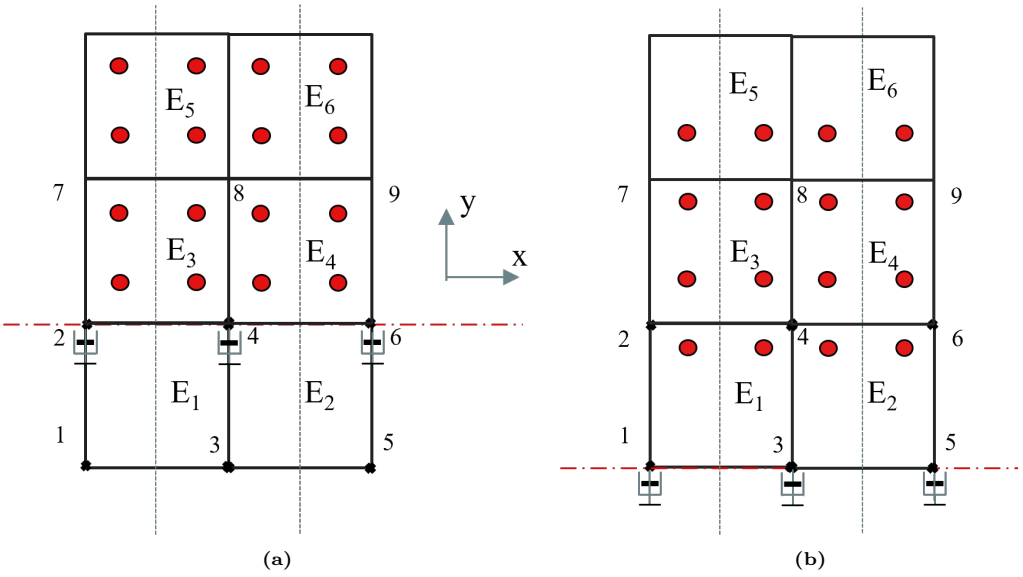

Figure 3.7: Description of determining boundary nodes, a) Before deformation and b) After material points displace

Finally, applying the modified Newton-Raphson iteration scheme for equation (3.30), yields:

$$\begin{aligned}([\mathbf{K}] + \frac{4[\mathbf{m}]}{\Delta t} + [\mathbf{k}]_{vis})^t\{\Delta\bar{\mathbf{u}}\}^{t+\Delta t}_{k+1} = \{\mathbf{F}\}_{ext}|^{t+\Delta t}_k - \{\mathbf{F}\}_{int}|^{t+\Delta t}_k + \{\mathbf{f}\}_{vis}|^{t+\Delta t}_k \\ -[\mathbf{m}]\Big(\frac{4\{\Delta\bar{\mathbf{u}}\}^{t+\Delta t}_k}{\Delta t^2} - \frac{4\{\bar{\mathbf{v}}\}^t}{\Delta t} - \{\bar{\mathbf{a}}\}^t\Big)\end{aligned} \tag{3.33}$$

where all the terms $[\mathbf{K}], \{\mathbf{F}\}_{ext}, \{\mathbf{F}\}_{int}, [\mathbf{m}]$ can be computed with equations (2.16), (2.23), (2.34) and (2.35). The viscous stiffness is computed at time t, the viscous force is updated in the current

configuration $t + \Delta t$. As explained above, the the viscous stiffness and viscous force will be determined as:

$$[\mathbf{k}]_{vis} = \frac{2a}{\Delta t} \sum_{i=1}^{nbn} \rho_i l_i [\mathbf{T}]^T [\mathbf{C}][\mathbf{T}] \tag{3.34}$$

$$\{\mathbf{f}\}_{vis} = -a \sum_{i=1}^{nbn} \rho_i l_i [\mathbf{T}]^T [\mathbf{C}][\mathbf{T}] \Big(\frac{2\{\Delta \bar{\mathbf{u}}_i\}|_k^{t+\Delta t}}{\Delta t} - \{\bar{\mathbf{v}}_i\}^t \Big) \tag{3.35}$$

where l_i is the boundary area, which is equal to cellsize (Δx) except the side nodes (for examples, nodes 1, 5 in figure 3.6), where the force is integrated over half of cellsize. Since the material points displace throughout the simulation, the boundary nodes need to be redefined after the update phase.

Viscoelastic boundary implementation

Similar to the viscous boundary, the equivalent viscoelastic boundary force can be expressed in terms of normal and shear stress conditions as:

$$\{\mathbf{f}\}_{viscoe} = -\rho A_{bound} \left(\begin{Bmatrix} a \\ b \end{Bmatrix} \begin{bmatrix} C_p & 0 \\ 0 & C_s \end{bmatrix} \begin{Bmatrix} v_n \\ v_s \end{Bmatrix} + \begin{bmatrix} K_n & 0 \\ 0 & K_s \end{bmatrix} \begin{Bmatrix} u_n \\ u_s \end{Bmatrix} \right) \tag{3.36}$$

With the viscous part has been illustrated in part (3.2.1), equation (3.36) is rewritten as:

$$\{\mathbf{f}\}_{viscoe} = \{\mathbf{f}\}_{vis} + \{\mathbf{f}\}_{spring} \tag{3.37}$$

Adding the equivalent force to Equation (2.15) yields:

$$[\mathbf{K}]\{\Delta \mathbf{u}\}^{t+\Delta t} = \{\mathbf{F}\}_{ext} - \{\mathbf{F}\}_{int} - [\mathbf{m}]\{\mathbf{a}\}^{t+\Delta t} + \{\mathbf{f}\}^{vis} + \{\mathbf{f}\}^{spring} \tag{3.38}$$

with:

$$\{\mathbf{f}\}^{vis} = -A_{bound} [\mathbf{T}]^T [\mathbf{k}][\mathbf{T}]\{\mathbf{u}_{\mathbf{x},\mathbf{y}}\} \tag{3.39}$$

where $[\mathbf{k}]$ is the spring stiffness coefficient matrix, $\{\mathbf{u}_{\mathbf{x},\mathbf{y}}\}$ is the vector of displacement in terms of the Cartesian coordinate system. Splitting the displacement vector $\{\mathbf{u}\}$ into the sum of the previous displacement and the incremental displacement (i.e. $\{\mathbf{u}\}^{t+\Delta t} = \{\mathbf{u}\}^t + \{\Delta \mathbf{u}\}^{t+\Delta t}$). Then following the same procedures as in equation (3.32) with the modified Newton-Raphson scheme, the equilibrium equation now becomes:

$$\Big([\mathbf{K}] + \frac{4[\mathbf{m}]}{\Delta t} + [\mathbf{k}]_{vis} + [\mathbf{k}]_{spring} \Big)^t \{\Delta \bar{\mathbf{u}}\}_{k+1}^{t+\Delta t} = \{\mathbf{F}\}_{ext}|_k^{t+\Delta t} - [\mathbf{m}] \Big(\frac{4\{\Delta \bar{\mathbf{u}}\}_k^{t+\Delta t}}{\Delta t^2} - \frac{4\{\bar{\mathbf{v}}\}^t}{\Delta t} - \{\bar{\mathbf{a}}\}^t \Big) \{-\mathbf{F}\}_{int}|_k^{t+\Delta t} + \{\mathbf{f}\}_{vis}|_k^{t+\Delta t} + \{\mathbf{f}\}_{spring}|_k^{t+\Delta t} \tag{3.40}$$

Similar to the viscous boundary, all the terms $[\mathbf{K}], \{\mathbf{F}\}_{ext}, \{\mathbf{F}\}_{int}, [\mathbf{m}]$ are computed with equations (2.23), (2.32), (2.34) and (2.35), while $[\mathbf{k}]_{vis}, \{\mathbf{f}\}_{vis}$ are determined using equations (3.35) and (3.43). Finally, the spring force and stiffness matrix are formed as follows:

$$[\mathbf{k}]_{spring} = \sum_{i=1}^{nbn} l_i [\mathbf{T}]^T [\mathbf{k}][\mathbf{T}] \tag{3.41}$$

$$\{\mathbf{f}\}_{spring} = -\sum_{i=1}^{nbn} l_i [\mathbf{T}]^T [\mathbf{k}][\mathbf{T}] \Big(\{\bar{\mathbf{u}}_i\}^t + \{\Delta \bar{\mathbf{u}}_i\}_k^{t+\Delta t} \Big) \tag{3.42}$$

where $\{\bar{\mathbf{u}}_i\}^t$ is the nodal displacement of the previous time step and $\{\Delta \bar{\mathbf{u}}_i\}^{t+\Delta t}$ is the incremental nodal displacement at the current configuration of the iteration k.

3.2.2. Dynamic boundaries with DM-GC

It is important to remark that this framework mainly uses GIMP shape functions and shape function gradients to interpolate the internal and external force vector with the DM technique to improve the stiffness calculation, while the CMPM technique is there mainly to enhance the stress recovery. Therefore, the boundary nodes (i.e. inner nodes *nin* and side nodes *nsn*) needed for the calculations of the viscous force, viscous stiffness, viscoelastic force and viscoelastic stiffness as in equations (3.34), (3.35), (3.41) and (3.42), are located once at the external boundary of all activated elements.

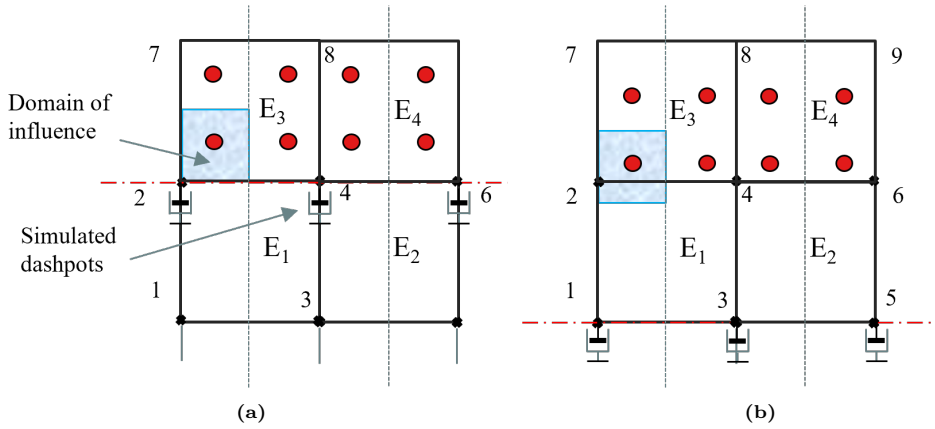

Figure 3.8: Surface nodes determination with GIMP, a) Before deformation and b) After material points displace

Figure 3.8 displays two possible scenarios during simulations. At the initial condition, the boundary nodes are node 2,4 and 6 as shown in figure 3.8a. This means dynamic boundary conditions are implied at these nodes (as displayed with simulated dashpots). However, when material points displace, even if the material point has not jumped from the initial element E_3 to the lower element E_1 (figure 3.8b), the boundary nodes activated are now nodes 1, 3 and 5 where dynamic boundaries are imposed, due to the fact that element E_1 is activated.

3.3. Implementation of DBC to MPM using interpolation of shape functions

The dynamic boundary has been implemented to MPM in section 3.2 following the conventional approach to impose boundary conditions with FEM. This approach requires tracking of background mesh's boundary nodes, which is complicated once material points displace. A more natural method of implying boundary conditions to MPM using interpolation with shape functions at the boundary material points will be discussed in this section.

3.3.1. Implementation with basic MPM

Here, it is proposed to have the viscous and viscoelastic boundary implemented in MPM by interpolation using shape functions. The idea is to have a pre-defined layer of boundary particles where the viscous force and viscoelastic force are acting on. As can be seen in figure 3.10, the boundary stress (i.e. viscous and viscoelastic stress) is applied directly at the location of boundary particles (i.e. material points in blue). The boundary force can now be computed as a product of the stresses acting on particle and the corresponding surface area. Basic MPM does not clearly define the domain of each material point, but this area is approximately determined equal to be a half of a background element size ($\Delta x/2$ in this case).

Figure 3.9 shows two possible scenarios of imposing dynamic boundary conditions in MPM. It can be seen that the boundary forces are interpolated to the corresponding nodes (nodes 7, 8, 9, 2, 4, and 6 as in figure 3.9a, nodes 2, 4, 6, 1, 3, and 5 as in figure 3.9b). As can be seen, if a material point jumps into another element, the boundary band will immediately change as the new element is activated. Note that the linear shape functions N are used with basic MPM.

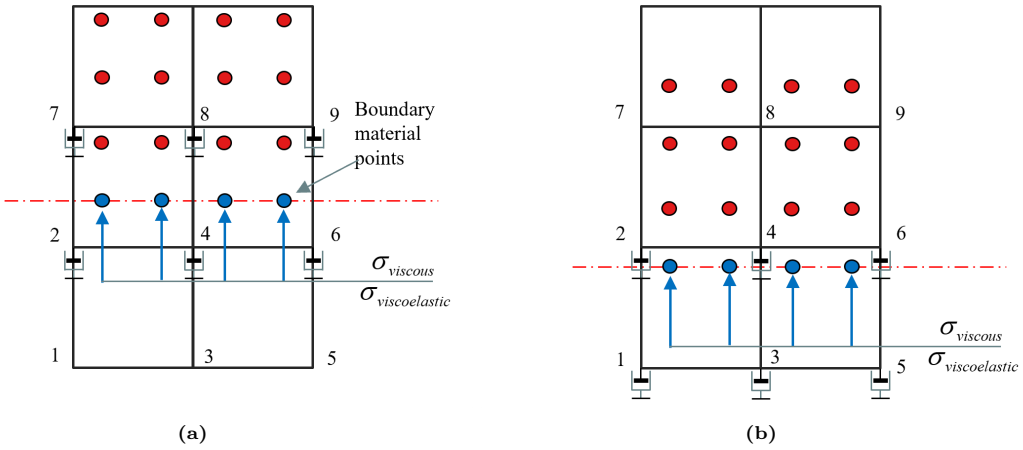

Figure 3.9: Basic MPM with boundary particles where dynamic boundary stresses are applied, a) Before deformation and b) After material points jump to other elements

The implementation formulation is similar to equation (3.40), except now the boundary force and boundary stiffness are determined as follows:

$$[\mathbf{K}]_{vis} = \frac{2}{\Delta t}\frac{\Delta x}{2}\sum_{p=1}^{bmps}\rho_p[\mathbf{N}]^T[x_p][\mathbf{T}]^T[\mathbf{C}][\mathbf{T}][\mathbf{N}][x_p] \tag{3.43}$$

$$\{\mathbf{F}\}_{vis}|^{t+\Delta t} = -\frac{\Delta x}{2}\sum_{p=1}^{bmps}\rho_p[\mathbf{N}]^T[x_p][\mathbf{T}]^T[\mathbf{C}][\mathbf{T}][\mathbf{N}][x_p]\left(\frac{2\{\Delta\bar{\mathbf{u}}\}_k^{t+\Delta t}}{\Delta t} - \{\bar{\mathbf{v}}\}^t\right) \tag{3.44}$$

$$[\mathbf{K}]_{spring} = \frac{\Delta x}{2}\sum_{p=1}^{bmps}[\mathbf{N}]^T[x_p][\mathbf{T}]^T[\mathbf{k}][\mathbf{T}][\mathbf{N}][x_p] \tag{3.45}$$

$$\{\mathbf{F}\}_{spring}|^{t+\Delta t} = -\frac{\Delta x}{2}\sum_{p=1}^{bmps}[\mathbf{N}]^T[x_p][\mathbf{T}]^T[\mathbf{k}][\mathbf{T}][\mathbf{N}][x_p]\left(\{\bar{\mathbf{u}}\}^t + \{\Delta\bar{\mathbf{u}}\}_k^{t+\Delta t}\right) \tag{3.46}$$

Note that the equation with viscous boundary can be obtained by ignoring the *spring* terms $[\mathbf{K}]_{spring}, \{\mathbf{F}\}_{spring}$ in equation (3.40)

3.3.2. DBC in DM-GC with interpolation

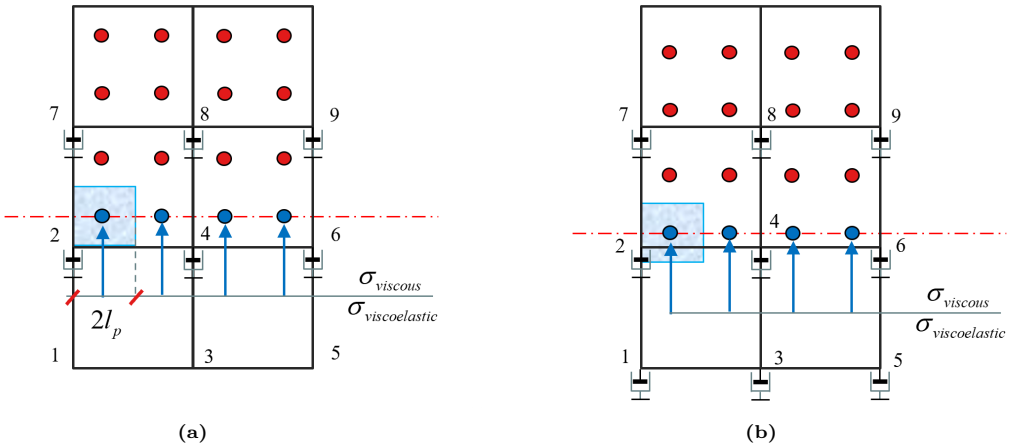

Figure 3.10: Boundary particles and corresponding nodes, a) Before deformation and b) After material points displace

Figure 3.10 shows two possible scenarios when dynamic boundary conditions are implemented in the DM-GC framework using interpolation of shape functions. Figure 3.10a displays the scenario when the material point's support domain is completely inside an element. However, if the material point displaces and its support domain overlaps more than one element, the boundary band and number of corresponding nodes will increase, as can be seen in figure 3.10b. Note that with the DM-GC framework, the GIMP shape functions are used for interpolation. Therefore, the boundary stiffness matrices and force vectors can still be computed similar to equations (3.43) to (3.46), but the linear shape function $[\mathbf{N}]$ is replaced by the GIMP shape function $[\mathbf{S}_{ip}]$, and the boundary area now is exactly $2l_p$ where l_p is a half size of a material point's support domain. As a result, the dimension of the displacement vector will change based on the number of corresponding nodes.

3.4. Implementation

Integration of the viscous stiffness and the viscous force can be done directly at the boundary nodes in a similar way as shown in the previous section. The nodal velocity is needed to compute the viscous force while with the viscoelastic, the nodel displacement is determined additionally as:

$$\bar{v}_i^t = \frac{\sum_{p=1}^{nmps} \rho_p v_p^t N_i(x_p)|J|W_p}{\sum_{p=1}^{nmps} v_p^t N_i(x_p)|J|W_p} \tag{3.47}$$

$$\bar{u}_i^t = \frac{\sum_{p=1}^{nmps} \rho_p u_p^t N_i(x_p)|J|W_p}{\sum_{p=1}^{nmps} v_p^t N_i(x_p)|J|W_p} \tag{3.48}$$

The viscoelastic equations share similarities with the viscous equations, therefore the calculations steps are alike to what have shown in table 3.1. The viscous stiffness $\{\mathbf{k}_{vis}\}$ can be calculated by modifying the diagonal terms corresponding to the boundary nodes. Similar to FEM, the shape functions values are zero for nodes which are not located at the surface boundary.

In table 3.1, the calculation steps for applying the viscous and viscoelastic boundary are shown. The Quasi Loop performs the Newton-Raphson iteration scheme, where the nodal displacement $\{\bar{\mathbf{u}}\}$ is updated as a function of the stiffness and resultant load (equation equations (3.33) and (3.40)). The external load vector, the mass and the stiffness matrix remain unchanged during iterations, therefore they are determined before entering the loop, together with the boundary stiffness contribution to reduce the computational cost. Dynamic terms based on updates of displacement, velocity and acceleration are the kinematic, internal and boundary force are updated every iteration. The Yield and plasticity loop are not part of the thesis. The reader is directed to Gonzalez Acosta (2020) for further reading. Finally, after the update phase, the locations of new boundary nodes will be re-determined as the material point positions are changed.

Table 3.1: Calculation steps with the viscous or viscoelastic boundary (implicit MPM)

1. Interpolations of body force, acceleration, velocity and displacement from particles to nodes:
- $\{\mathbf{b}\}^t$ *equation* (2.17)
- $\{\bar{\mathbf{a}}\}^t$ *equation* (2.38)
- $\{\bar{\mathbf{v}}\}^t$ *equation* (3.47)
- $\{\bar{\mathbf{u}}\}^t$ *equation* (3.48)

2. Integrate stiffness matrix and body mass:
- $\{\mathbf{m}\}^t$ *equation* (2.24)
- $\{\bar{\mathbf{K}}\}^t$ *equation* (2.32)

3. Integrate viscous stiffness vector and spring stiffness vector:
Determine transformation of axis matrix:
- $\{\mathbf{T}\}$ *equation* (3.29)

Integrate over surface nodes for viscous stiffness:
- $\{\mathbf{k}_{vis}\}^t$ *equations* (3.34)*and* (3.43)

Integrate over surface nodes for spring stiffness:
- $\{\mathbf{k}_{spring}\}^t$ *equations* (3.41)*and* (3.45)

4. Integrate external load vector
- $\{\mathbf{F}_{ext}\}^{t+\Delta t}$ *equation* (2.17)

Initialise zero nodal displacement:
- $\{\bar{\mathbf{u}}\} = 0$

5. Time step: $j \rightarrow t + \Delta t$
Quasi Loop, iteration k
Integrate internal force vector:
- $\{\mathbf{F}_{int}\}_k^{t+\Delta t}$ *equation* (2.18)

Update acceleration, velocity and nodal displacement (Newmark's scheme):
- $\{\bar{\mathbf{v}}\}_k^{t+\Delta t}$ *equation* (2.29)
- $\{\bar{\mathbf{a}}\}_k^{t+\Delta t}$ *equation* (2.28)
- $\{\bar{\mathbf{u}}\}_k^{t+\Delta t}$ *equation* (2.27)

Update kinematic force vector, viscous force and spring force vector:
- $\{\mathbf{F}_{vis}\}_k^{t+\Delta t}$ *equations* (3.35)*and* (3.44)
- $\{\mathbf{F}_{kin}\}_k^{t+\Delta t}$ *equation* (2.33)
- $\{\mathbf{F}_{spring}\}_k^{t+\Delta t}$ *equations* (3.42)*and* (3.46)

If viscous boundary is used:
  Solve nodal displacement $\{\bar{\mathbf{u}}\}_{k+1}^{t+\Delta t}$ with equation (3.33)
Else If viscoelastic boundary is used:
  Solve nodal displacement $\{\bar{\mathbf{u}}\}_{k+1}^{t+\Delta t}$ with equation (3.40)
End If
Update acceleration $\{\bar{\mathbf{a}}\}_{k+1}^{t+\Delta t}$
Compute the material trial stresses $[\boldsymbol{\sigma}_p]_{k+1}^{trial}$
Yield Loop
If $Y\left[\sigma_p\right]_{k+1}^{trial} > 0$: return stresses to the yield surface Y
  Plastic iteration loop
  If $Y\left[\sigma_p\right]_{k+1}^{t+\Delta t} = 0$: EXIT Yield Loop
END Yield Loop
Update material point stresses with plasticity $[\boldsymbol{\sigma}_p]_{k+1}^{t+\Delta t} = [\boldsymbol{\sigma}_p]_{k+1}^{trial}$
Check convergence criteria: EXIT Quasi Loop
END Quasi Loop

6. Update phase: particle accelerations, velocities, positions and locate boundary nodes
- $\{\mathbf{v}\}_p^{t+\Delta t}$ *equation* (2.41)
- $\{\mathbf{a}\}_p^{t+\Delta t}$ *equation* (2.39)
- $\{\mathbf{x}\}_p^{t+\Delta t}$ *equation* (2.42)

3.5. Transformation between quasi-static and dynamic analysis

The non-reflecting boundary formulations allow particles at the boundary to displace instead of having them fixed. On the other hand, calculation of the initial stress state with the gravity requires fixed conditions. Therefore after the initial stress state is generated with quasi-static analysis using equation (2.37) with the fixed boundaries, dynamic analysis is then performed with absorbing boundaries.

After the quasi-static phase is completed, the fixed boundary is switched off and is replaced by absorbing boundaries. This means there should be a replacement for the fixed boundary to prevent any downward movement due to the body force. In FEM, the boundary does coincide with the physical edges, therefore the fixed boundary can be replaced with the spring conditions, provided the dynamic phase to be transited smoothly. This is called the "penalty method". The author directs to Griffiths (2004) for further reading.

In MPM, it is relatively complicated to transfer between these analysis stages. Because the background mesh boundaries do not coincide with the physical edges, methods such as the penalty method can not be applied easily. The task, therefore remains unsolved.

In this thesis, the fixed condition is still used for generating initial conditions. Note that only the gravitation is considered as a source of external force, hence the equilibrium equation is similar to what has been seen in equation (2.37), where the external force includes only the body force is now calculated as:

$$\{\mathbf{F}\}_{ext}^{t+\Delta t} = \sum_{p=1}^{nmps} \rho_p [\mathbf{N}]^T [x_p] \{\mathbf{b}\}^t |J| W_p \tag{3.49}$$

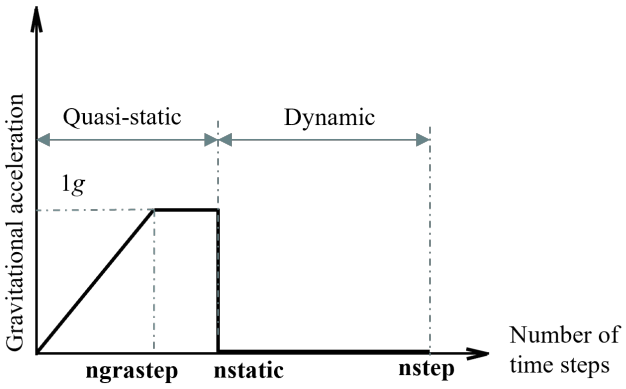

Figure 3.11: Calculation phases illustration

During the quasi-static stage, the gravitation load is gradually increased each time step until the gravitational reaches $1g$. During simulation with the total number of time steps **nstep**, the gravitational force is calculated for **ngastep** = 50 time steps, then the $1g$ condition is kept constant until the number of time steps reaches **nstatic** = 60 time steps, as shown in figure 3.11. After that, the dynamic analysis takes place. Note that the gravitational force has already lead to initial displacement and stresses inside the soil body, therefore, by ignoring the initial displacement, internal stresses and the gravitational force, the dynamic analysis equation can be obtained. In other words, the gravitational acceleration is $0g$ during the dynamic phase as shown in figure 3.11.

Table 3.2: Calculation steps of quasi-static and dynamic phase

1. Interpolations of body force, acceleration, velocity and displacement from particles to nodes (equations (2.38), (3.47) and (3.48))
2. Integrate stiffness matrix and body mass (equations (2.24) and (2.32))
3. Integrate viscous stiffness vector and spring stiffness vector:
Determine transformation of axis matrix, equation (3.29):
Integrate over surface nodes for viscous stiffness with equations (3.34) and (3.43):
Integrate over surface nodes for spring stiffness with equations (3.41) and (3.45)
4. Integrate external load vector with equation (2.17)
Initialise zero nodal displacement:
$\{\bar{\mathbf{u}}\} = 0$
If: $j <$ **nstatic**: Quasi-static analysis (fixed boundary):
5. Quasi Loop, iteration k
Solve nodal displacement $\{\bar{\mathbf{u}}\}_{k+1}^{t+\Delta t}$ with equation (2.37)
Compute the material trial stresses $[\boldsymbol{\sigma}_p]_{k+1}^{trial}$
Yield Loop
Update material point stresses with plasticity $[\boldsymbol{\sigma}_p]_{k+1}^{t+\Delta t} = [\boldsymbol{\sigma}_p]_{k+1}^{trial}$
Check convergence criteria: EXIT Quasi Loop
END Quasi Loop
6. Update phase: particle's positions:
$\{\mathbf{x}\}_p^{t+\Delta t}$ *equation* (2.42)
If: $j =$ **nstatic**:
Save the initial material point's stresses: $[\boldsymbol{\sigma}_p]^t|^{ini} = 0$
Reset the dynamic material point's stresses to zero: $[\boldsymbol{\sigma}_p]^t|^{dyn} = 0$
If: $j >$ **nstatic**: Dynamic analysis (dynamic boundary):
7. Quasi Loop, iteration k
Integrate internal force vector (using equation (2.18) but with the dynamic material point stresses $[\boldsymbol{\sigma}]_p^t|^{dyn}$):
Update acceleration (equation (2.29)), velocity (equation (2.28)) and nodal displacement (equation (2.27)) (Newmark's scheme):
Update kinematic force vector (equation (2.33)), viscous force (equations (3.35) and (3.44)) and spring force vector (equations (3.42) and (3.46)):
If viscous boundary is used:
Solve for nodal displacement with equation (3.33)
Else If viscoelastic boundary is used:
Solve for nodal displacement with equation (3.40)
End If
Update acceleration $\{\bar{\mathbf{a}}\}_{k+1}^{t+\Delta t}$
Compute the material point trial stresses $[\boldsymbol{\sigma}_p]_{k+1}^{trial}$
Yield Loop
If $Y\left[\sigma_p\right]_{k+1}^{trial} > 0$: return stresses to the yield surface Y
Plastic iteration loop
If $Y\left[\sigma_p\right]_{k+1}^{t+\Delta t} = 0$: EXIT Yield Loop
END Yield Loop
Update the total material point stresses with plasticity $[\boldsymbol{\sigma}_p]_{k+1}^{t+\Delta t}|^{tot} = [\boldsymbol{\sigma}_p]_{k+1}^{trial}$
Calculate the dynamic material point stresses: $[\boldsymbol{\sigma}]_{k+1}^{t+\Delta t}|_p^{dyn} = [\boldsymbol{\sigma}_p]_{k+1}^{t+\Delta t}|^{tot} - [\boldsymbol{\sigma}_p]^t|^{ini}$
Check convergence criteria: EXIT Quasi Loop
END Quasi Loop
8. Update phase: particle accelerations, velocities, positions and locate boundary nodes with equations (2.39), (2.41) and (2.42)

Calculation steps considering both quasi-static phase and dynamic phase now is shown in table 3.2. It can be seen that calculation steps for quasi-static phase is similar to what have shown in the dynamic

phase, except that all the inertia terms are excluded. During the quasi-static stage, the acceleration and velocity of material points are zero. The Yield loop exists to ensure that the increments of gravitational acceleration is sufficiently small to stabilize the simulation. The transition between two stages illustrates that only the input dynamic loading can result in the dynamic material point stresses $[\boldsymbol{\sigma}_p]^t|^{dyn}$. After the quasi-static phase is completed, the initial material point's stresses (i.e. $[\boldsymbol{\sigma}_p]^t|^{ini}$) are determined, the dynamic phase takes place using the absorbing boundary condition. At the begining of this stage, $[\boldsymbol{\sigma}_p]^t|^{dyn} = 0$. Then the Yield loop is performed with the stress inside the yield surface (in elastic range) is: $[\boldsymbol{\sigma}_p]^t|^{tot} = [\boldsymbol{\sigma}_p]^t|^{ini} + [\boldsymbol{\sigma}_p]^t|^{dyn}$. Once the total material point stresses (i.e. $[\boldsymbol{\sigma}_p]^{t+\Delta t}|^{tot}$) are determined incorporated with the yield surface, the dynamic material point stresses can be calculated as shown in table 3.2. Note that after the quasi-static stage, the internal force is calculated with the dynamic material point stresses.

4

Benchmarks

4.1. Introduction

In this section, 2 benchmarks are investigated to validate the implementation of dynamic boundaries. First, the 1D benchmark problem is investigated with two scenarios: small-deformation and large deformation. Later, results of a 2D symmetrical plane strain model will be presented.

4.2. 1D column

4.2.1. Small deformation

Two 1D column models under a dynamic load with small magnitudes will be presented. Non-harmonic load and harmonic load function will be applied to the top of the soil column to validate the absorption of dynamic boundaries.

Non-harmonic dynamic load

Figure 4.1 illustrates the one-dimensional column under dynamic loading, with elastic parameterseters Young's modulus $E = 20MPa$, Poisson's ratio $\nu = 0.25$, density of $\rho = 1500kg/m^3$. The geometry of the column is shown in figure 4.1a, with the ratio between height and width as $H/D = 100 > 10$, to make sure a 2D model can accurately represent one-dimensional properties. The background mesh is discretised with 2D-quadrilateral element of size $\Delta x = \Delta y = 0.25m$, each element initially contains 4 material points equally distributed. There are a total of 6400 points located in the initial active elements. The background mesh is set to have an additional column of elements at the right and left side of the column, while an additional 7 rows of elements are added to the bottom and one additional row of elements is inserted at the top to ensure that there is sufficient space for particle movements, as shown in figure 4.1c.

Roller conditions are applied along the left and right boundary, allowing only vertical movement. To test the efficiency of the viscous boundaries, different boundary conditions are simulated at the bottom surface separately as: a) fixed boundaries; b) viscous boundary; and c) viscoelastic boundary, to compare their effects on wave propagation. Boundary conditions are implied in the way which is shown in section 3.2.1 as this method is similar to what has been done in FEM. Six measuring points, A, B, C, D, E and F are located throughout the column with a fixed distance between points of 20m, to record the stress history during simulation as can be seen in figure 4.1b.

The first type of dynamic load applied is the Dirac Delta function as shown in figure 4.2. The load has a peak of 10kN, which is equal to a distributed stress of $F_{peak}/D = 10kPa$ applied at the top of the column. The period of the incident wave is chosen to be 0.1 seconds as this period is relevant to many geotechnical problems. time step size is set to be $\Delta t = T_{load}/20 = 0.005s$. The simulation time is 2.5s to ensure that the wave has sufficient time to transmit through the entire column and reflect back (if there is a spurious reflection).

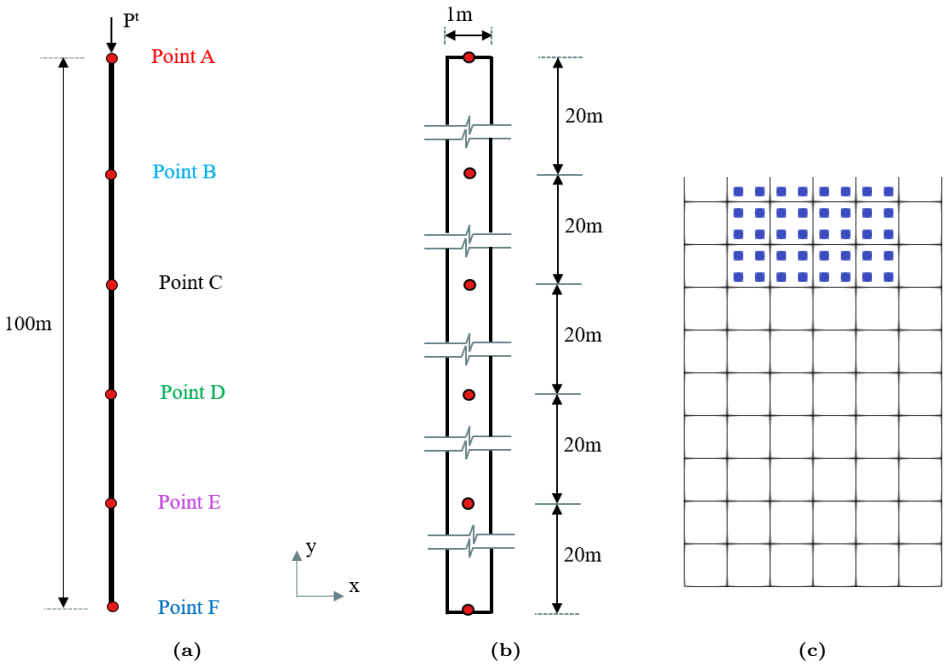

Figure 4.1: Description of the benchmark, a) Geometry of the column, b) Locations of measuring points, c) Discretised model at the bottom of the soil column

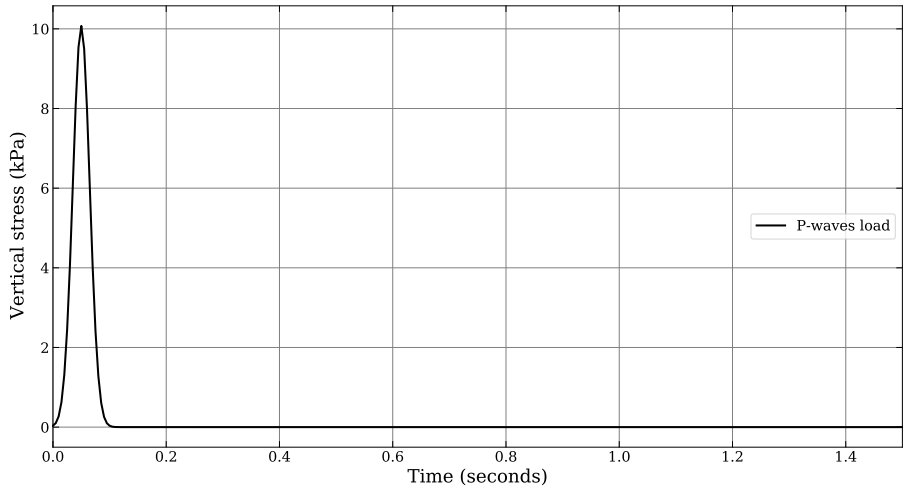

Figure 4.2: Incident P-wave with Delta load function with duration $T = 0.1s$

The load function is zero initially and then increases to the peak of $P_{peak} = 10kPa$ in 0.1 seconds. The Dirac load function is expressed as follow:

$$f(t) = \delta_a(t) = \frac{0.375}{a\sqrt{\pi}} e^{-\left(\frac{t-t_0}{a}\right)^2} \tag{4.1}$$

where $t_0 = 0.05$ is time in which the load reaches its peak, t is time and $a = 0.021$ is the chosen coefficient. With the given soil properties, the compressional wave velocity is computed to be equal to $C_p \approx 131m/s$. During the simulation, the domain is assumed to be homogeneous. With this simplification, the total time that the P-wave needs to travel throughout the column is $t_{travel} = H/C_p = 100/131 \approx 0.76$ seconds. Moreover, the analytical solution suggests that the stress magnitude of an arbitrary point in the domain should be closely equal to the $P_{peak} = 10kPa$ during the propagation, and the duration of

stress increment should be 0.1 seconds. The compressional velocity of soil particle is approximated to be:

$$v^p \approx \frac{P_{peak}}{\rho \times C_p} = \frac{10kPa}{1500kg/m^3 \times 131m/s} \approx 0.051m/s \tag{4.2}$$

The response displacement solution can be expressed as:

$$u(t) = \frac{1}{2\pi}\int_{-\infty}^{\infty} G(\omega)F(\omega)e^{i\omega t}d\omega \tag{4.3}$$

where $u(t)$ is the displacement response of the system to the input signal, $G(\omega)$ is the Green's response function in the frequency domain ω, $F(\omega)$ is the Fourier transform of the load function and i is the imaginary unit.

With the input Dirac load function, the Fourier transform function of the input load can be computed as:

$$F(\omega) = \int_{-\infty}^{\infty} f(t)e^{-i\omega t}dt \tag{4.4}$$

$$F(\omega) = \int_{-\infty}^{\infty} \frac{0.375}{a\sqrt{\pi}} e^{-\left(\frac{t-t_0}{a}\right)^2} e^{-i\omega t}dt = 0.375e^{-i\omega t} \tag{4.5}$$

With given duration of load is 0.1 seconds, the angular frequency of the input signal is:

$$\omega = \frac{2\pi}{T} \approx 62.8(rad/s) \tag{4.6}$$

The response function $G(\omega)$ can be determined as follows:

$$G(\omega) = \frac{1}{k - \omega^2 m + i\omega c} \tag{4.7}$$

where k is the stiffness of the considering system, m is the mass and c is the damping coefficient. For simplicity, the solution is carried out with the assumption that the system is homogeneous and elastic, c is chosen to be zero. The Young'modulus is $E = 20MPa$ resulting in a stiffness value of $k = 2000(tons/m^2)$, the density of the soil is $\rho = 1500kg/m^3 = 1.5(tons/m^3)$. Considering material point that has a volume of C_p, with a cell size of 0.25 m inserted 4 material points, the material point's mass is determined as:

$$m = \rho C_p = 1.5tons/m^3 \cdot 1m \cdot 0.125m \cdot 0.125 \approx 0.0234tons \tag{4.8}$$

Therefore the response function in the frequency domain is determined as:

$$G(\omega) = \frac{1}{2000 - 0.0234\omega^2} \tag{4.9}$$

Finally, combining equations (4.5) and (4.9) to equation (4.3), the vertical displacement response of a material point at the top soil column, at the peak time $t = 0.05s$ is approximated as:

$$u(t = 0.05) = \frac{1}{2\pi}\int_0^{62.8} \frac{0.375}{2000 - 0.0234\omega^2} e^{-0.05i\omega} e^{0.05i\omega} d\omega \tag{4.10}$$

$$u(t = 0.05) \approx 0.0087 \cdot tan^{-1}\Big(0.003423265984\omega\Big)\Big|_0^{62.8} \approx 0.0019(m) \tag{4.11}$$

Figure 4.3 shows the result of simulation with fixed boundary condition. The propagation of wave is clearly shown, as well as the spurious reflection. time that the vertical stress reaches its peaks at point A ($y = 0m$) is $t \approx 0.05$ seconds and at point F ($y = 100m$) is $t \approx 0.8$ seconds. This means that the travel time of the incident wave is nearly 0.75 seconds, approximately equal to t_{travel}, as computed above. Another thing worth pointing out is that the differences in peak stress recorded at each point is approximately equal to one fifth of t_{travel}, since all six measuring points are evenly spaced over the column.

After the load reaches the bottom, it is trapped inside the domain, and keeps bouncing back and fort endlessly. The incident compressional wave is reflected at the bottom, but does not change the wave form, therefore the reflected wave also has negative stress, but travels to the top column. This reflection stress peaks the top (point A) at time of approximately $1.6 seconds$ with no significant build-up of stress. The wave is then reflected with same amplitude but opposite sign to the bottom, since the free boundary condition at the top cannot transmit waves. Clearly, the wave propagates with almost no attenuation for the first 20 m, as the stress peak recorded at point B is 10 kPA, then it starts to attenuate and the peak magnitude decreases with travelled distance. Moreover, oscillations with higher frequencies are observed at point C, D and E, after stress reaches the highest magnitude. Since the top boundary is free, these high-frequency oscillations occur with higher magnitude after the wave is reflected at the top.

The reflection does not only cause the stress record to be inaccurate with respect to time but also with respect to magnitude. The stress recorded at point F is twice as high as the stress at point E because at this point, both an incoming and a reflected wave meet each other in phase. These waves are in sync resulting in an amplified stress amplitude in this point.

Figure 4.4 shows the stress record of the six measuring points of the viscous and viscoelastic model, respectively. While point A and F are specifically chosen at the top and bottom of the model (top and bottom material points) to explore the behaviour of these singularity points, results obtained at the remaining points should display a representative behaviour of the particles inside the domain as well as the wave propagation. It is clear that the vertical stress at the top of the soil column has jumped from zero to the peak value of approximately $7.5 kPa$, then quickly dropped to zero again, with an exact duration of 0.1 seconds, in correspondence with the applied load.. The magnitude, however, is lower than the given $10 kPa$. This is a common problem in MPM in which input forces are applied using shape functions. Dealing with this issue is not part of this thesis and the phenomena does not significantly affect overall outputs of simulations.

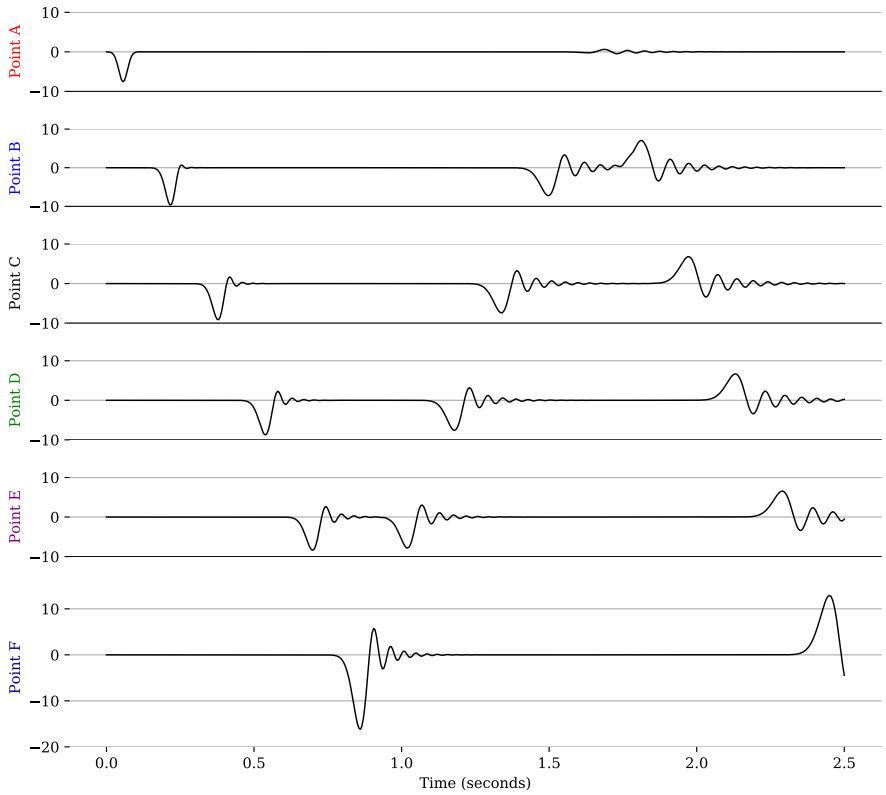

Figure 4.3: Vertical stress history (kPa) of measuring points with fixed boundary

The viscous and the viscoelastic boundary are shown to almost perfectly absorb the spurious reflections,

while the fixed condition cannot, as shown in figure 4.4. With the viscous and viscoelastic model, the incoming load function reaches to the bottom at time 0.8 seconds after the simulations started, then it is transmitted completely through the boundary, and no more reflection is observed after $t = 0.8seconds$.

The peak stresses obtained with the viscous and the viscoelastic boundary are approximately $10kPa$, which is what to be expected. However, the stress recorded at point F is only $6kPa$, critically smaller than stress at point E. A possible reason for this is the fact that the load, which is transmitted at this location, will lead to a reduction of the recorded stress.

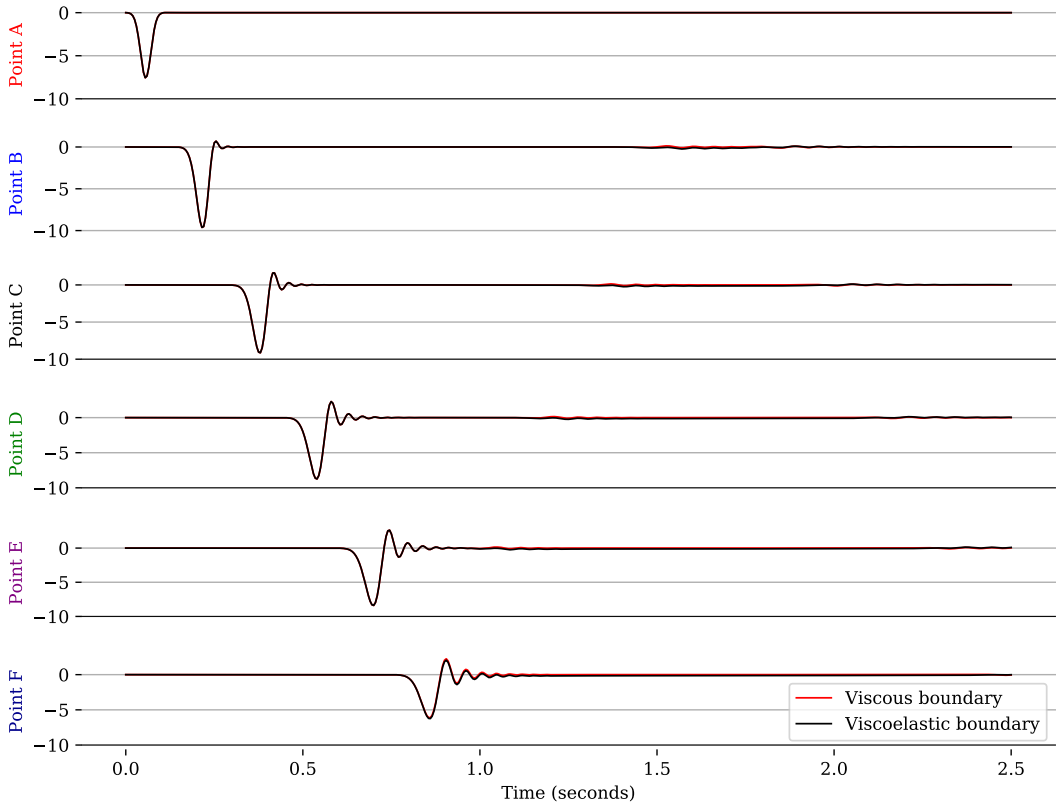

Figure 4.4: Vertical stress history (kPa) of measuring points with viscous and viscoelastic boundary

Figure 4.5 shows the displacement recorded at measuring points. As can be seen, the peak displacement obtained is approximately 0.002 m, which closely agrees with the predicted displacement of 0.0019 m (equation (4.11)). The reflection is well-displayed. First, the input load results in downward displacements of all measuring points, then the wave is reflected at the bottom and it travels from the bottom to the top (point F back to point A). This results in recovery of the displacement over the column. This suggests that if the wave reflected at the fixed boundary is negative but travels in the positive direction (y^+), the displacement will be positive together with an upward movements of particles. However, this does not agree with the case when the wave is reflected at the free boundary. As soon as it reaches the top and get reflected, the stress changes the sign to positive, while the wave reflected downwards, and the displacement observed is positive. The answer for this phenomena is that the reflection at the fixed boundary does change both the wave forms and their directions of propagation, leading to opposite displacements of the incoming wave as a rebound effect, while the free boundary reflects waves but keeps the wave forms and only changes the propagation directions, therefore it results in displacements with same directions as the propagated waves.

The displacements with the viscous and viscoelastic boundary are shown in figure 4.6. Both models have predicted the peak displacement well, with no reflection of waves. The viscous model has shown to result in a permanent displacement of 0.002 m, while the viscoelastic model has shown a recovery of the system in which the displacement observed to gradually decreased, after the wave has been transmitted

at the bottom. This phenomena represents real-life behaviour of the soil, however, it is not sufficient to conclude whether the recovery effect is accurate or it is just numerical artifact.

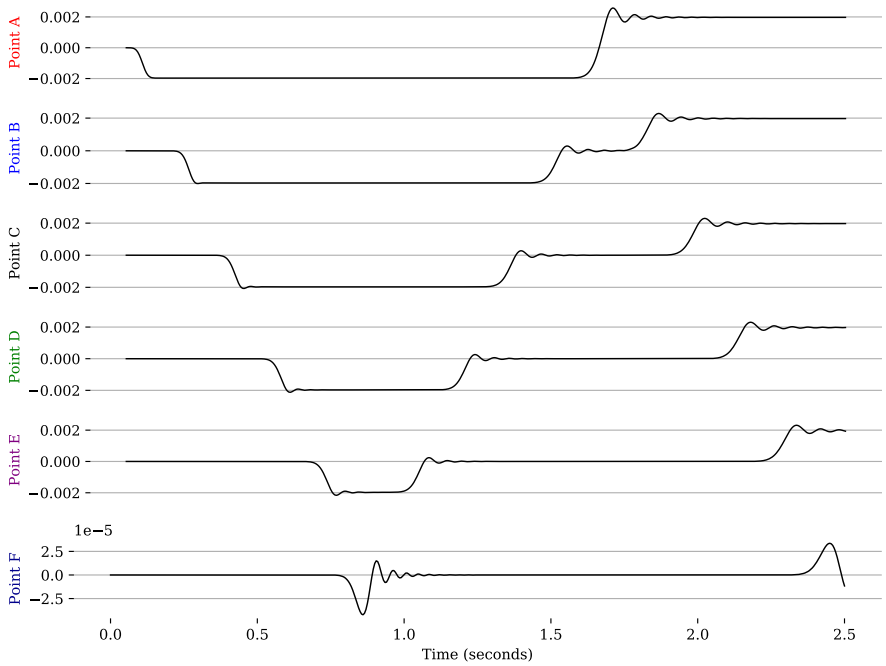

Figure 4.5: Vertical displacement (m) of measuring points with fixed boundary

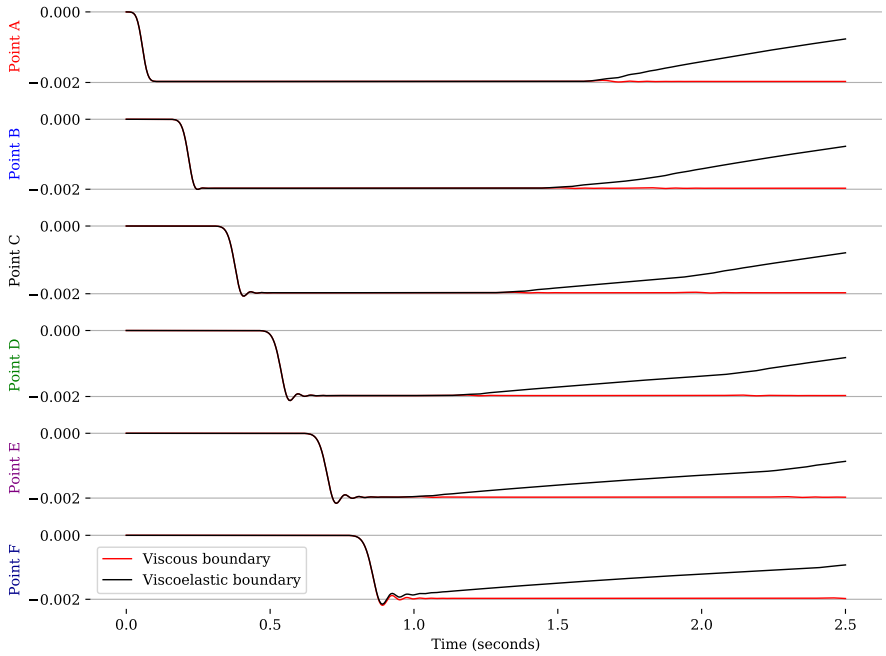

Figure 4.6: Vertical displacement (m) of measuring points with viscous and viscoelastic model

The velocities of all measuring points with the fixed model and models with dynamic boundaries are shown in figures 4.7 and 4.8, respectively. All three models predicted a maximum velocity which is approximately 0.05m/s. This is in agreement with the analytical solution shown above. The reflection at the fixed boundary results in the movement of particles in the opposite direction as compared to the incoming signal. While the free boundary also reflects the waves but it is not able to change the

direction of particles movement. The viscous model and the viscoelastic model have shown to absorb perfectly, and their results are nearly identical. As discussed above, the boundary transmits the input signal leading to a decrease in stress at the boundary (see figure 4.4), but the velocity magnitude is preserved. The peak velocity of point F is approximately 0.045m/s, which does not deviate significantly from the average velocity of 0.05m/s over the column.

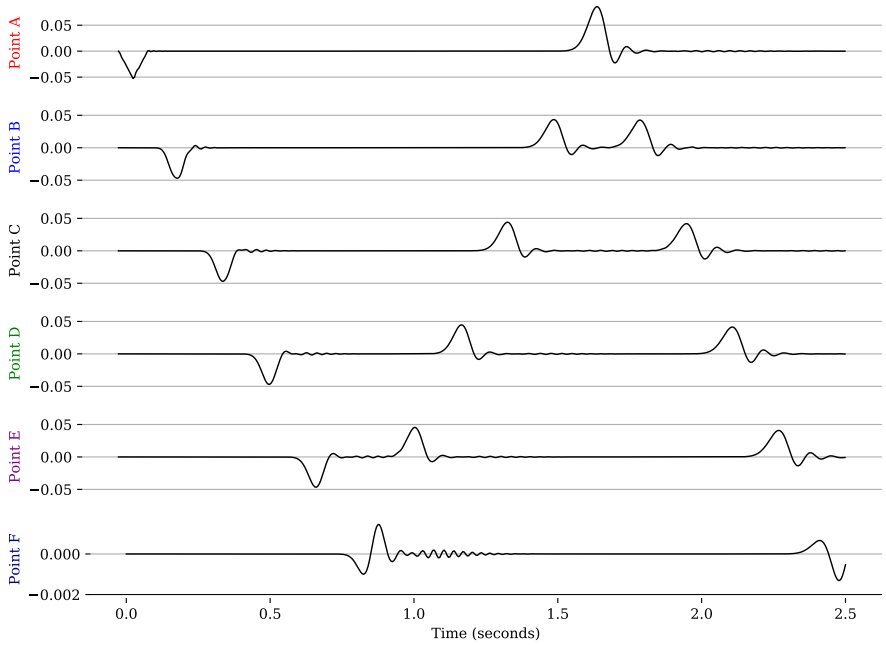

Figure 4.7: Vertical velocity history (m/s) of measuring points with fixed boundary

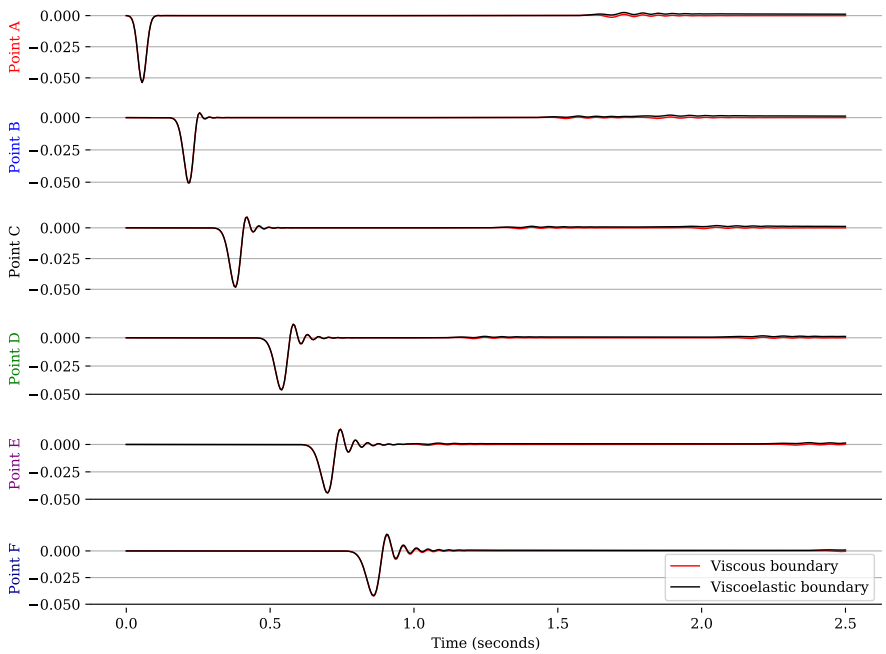

Figure 4.8: Vertical velocity history (m/s) of measuring points with viscous and viscoelastic boundary

Harmonic dynamic load

The soil column with the exact same soil properties as in the previous section is modelled with the boundary placed closer to the excitation's location, in order to reduce the computational time. The

column's height now is reduced to $H = 20$, while the width is kept to be equal to 1m, as shown in figure 4.9 . Three measuring points are located at the top, middle and bottom of the soil column. The discretisation and background mesh is alike the case of non-harmonic load function.

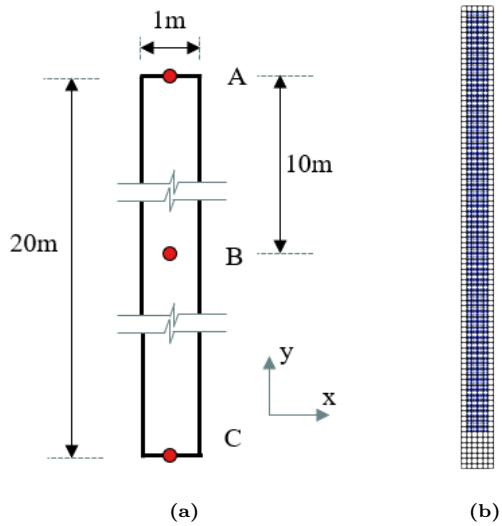

Figure 4.9: Description of the benchmark, a) Geometry of the column with locations of measuring points, c) Discretised model

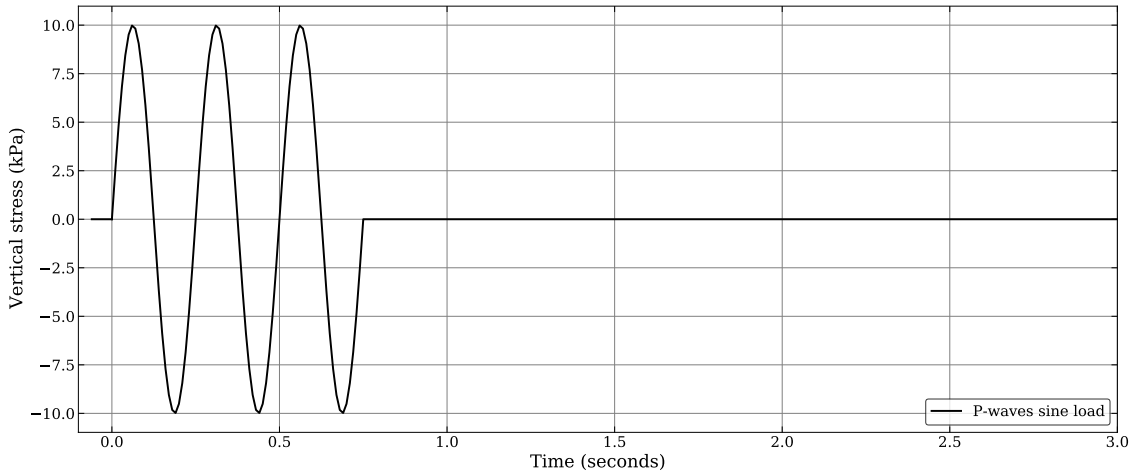

Figure 4.10: Incident P-wave with sine way load function

The Delta load function is replaced with a harmonic sine wave load function. Figure 4.10 illustrates the dynamic load that is implied at the top of the column. The wave consists of 3 small sine waves which can be expressed as:

$$P(t) = P_0.sin(\omega t) \tag{4.12}$$

where $P_0 = 10kPa$ is the wave amplitude, $\omega = 2\pi/T$ is the angular frequency of each wave with the duration of $T = 0.25$ seconds. The total loading time is 0.75 seconds, covered by 75 time steps of $\Delta t = 0.01$ seconds. An additional model of a soil column with extended mesh of $H = 300m$ will be used as the reference solution. The height of 300 m is to make sure that no reflection can be observed during the simulation. Note that reflection still occurs with the extended model if the simulation time is large enough. However, this model can represent the ideal condition in which the input signal is transmit to the infinite region perfectly. Figure 4.11 shows the stress history of the three measuring points considering different boundaries. The fixed model appears to have chaotic reflections inside the model since the waves are trapped inside the domain, causing significant

inaccuracies of stress recorded. The waves are amplification each other when they meet, increasing the peak stress and making the stress phase incorrect. As can be seen in figures 4.11b and 4.11c, the fixed model's stress history is completely different with the extended mesh fixed model as the 3 sine waves interact with each other. The peak stress obtained is nearly $20kPa$ for the middle while this value is $30kPa$ at the bottom. Both the viscoelastic and the viscous model have shown impressive results in which they transmit almost all the incoming waves, this is also the case with the extended mesh, which is what to be expected. However, at time $t \approx 0.8$ seconds (figure 4.11b) and $t \approx 1.0$ second (figure 4.11c), there are some minor reflections observed with the viscoelastic model.

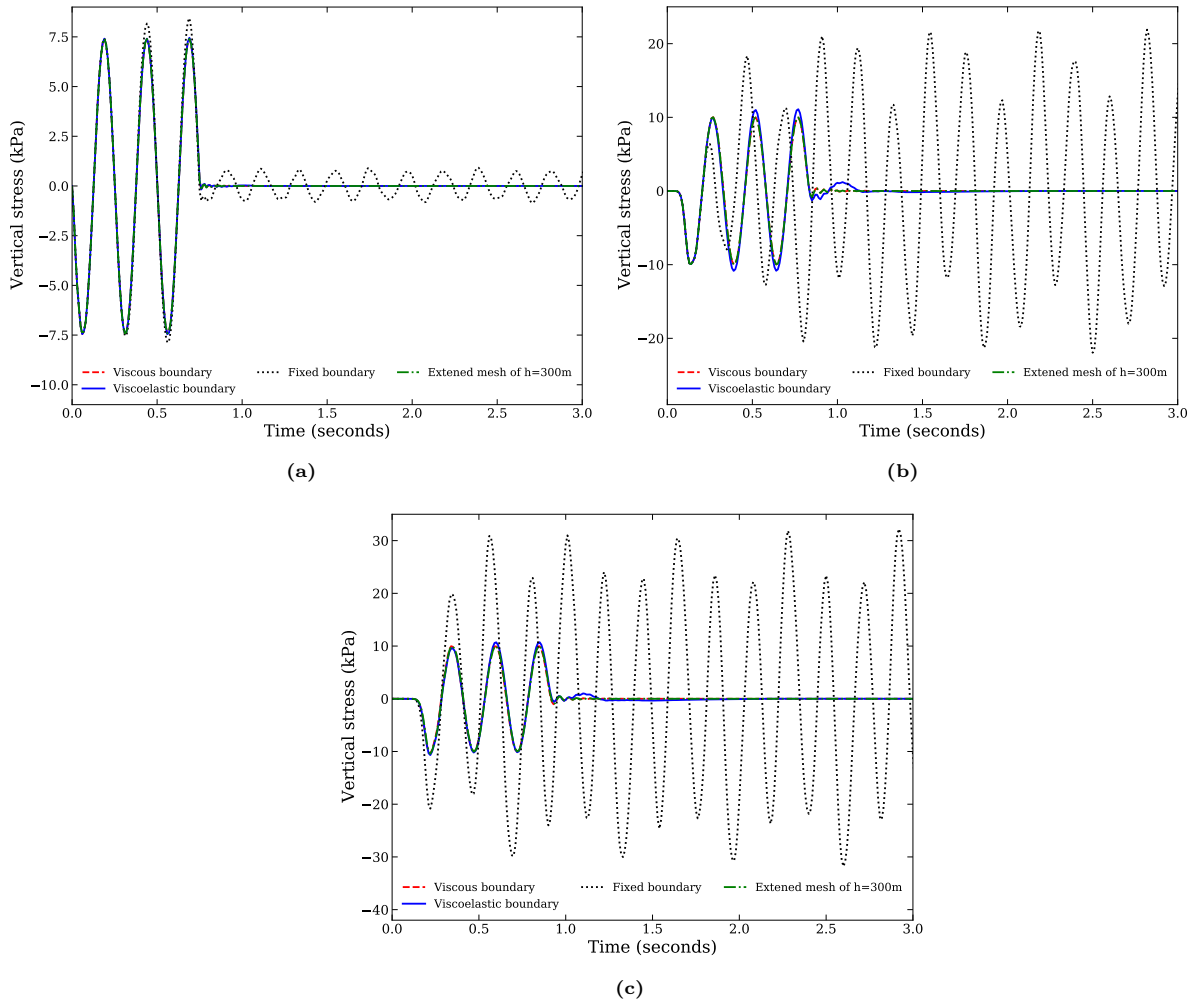

Figure 4.11: Stress history, a) At the top of the column, b) At the middle of the soil column and c) At the bottom of the column

Figure 4.12 displays the vertical displacement and velocity at the three measuring points. The fixed model output is inaccurate, as the model predicts incorrect peak displacements or velocities at the top and middle (figures 4.12c and 4.12d). The viscous boundary appears to have a better performances compared to the viscoelastic model, although both models results show nearly perfect absorption with the velocity. However, the viscoelastic model seems to fail when there are many of incoming waves. This can be attributed to the fact that the incoming waves react with the numerical stiffness property, resulting in errors.

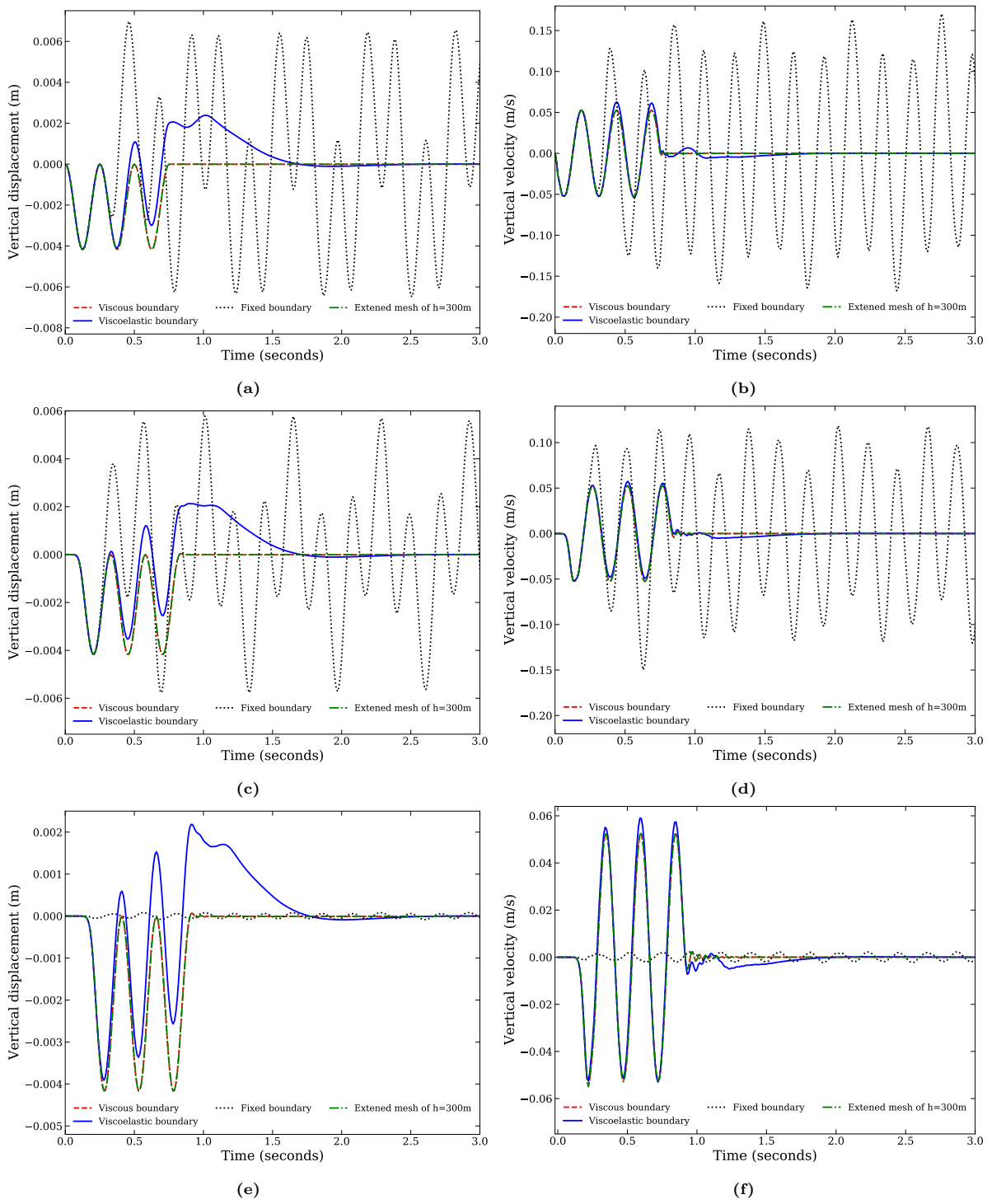

Figure 4.12: Displacement and velocity histories, a) Displacement at the top, b) Velocity at the top, c) Displacement at the middle, d) Velocity at the middle, e) Displacement at the bottom and d) Velocity at the bottom

To conclude, the spurious reflection caused by the use of fixed boundary can lead to inaccurate stress records, both in time and magnitude. The reaction between the incoming waves and the reflected ones can result in larger stress waves recorded. In case there are multiple input signals, the fixed model usually fails to predict time that stress or displacement reach its peaks. The extended mesh indeed can represent the propagation of input load signal to infinite region, but it does not absorb the reflection, next to this the computational cost is relatively high. Both the viscous boundary and the viscoelastic boundary produce similar response with near perfect absorption of the numerical reflection, for both

harmonic and non-harmonic input load. However, the use of the viscous boundary is preferred with its high accuracy and simplicity.

4.2.2. Large-deformation

The result of dynamic boundaries in MPM with small deformation is relatively impressive. However, stress oscillation has been recognised as one of the most common problem in MPM, especially with large deformation. Therefore, a 20m-high 1D soil column with the same geometry as was the case for small deformation will be tested with large-magnitude dynamic load to investigate the performances of dynamic boundaries in MPM. Discretisation and geometry of the problem is the same as what has been described in figure 4.9. Three measuring points are placed at the top, the middle and the bottom of the column. Figure 4.13 shows the dynamic load, at the top a force of $300kN$ is applied to an area of $1m^2$. It is sufficiently large to make sure the simulation is large-deformation.

The analytical solution for the displacement response of the system is not available, however, the stress recorded of an arbitrary point in the soil body should be approximately to $300kPa$. the peak movement of a soil particle can also be determined as:

$$v^p \approx \frac{P_{peak}}{\rho \times C_p} = \frac{300kPa}{1500kg/m^3 \times 131m/s} \approx 1.53m/s \tag{4.13}$$

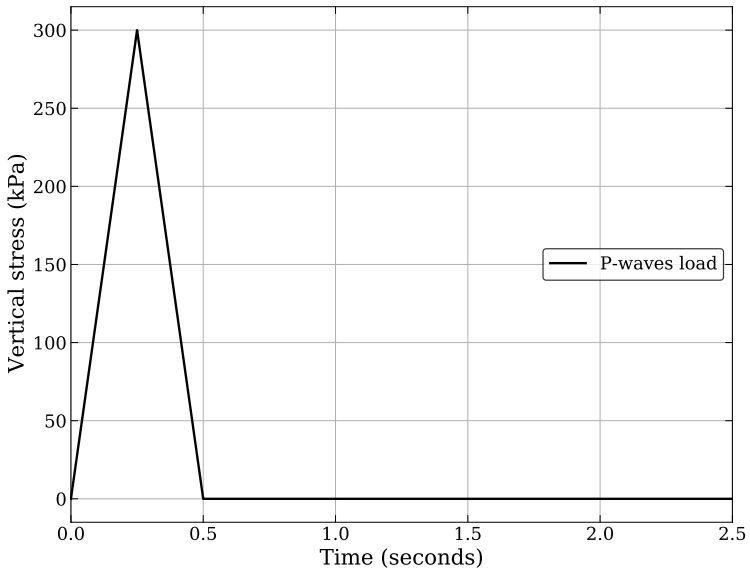

Figure 4.13: Incident P-wave with Delta load function

In this section, implementation of the viscous and viscoelastic boundary will be tested, with two frameworks: basic MPM and advanced MPM with DM-GC technique. Two methods of implementation which have been discussed in sections 3.2 and 3.3 are used to impose dynamic boundaries, as shown in section 4.2.2. Method 1 is similar to the way the boundary is applied in FEM, while method 3 uses the same approach, but with the more advanced framework of MPM. Method 2 and 4 are proposed to pre-define the outer layer of boundary particles and use interpolation with shape function to impose boundary condition. GIMP shape functions are applied with method 4 while linear shape functions are used with method 2.

Table 4.1: Combinations to impose dynamic boundary

Combination to apply DBC		Method 1	Method 2	Method 3	Method 4
Framework	Basic MPM	Yes	Yes	-	-
	DM-GC	-	-	Yes	Yes
Implementation	Surface nodes	Yes	-	Yes	-
	Interpolation with SFs	-	Yes	-	Yes

Figure 4.14 shows the stress records at the measuring points with all three selected boundary conditions. Overall, the results are relatively poor. Nevertheless, there are some remarkable things worth pointing out. It is clear that the vertical stress is integrated incorrectly at the top column (figures 4.14a, 4.14c and 4.14e), as this is a common problem with MPM in which input forces are applied using shape functions. Note that this numerical artifact only affects the stress record of top material points, and exact input stress will be transferred to lower material points in the domain. While stress outputs are poorly displayed with the use of MPM, the DM-GC techniques has shown its improvement with smoothing stress curves and filtering out stress oscillations. The spurious reflection with the use of fixed boundary can be seen clearly. At the bottom, the reflection combines with incoming input load, leading to a stress peak magnitude two times higher than the input load. Results obtained using dynamic boundary conditions are shown with mostly no reflections. Among four given methods to impose DBC, method 4 has shown the best result with the smoothest stress curves, while with method 3, the stress record at the top is nearly identical to method 4, but stress oscillation can still be deducted at the bottom (figures 4.14d and 4.14f). Method 1 shows good absorption of reflections, with clear stress oscillations. Reason for this is that with large-deformation, material points jump from one element to another, the boundary edge therefore keeps moving instantly during the simulation. While method 2 still deducts some reflections as shown in figure 4.14c.

Stress record at the middle of the column is shown in figure 4.15. The spurious reflection is clear shown to influence the stress magnitude as in figure 4.15a. The peak stress is obtained approximately $700kPa$ with basic MPM and nearly slightly higher than $400kPa$ as with DM-GC framework. The dynamic loading signal is trapped inside the column permanently, leading to infinite stress oscillation. The efficiencies of different methods to impose DBC are well-displayed. All methods have predicted the same arrived time of the stress waves of approximately $0.08s$. With the calculated compressional wave velocity is $C_p \approx 131m/s$, time needed for the load to propagate down to the middle point is: $t = 10m/131m/s \approx 0.076s$. This value agrees well with the numerical results. Nevertheless, the result with method 4 outweighs other methods. As can be seen in figure 4.15c, the reflection is perfectly filtered out and no oscillations are observed. Method 1 can absorb the reflection to a remarkable amount but often results in permanent stress after the load propagates, while method 2 cannot absorb the reflection totally and method 3 deducts stress oscillations. Although it is clear that using DM-GC technique improves the stress recovery, as the result with method 3 gives better prediction for the stress curve, the reflections cannot be absorbed properly, as the boundary edge will often be located lower than the physical boundary. This illustrates the excellent advantages of method 4 to impose dynamic boundary conditions, in terms of absorption of numerical reflections, but also elimination of stress oscillation. Note that method 2 with the use of linear shape functions gives the lowest-quality results, while the most promising results are obtained with GIMP shape functions interpolation.

Figure 4.15d shows the comparison of stress records between fixed boundary models and dynamic boundary conditions. It is clear that the fixed boundary always generates the spurious reflections regardless of the used framework. Both basic MPM and DM-GC framework renders inaccuracies in stress magnitude and the presence of multiple unnatural stress waves. The stress curve is smoother with the DM-GC framework than with basic MPM. The peak stress is obtained approximately equal $400kPa$ with DM-GC and nearly $750kPa$ with basic MPM.

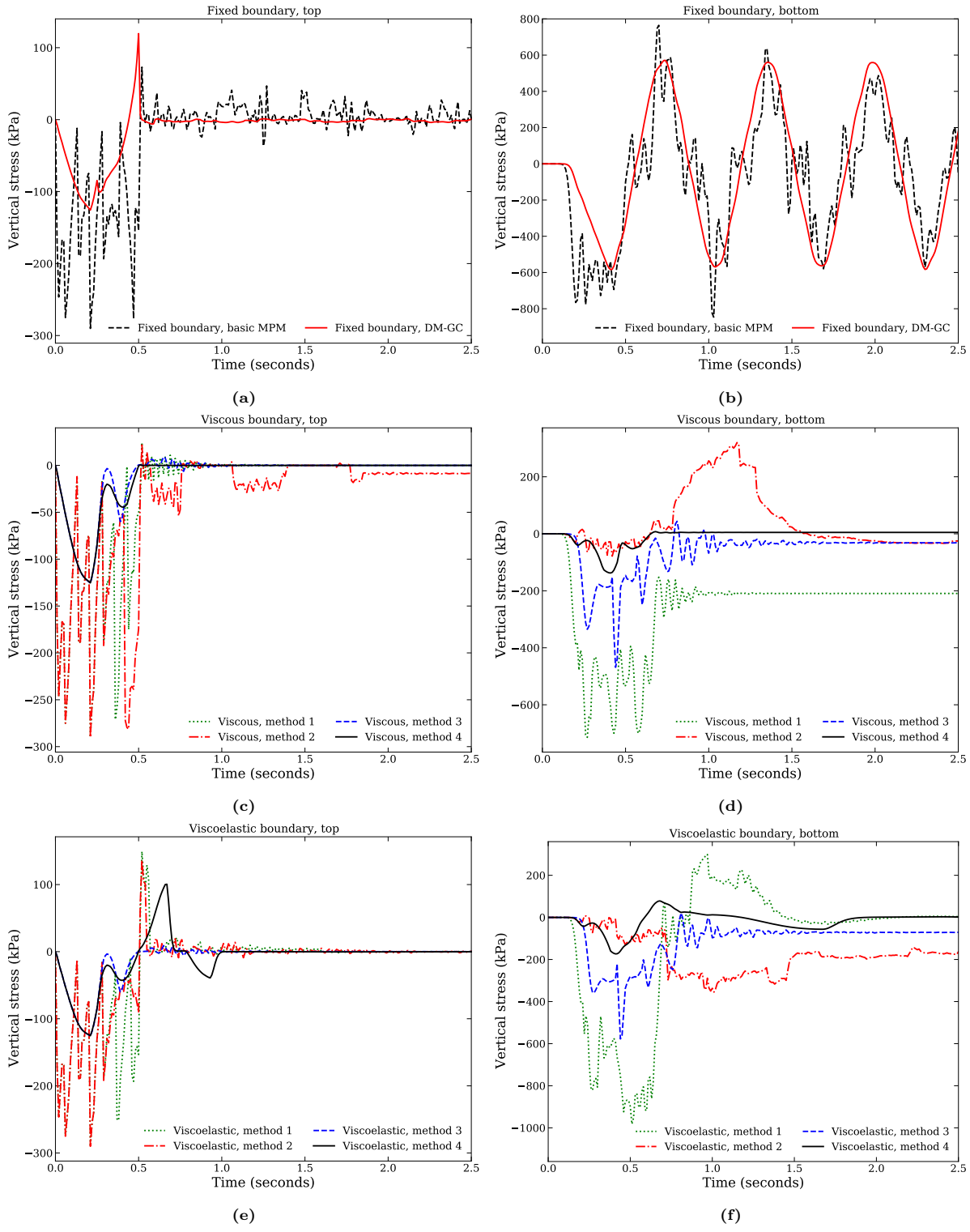

Figure 4.14: Vertical stress record at the top and bottom of the column, (a, b) Top and bot record with the fixed boundary (c, d) Top and bot record with the viscous boundary, and (e, f) Top and bot record with the viscoelastic boundary

This is clearly incorrect as the peak input load is about $300kPa$. This is the interaction effect between incoming load and reflected waves. Note that the compressional wave velocity is $C_p = 131m/s$, therefore at $t \approx 0.076s$ the input signal propagates to the middle point. The signal reaches the bottom at $t \approx 0.152s$, before it gets reflected and reaches the middle point at $t \approx 0.24s$. This explains why the

stress record of the fixed boundary and the dynamic boundary models are identical until $t \approx 0.228s$. It is clear that when both the incoming signal and the reflected waves reach the same location in the domain, they will interact, leading to inaccuracies of stress magnitude. With the viscous and the viscoelastic boundary, no reflections are observed, and the stress peak is nearly $300kPa$, which is what to be expected.

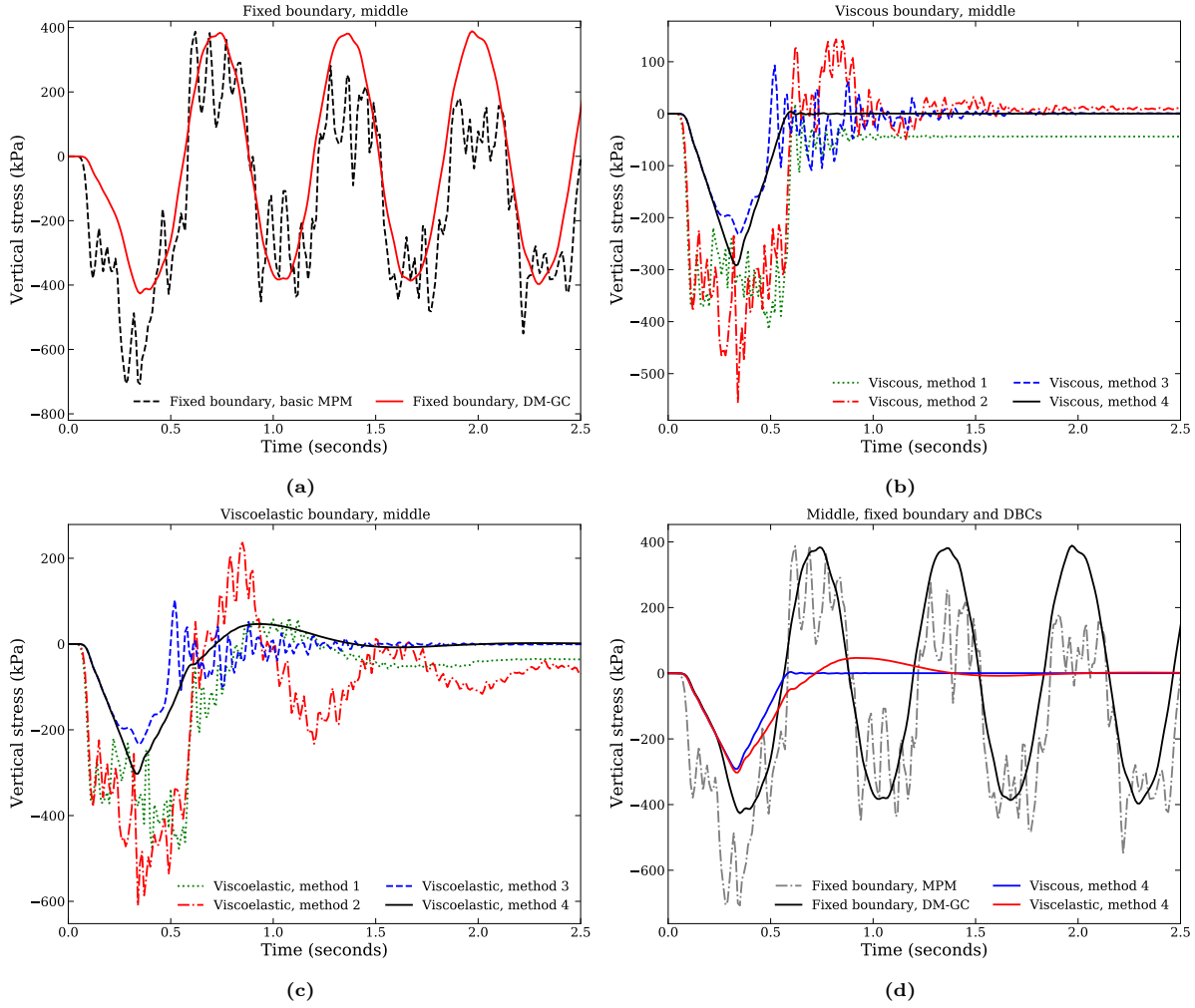

Figure 4.15: Vertical stress history at the middle, a) Fixed boundary, b) Viscous boundary, c) Viscoelastic boundary and, d) Comparison between fixed boundary and DBCs with method 4

Figure 4.16 displays the velocity records at the top of the column with all three testing boundary conditions. As discussed above, the maximum velocity of a soil particle is computed to be approximately $1.53m/s$ which corresponds to the maximum stress of $300kPa$. While the velocity is well-displayed with the use of dynamic boundary conditions, the fixed boundary condition shows some numerical errors. At $t \approx 0.25s$, soil particle's velocity reaches its peak of $1.5m/s$, as shown in figure 4.16a. After the wave is reflected at the bottom boundary, it then propagates back to the top of the column and reaches the maximum velocity of approximately $3.0m/s$. This phenomenon is similar to the amplification of the stress at the bottom as shown in the figure 4.14b, as the top boundary can freely move. This effect can still be observed at the bottom boundary, but in small-scale, as can bee seen in figure 4.16b. Overall, the use of basic MPM results in a velocity record with low-quality. While with the DM-GC framework, the velocity curve is smooth and its change is gradual, following the shape of the input Delta load function, basic MPM gives results with instant jumps and drops in magnitude, which is unrealistic.

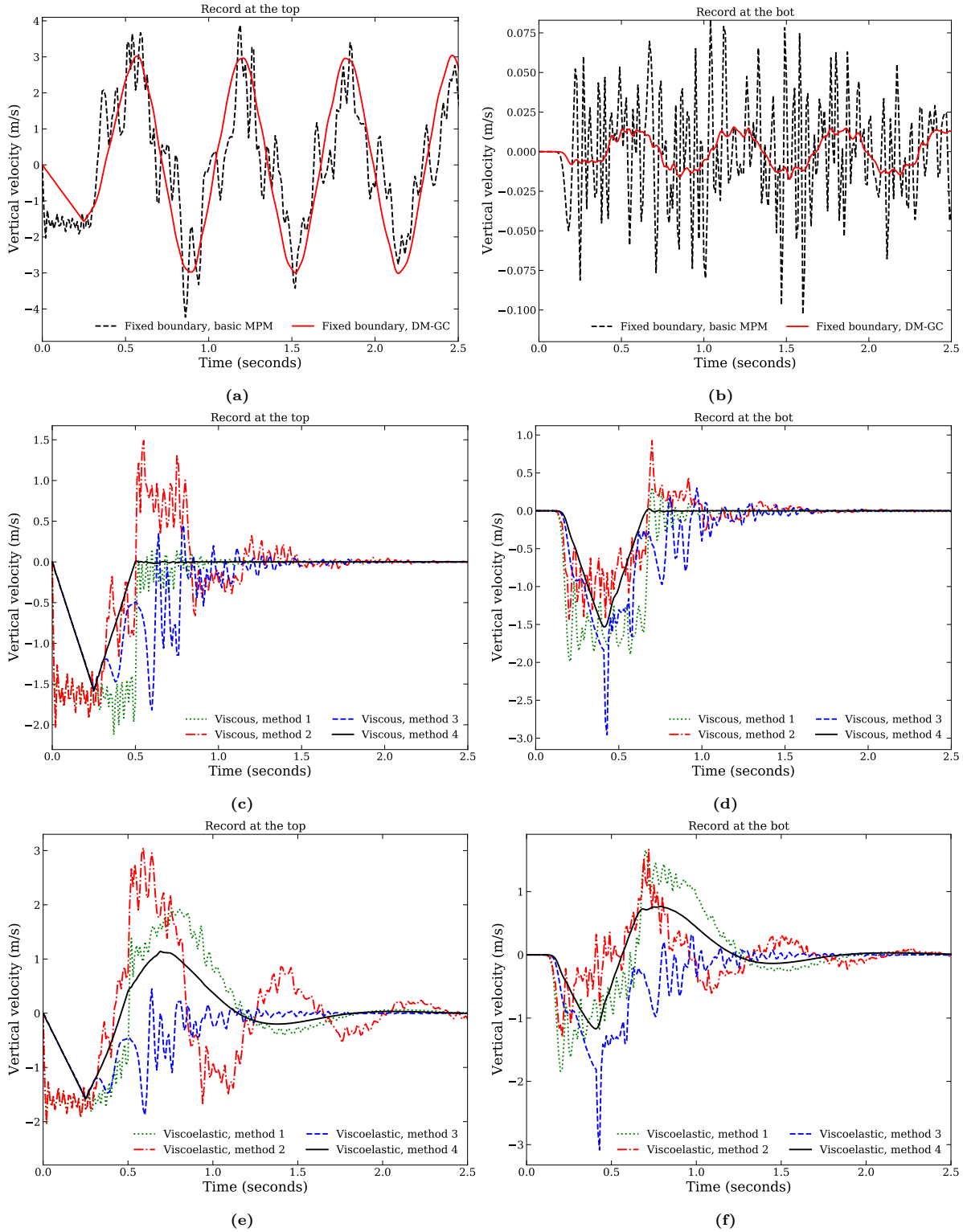

Figure 4.16: Vertical velocity record at the top and bottom of the column, (a, b) Top and bot record with the fixed boundary (c, d) Top and bot record with the viscous boundary, and (e, f) Top and bot record with the viscoelastic boundary

Again, imposing DBC using method 1 can absorb the reflection to a certain amount while still deducting stress oscillations. It is also proven that using GIMP interpolation with shape functions to impose dynamic boundary gives impressive results, while linear shape function interpolations with basic MPM cannot eliminate the numerical reflections, as seen in figures 4.16c and 4.16e. Record with method

3 is also relatively poor. Because the boundary is placed far from the physical domain, it fails to absorbs incoming waves. Finally, it is seen that both the viscous and the viscoelastic boundary give almost identical result. However, the viscoelastic condition shows rebounds of velocity due to its spring contribution.

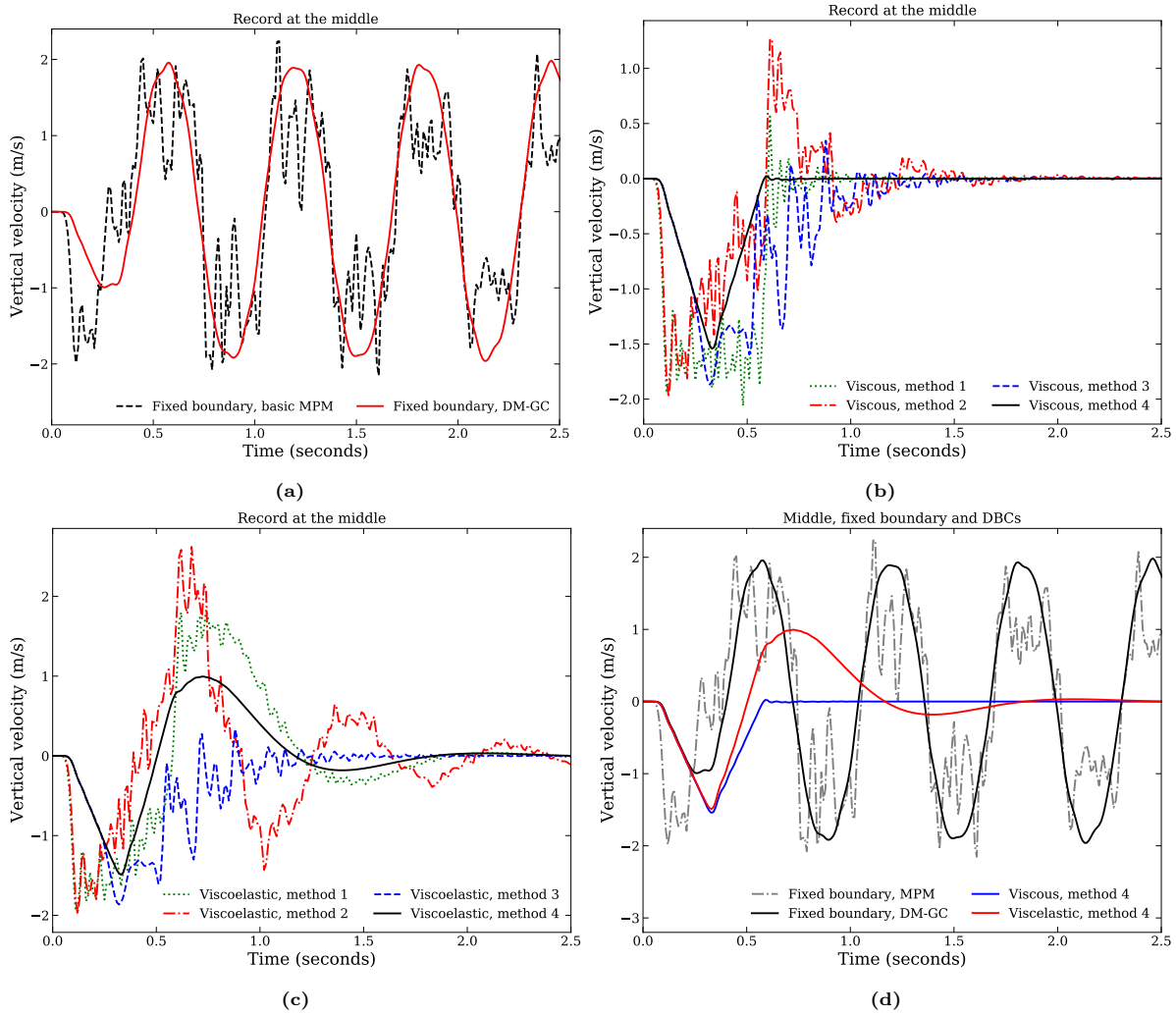

Figure 4.17: Vertical velocity history at the middle, a) Fixed boundary, b) Viscous boundary, c) Viscoelastic boundary and, d) Comparison between fixed boundary and DBCs with method 4

Figure 4.18 illustrates the displacement history of at three measuring points of the fixed boundary comparing to results of dynamic boundaries. Only method 4's results are used to compare, as this method has been proven to give the best performances among the 4 proposed solutions. Overall, the fixed boundary condition shows oscillation of displacement, with the maximums value at the top nearly being $0.5m$ with basic MPM and approximately $0.32m$ with DM-GC technique. The displacement obtained at the middle point is lower, about $0.25m$ and $0.19m$ with basic MPM and DM-GC, respectively. While the viscous model gives permanent displacement of $0.4m$ over the domain, the viscoelastic model displays that the displacement quickly increases to the highest values, then gradually decreases to zero. The reflection of waves clearly affects the displacement record at the middle point of the column, as can be seen in figure 4.18b. The displacement records of fixed boundary and dynamic boundaries are identical until time $t \approx 0.22s$, which is exactly when the reflection waves propagate back to the middle point, as discussed above. As a result, the vertical displacement obtained with the fixed boundary is reduced due to the interactions between the reflection and incoming waves. Finally, the displacement observed with fixed boundary using basic MPM is higher and deviates earlier in time than others. This is because of the instant jumps of stress and velocity, as shown in figures 4.14a and 4.16a.

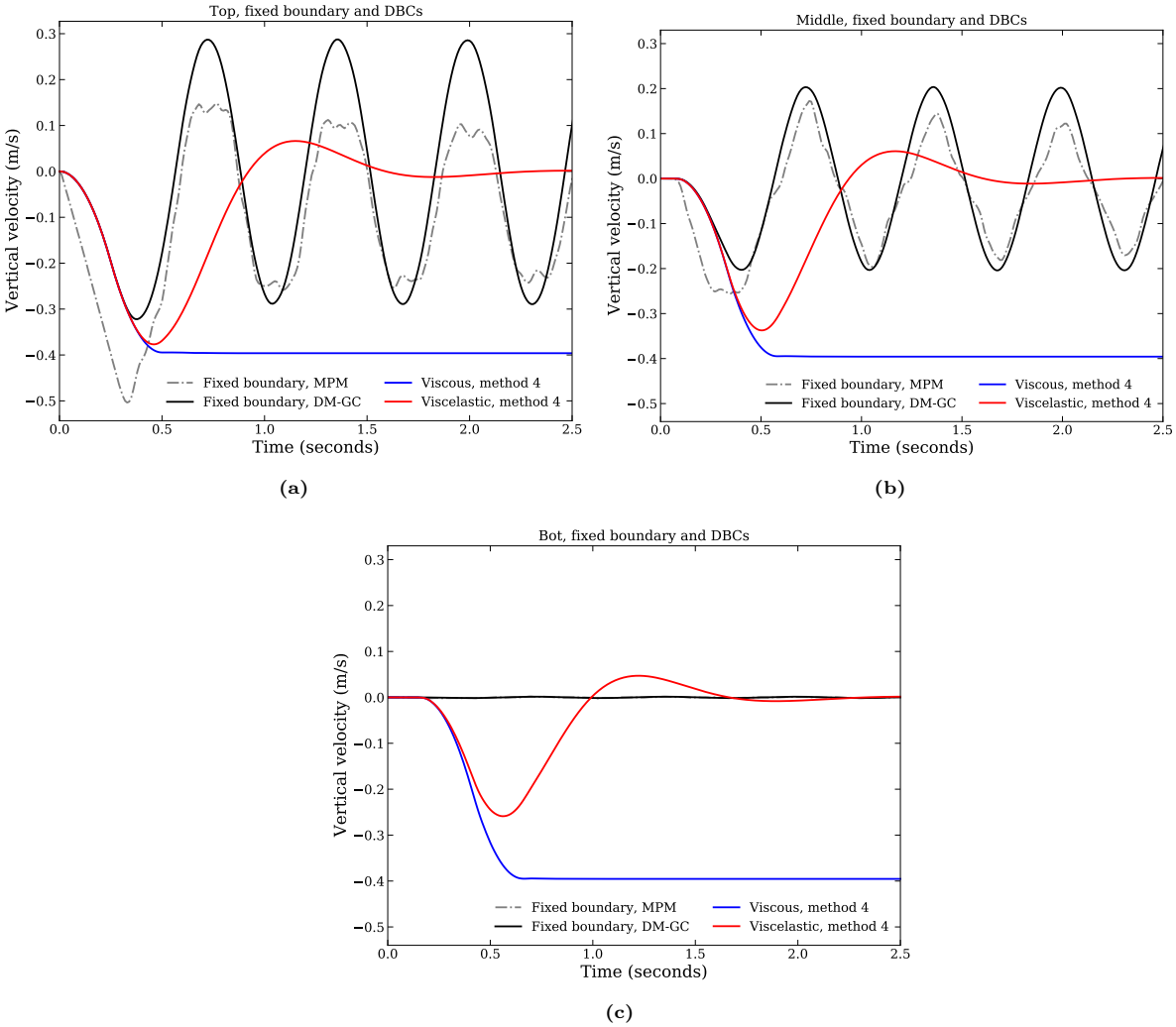

Figure 4.18: Displacement history, a) At the top of the column, b) At the middle of the soil column and c) At the bottom of the column

4.3. 2D symmetrical plane strain model

A two dimensional symmetric elastic model of $4m \times 4m$ under one loading pulse is investigated. Only method 3 of applying DBC is used as this method is proven to give the best output, as discussed in section 4.2.2. Figure 4.19 illustrates the geometry of the problem, with the dynamic point load P applied to the top left hand of the model. Six measuring points are located to record domain's behaviours, as shown in figure 4.19a, with background element sizes of $\Delta x = \Delta y = 0.05m$. Each element contains four material points equally distributed at the centre of element's quadrants. The model's parameters are Young's modulus $E = 20MPa$, Poisson's ratio $\nu = 0.25$, density of $\gamma = 15kN/m^3$. The rollers condition is applied along the left hand side boundary to prevent any horizontal movement, while the absorbing boundary condition are prescribed for the right side and bottom boundary using method 4, which has been shown to be efficient with the previous benchmark. The result is compared to the fixed model using the DM-GC framework instead of basic MPM since both frameworks show similar behaviours but the latter one's result is less smooth than the advanced one. Fully fixed condition is set at the bottom while rollers condition is simulated along the left and right hand edges. The problem was simulated using time step of $\Delta t = 0.01s$.

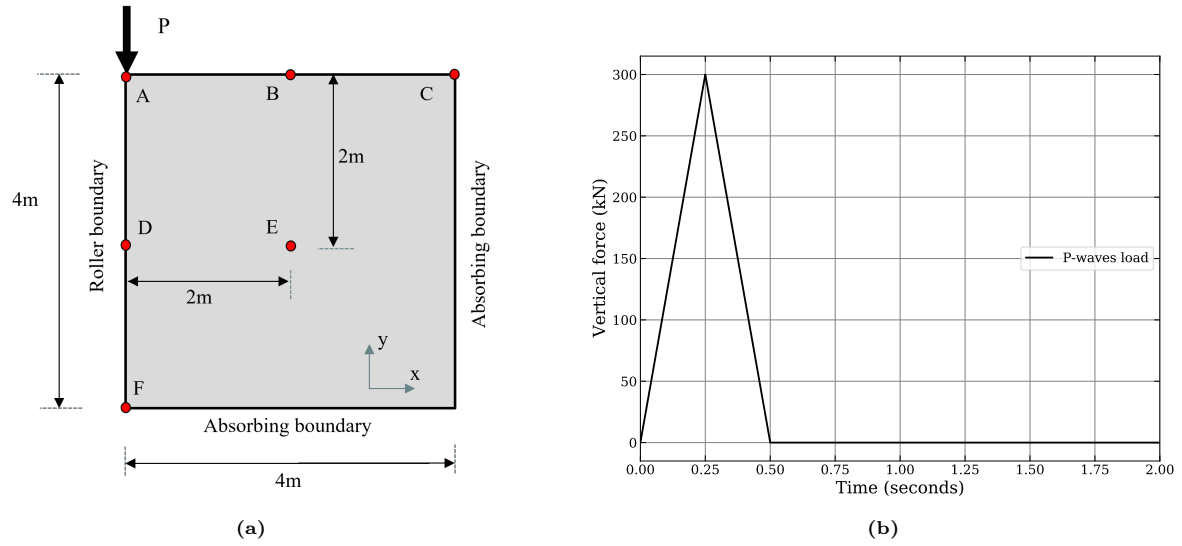

Figure 4.19: Description of the 2D benchmark, a) Geometry of the model and measuring points, c) Dynamic point load

The vertical stress history is shown in figure 4.20. Remind that point load is applied to the top 2 material points in one element, this is equal to having point load applied on the area of one element size. Therefore the maximum stress is: $\sigma_{input}^{peak} = 300/\Delta x = 6000kPa$. However, since the load is input as a point load, its energy is transferred to the whole domain, and therefore the peak stress will quickly decrease. This explains why the peak stress shown in figure 4.20 is smaller than σ_{input}^{peak}.

Overall, both the viscous and viscoelastic boundary absorb almost all the reflections. While the fixed boundary creates reflections of stress inside the domain, leading to non-stop oscillation of stress, as can be seen in figures 4.20b and 4.20c. The amplification of stress at the boundary can be seen in figure 4.20c, as the peak stress recorded with the fixed boundary is nearly 3 times larger than what has been obtained with absorbing boundary.

The horizontal stress results are displayed in figures 4.20d to 4.20f. All three boundaries show an increase in stress to around 20kPa at point B and nearly 10kPa at point C. At point E, all three models display similar behaviour as the soil particle here is compressed and pushed away from the excitation's location. However, at the surface, the fixed model gives positive stress while the viscous boundary gives negative stress. This difference is due to the propagation of surface waves. Since the fixed boundary cannot absorb the surface waves, they are trapped inside the domain.

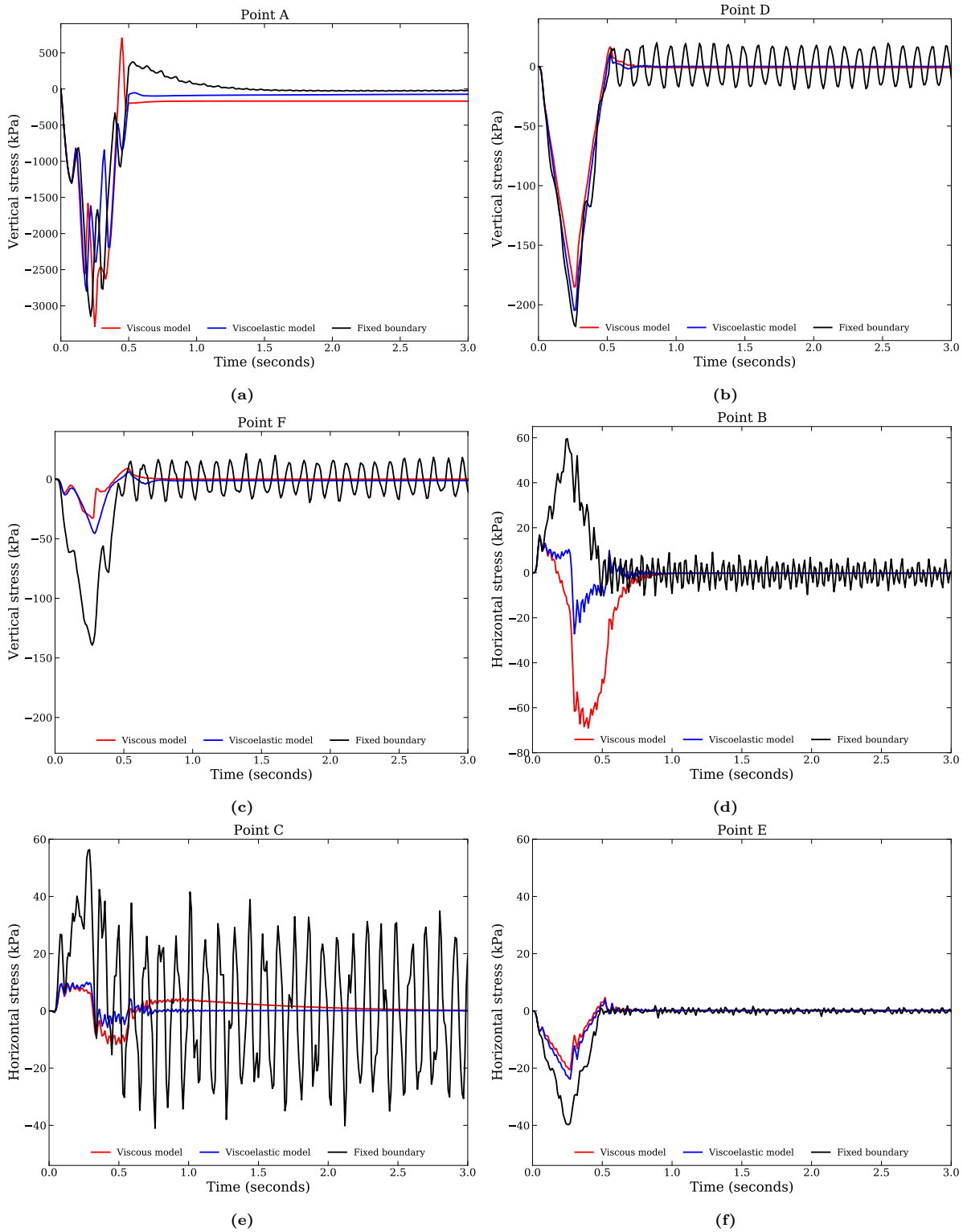

Figure 4.20: Vertical and horizontal stress histories of different measuring points

Visualisations of horizontal stress are shown in figure 4.21 to show the propagation of waves near the surface. point load first creates horizontal stress waves that travels towards the right boundary, as shown in figures 4.21a to 4.21c. However, while the viscous and viscoelastic boundary are shown to absorb the surface waves (figures 4.21e and 4.21f), the surface waves are trapped inside the domain with the fixed boundary as shown in figure 4.21d. To conclude, the horizontal stress is calculated more

precisely with the absorbing boundaries than with the fixed model.

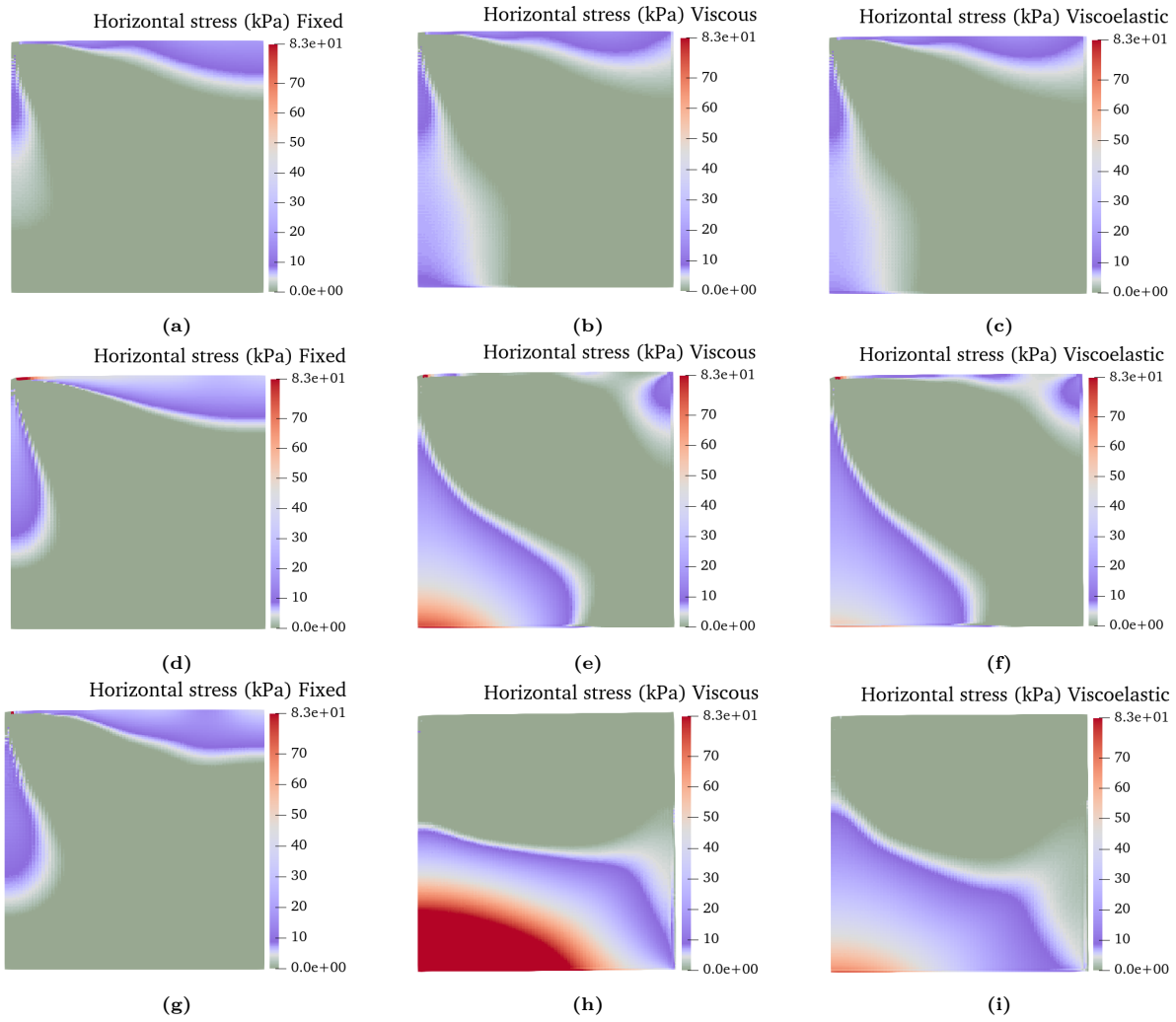

Figure 4.21: Horizontal stress visualisation of the simulation, (a, b, c) t = 0.07s, (c, d, e) t = 0.17s, (g, h, i) t = 0.4s

Figure 4.22 shows displacement visualisations of three models, in order to give a visual views of the simulation with different boundaries. The initial condition is static equilibrium with zero displacement over the domain, as seen in figures 4.22a to 4.22c. After the load is applied, it creates contours of displacement with different values to each model. The load transfers energy into two types of waves, body waves that penetrate into the soil and surface waves that travel near the surface. As can be seen in figure 4.22d, the energy is converted more into body waves than surface waves as the displacement contour tends to grow deeper rather than wider. The figure also illustrates two regions, separated by the cone like trough area. One region with deeper contour is due to the propagation of body waves, while the other is respected to the propagation of surface waves. At time $t = 0.15s$, displacement obtained the highest values with the viscous model and the least with the fixed boundary. This agrees well with the theory as the viscoelastic formulation simulates the spring recovery from the far field, leading to that less displacement can be observed than the viscous model. At time $t = 0.25s$, the input loading reaches its peak value, corresponding to the maximum displacement obtained with the viscous model as $u_{peak} \approx 0.13m$, while this value is approximately 0.09m with the fixed model and nearly 0.11m with the viscoelastic boundary, as seen with figures 4.22g to 4.22i. In figures 4.22j to 4.22l, one can see the evolution of displacement at time $t = 0.4s$.

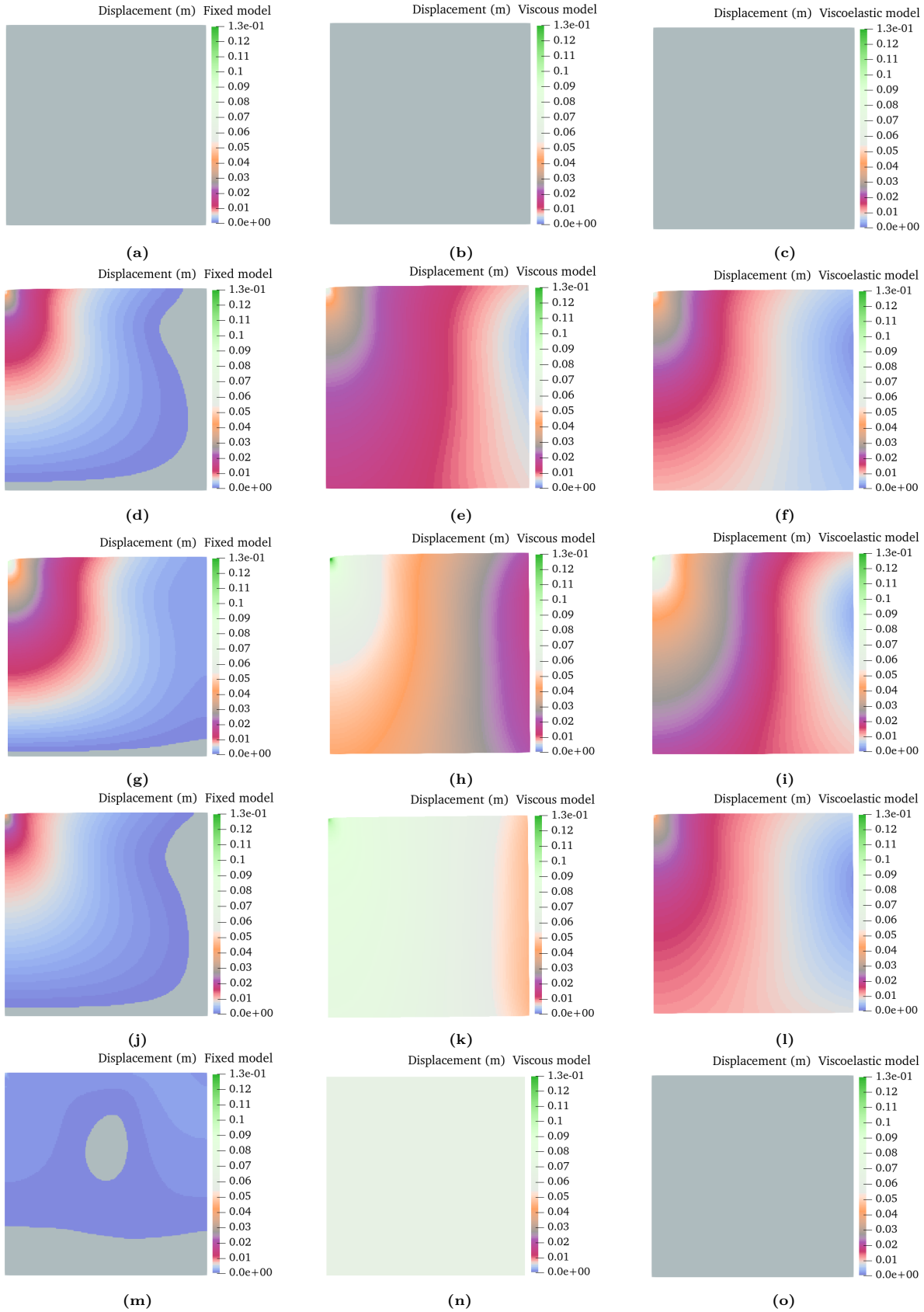

Figure 4.22: Displacement visualisation of all tested model, (a, b, c) Initial condition, (c, d, e) t = 0.15s, (g, h, i) t = 0.25s, (j, k, l) t = 0.4s, (m, n, o) t = 1.0s

While the fixed model shows the reflection of displacement and no movement at the boundary, as the contour shades shrink towards the excitation location, the viscous model keeps moving down. Although it is hard to see, but the bottom boundaries of the viscous and viscoelastic model are moved, as they are no longer staying horizontally as compared to the fixed boundary, but tend to oblique downward the left hand side edges, as shown in figures 4.22h and 4.22k and figures 4.22i and 4.22l. This phenomenon is recognized by looking at the displacement contour in these figures. The left hand side displacement contours hold larger magnitude than the right hand side ones.

However, after loading, these boundaries are proven to have their directions rotated back horizontally, as shown in figure 4.22n and figure 4.22o. While the viscoelastic model returns to its original position with no displacement, the viscous model results in permanent displacement over the domain of $0.06m$, as shown with light, bright displacement shading in figure 4.22n. The fixed model, at this time, has infinite oscillations of displacement even after the loading phase, shown by figure 4.22m. This is trivial as the fixed boundary cannot transmit the input signal properly. The maximum displacement oscillated is about 0.01m which is small.

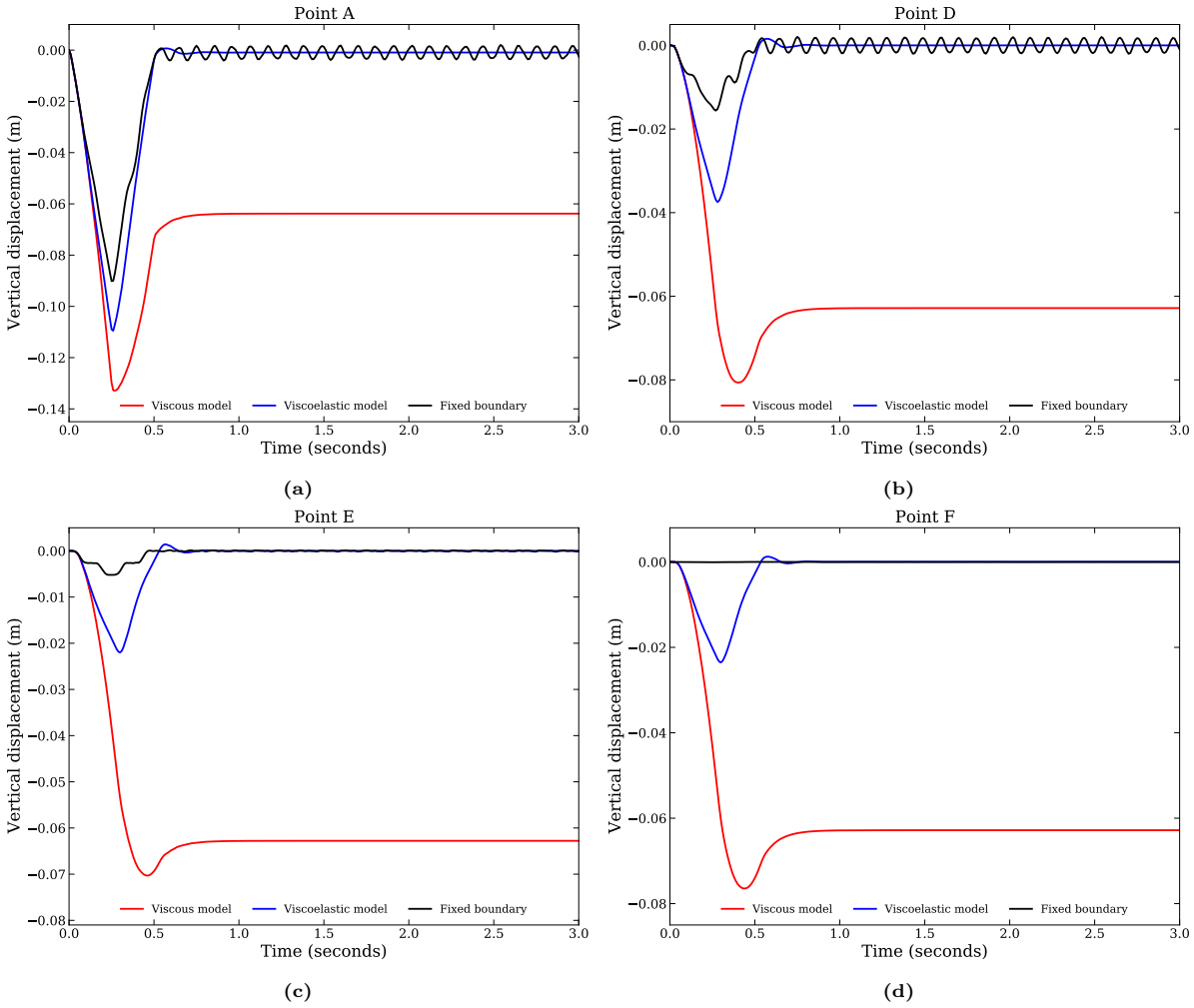

Figure 4.23: Displacement histories of different measuring points

Figure 4.23 shows the vertical displacement obtained at point A, D, E and F. The highest value of displacement is recorded with the viscous model at all points. The fixed model has the peak value of displacement at point A is about -0.09m. The displacement history has a Delta-like shape, while displacement oscillation is obtained at both point A and D (figures 4.23a and 4.23b) with a magnitude of 0.005m, and significantly small oscillations shown in figure 4.23c. The reflection of waves in this case is smaller compared to the 1D case, since with the 2D model with a point load applied, the input energy has to be transferred to the whole domain, therefore the magnitudes of oscillations are strongly

decreased. Besides, the displacement is smoother when absorbing boundaries are used. However, permanent displacement about approximately -0.065m is obtained with the viscous boundary, while the viscoelastic model shows a rebound effect, in which the domain is recovered gradually. Therefore, the displacement records obtained with the viscoelastic model show similar Delta function shapes like the input load function.

The surface waves also cause vertical displacements at points B and C as shown in figures 4.24a and 4.24b. Since point B is closer to the excitation than point C, vertical movement obtained at point B is larger than at point C. An interesting thing is that the oscillations of displacement are recorded to be higher at the boundary (point C). A possible reason to this is that the oscillations occurring at the location of point C are a combination of both surface and body waves reflection, while the inaccuracies in stress at point B as discussed above lead to small oscillations which can be neglected.

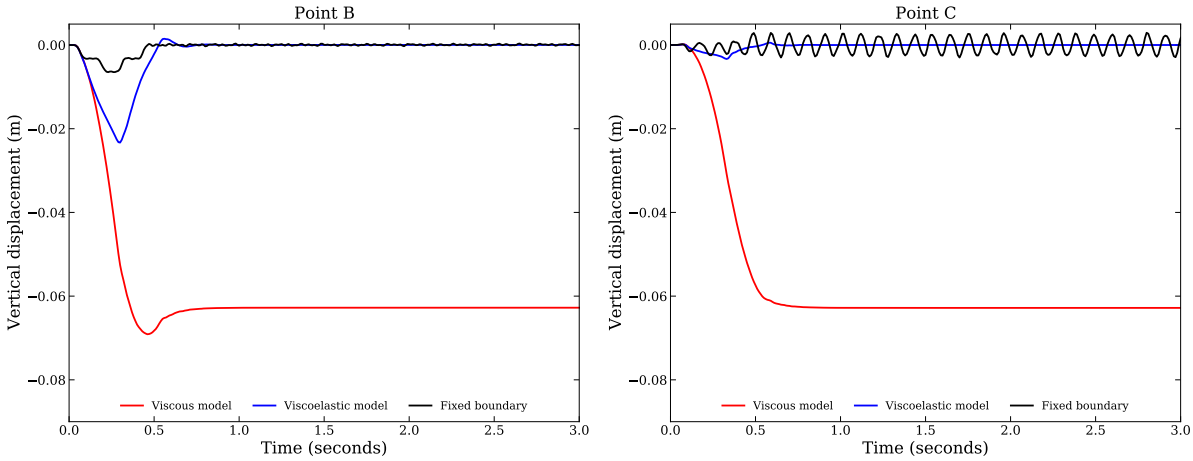

Figure 4.24: Displacement histories of measuring points at the surface

Horizontal displacements at point B, C and E are shown in figure 4.25. It is clear that the spurious reflection as a result of using the fixed boundary leads to the infinite vibrations inside the model. One surprising thing is that the soil particle at point B is closer to the excitation location than at point C, but the horizontal displacement is recorded to be larger at point C than at point B. The horizontal displacement at point C is approximately $0.005m$ higher than at point B when the viscous boundary is used, while this value is nearly $0.00025m$ with the viscoelastic boundary. This shows that the viscoelastic boundary displayed better result than the viscous one. An answer for this phenomenon is that since the left hand side boundary is subjected to the roller condition, the soil particle at the right hand side edge tends to displace towards the excitation source more. Since the right hand side boundary is not fixed, this phenomenon is similar to the shrinkage of the domain towards the left hand side boundary. Finally, while the soil at the surface tends to displace towards the excitation source's location, as shown in figures 4.25a and 4.25b, the soil below the surface is moving far away from the excitation location, seen in figure 4.25c with positive sign displacement. This is trivial as the load is applied downward, therefore the soil will be pushed away.

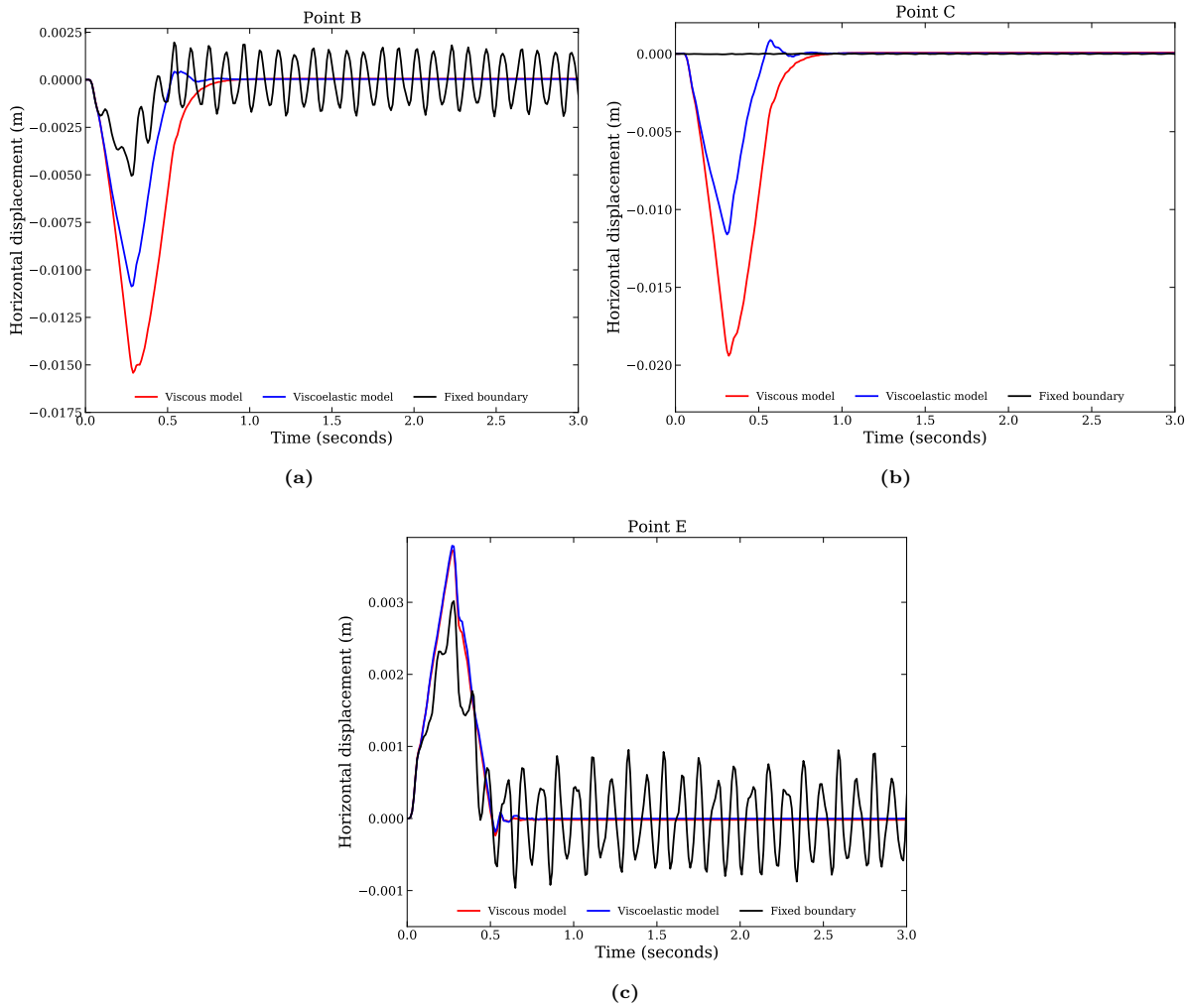

Figure 4.25: Horizontal displacement at the surface and middle of the domain

4.4. Conclusion

MPM is a method which is able to deal with large-deformation problems. However, the radiation condition at the boundary requires special treatments in order to represent accurate wave propagation processes. The common boundary solution (i.e. fixed boundary) is observed to deduct the spurious reflection of waves which are trapped inside the domain, leading to inaccurate outputs. In this chapter, two benchmarks have been used to validate four discussed method of implementations dynamic boundary to absorb the reflected waves, and investigate the behaviours of two boundaries: the viscous and the viscoelastic boundary. Using the conventional approach to impose dynamic boundary only at the surface nodes can give good result for a small-deformation problem, while it failed to render good results with large-deformation in which material points often jump from one element to another. It is shown that implementing these boundary conditions using interpolation with GIMP shape functions instead of linear shape functions, together with the DM-GC method, can almost perfectly absorb the reflections of waves with no stress oscillations. Nonetheless, the viscous boundary has displayed to have slightly better absorption of surface waves than the other one. Radiation condition at the boundary is also represented precisely, showing the improvements in which their performances are more reliable compared to the fixed model. However, the viscous condition gives permanent displacement and often the boundary will be moving during simulation. The viscoelastic conditions, on the other hand, show a better performance in which the boundary has its own stiffness that can minimize the movement of particles.

5

Study of a foundation under repeated loading with implicit MPM

5.1. Introduction

Repeated dynamic loads generated from different sources in nature can cause several impacts to foundation. Under dynamic condition, soils tends to behave in critical modes, often reducing the bearing capacity of the foundation. While the estimation for the bearing capacity of the foundation under static load has been studied intensively for many years by means of empirical methods, experimental data, analytical limit analysis or numerical analysis, such as: Meyerhof (1951), Prandtl (1920), and Tezaghi (1925), the dynamic bearing strength cannot be easily addressed. A general approach to estimate the bearing capacity for shallow foundation is by means of an equivalent pseudo-static approach (or reduction of coefficients). The very first studies using this approach is nominated to Meyerhof (1953) and Shinohara et al. (1960). Later, Budhu and Al-Karni (1993) proposed a limit equilibrium formulation associated with pseudo-static approach to estimate the bearing capacity of shallow foundations. Another approach to estimate the bearing capacity is introduced by Richards et al. (1993) and Soubra (1997). These approaches have assumed the failure mechanism in soil attributed to an asymmetrical Prandtl failure surface, similar to the simplified Coulomb failure wedges.

Knappett et al. (2006) concludes that it is still complicated to predict the actual seismic failure mechanism beneath the footing with confidence, making the dynamic bearing capacity difficult to estimate. Moreover, the bearing strength significantly decreased and the failure mechanism tend to be even more complex if the foundation suffers repeated dynamic loading. An example of failure due to the reduction of the bearing capacity of the foundation under dynamic loading has been observed during the Miyagihen-Oki earthquake of magnitude 7.8 (June 12, 1979), northeast Sendai, Japan. During the seismic event, there were bearing-capacity failures of several oil-storage tank foundations attributed to excessive settlements (Tono and Yasuda, 1981). Drabkin et al. (1996) and François et al. (2010) have shown that the repeated load with small magnitude as compared to static load still can lead to significant accumulation of plastic deformation, leading to failures. Experimental tests conducted by Moghaddas et al. (2011) also shows that cyclic loading often results in permanent plastic settlements.

In an attempt to depict a realistic foundation failure simulation and for helping to study the behind failure mechanism, a shallow foundation under dynamic repeated load is simulated using the advanced technique DM-GC. Dynamic boundary conditions will be imposed with the procedure showed in section 3.3.2, which has been proven to be the most effective.

5.2. Problem Description

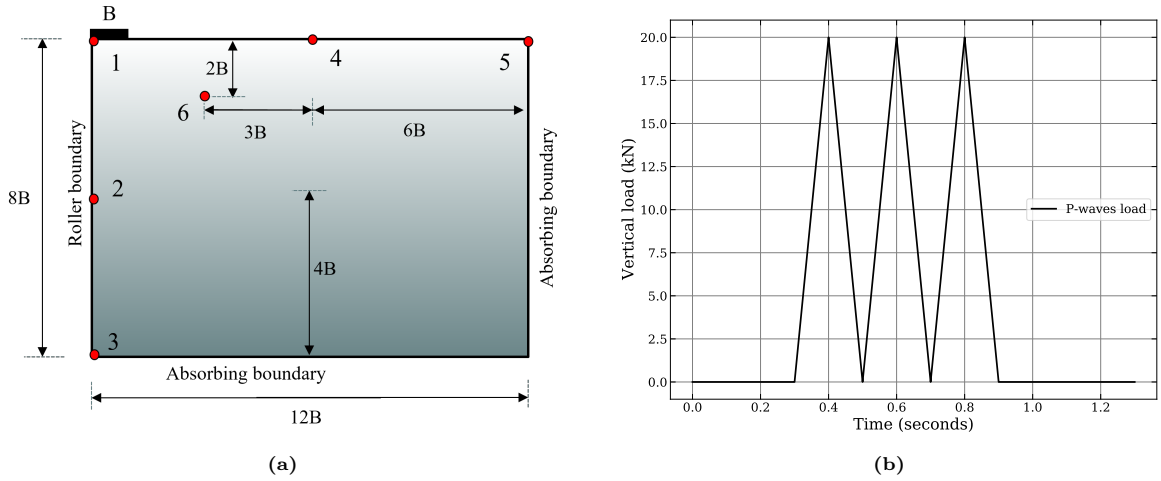

Figure 5.1: Description of the problem, a) Geometry of the model, c) Repeated load

A strip foundation of width $B = 0.5m$ on a cohesive soil suffering repeated dynamic load is modelled in two dimensions. The soil body is modelled to a depth of $H = 4m$ with the width $D = 6m$ The rollers condition is applied along the left hand side boundary to prevent any horizontal movement, while the absorbing boundary conditions are prescribed for the right hand side and bottom boundary. The problem was simulated using a time step of $\Delta t = 0.005s$. The background mesh element size is $\Delta x = \Delta y = 0.0625m$. Each element initially consists of four material points inserted equally distributed at the centre of element's quadrants. Six measuring points are located to record the stress history, as shown in figure 4.9a.

Soil parameters are Young's modulus $E = 200c_u$, soil's density $\rho = 1000kg/m^3$ and Poisson'ratio $\nu = 0.41$. The soil constitutive model used is elastic perfectly plastic soil with von Mises yield criterion incorporated with the post-peak softening, as shown in figure 5.2:

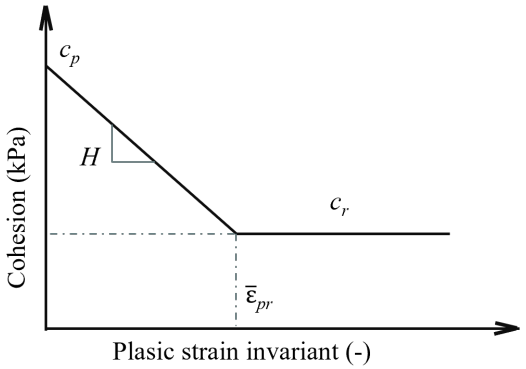

Figure 5.2: Post-peak softening model, after Wang and Hicks (2016)

The peak cohesion is $c_p = 10kPa$, the residual strength is $c_r = 3kPa$. The softening modulus is $H = dc/d\bar{\varepsilon}_p = -140kPa$ where $\bar{\varepsilon}_p$ is the plastic strain invariant.

The quasi-static scheme is first used to generate the initial stress condition of the domain, with the gravitational force applied incrementally for 50 steps until $t = 0.25$s then kept constant at $1g$ until the end of the initial stage (60 time steps). The dynamic stage is then carried out at time $t = 0.3$s. As shown in figure 5.1b, the dynamic load applied at time $t = 0.3s$ consists of 3 repeated pulses. Each pulse has a duration of 0.2s. First, results with basic MPM using fixed boundary conditions will be used as the starting point. Then results of three models: (1) DM-GC model with fixed boundary, (2)

Viscous model and (3) Viscoelastic model, will be presented to emphasize any improvements comparing to conventional MPM. As discussed before in Chapter 4, the method 4 of imposing dynamic boundary conditions renders results with highest-quality, therefore only this method will be used to apply the viscous and the viscoeslatic boundary.

5.3. Result

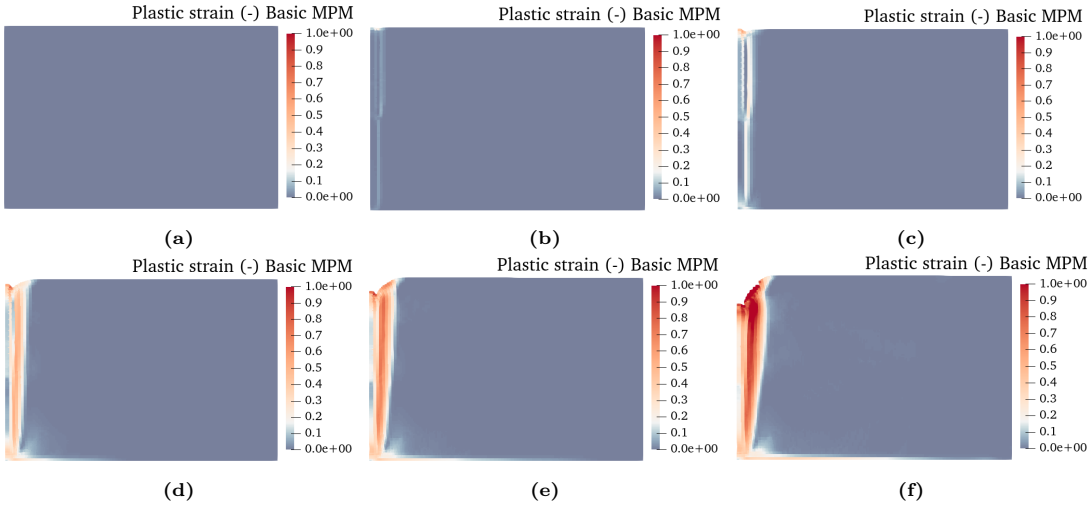

Figure 5.3: Plastic strain evolution of fixed boundary with basic MPM, (a) After static analysis phase (t=0.3s), (b) t = 0.31s, (c) t = 0.32s, (d) t = 0.36s, (e) t = 0.4s and, (f) t = 0.45s

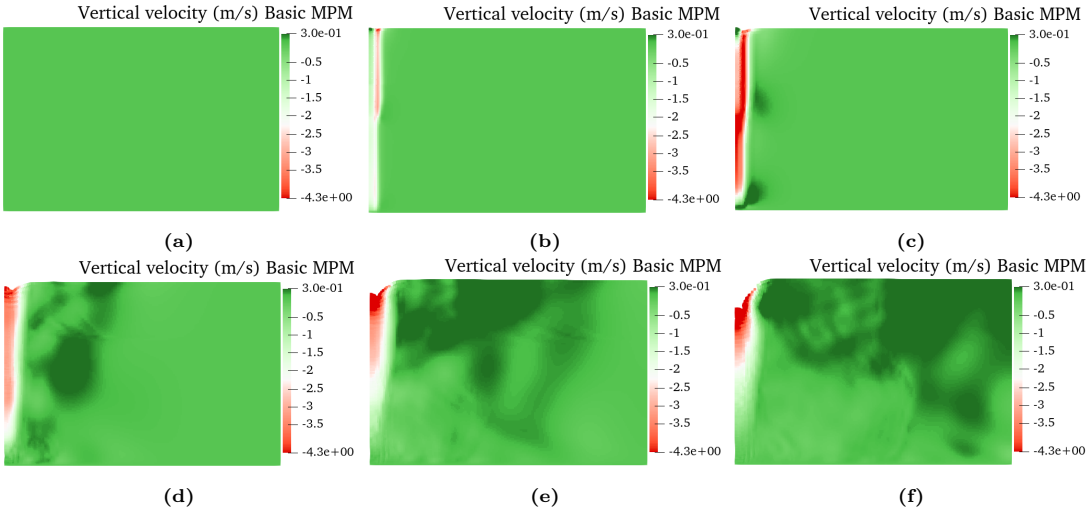

Figure 5.4: Vertical velocity record of fixed model with basic MPM, (a) After static analysis phase (t=0.3s), (b) t = 0.31s, (c) t = 0.32s, (d) t = 0.36s, (e) t = 0.4s and, (f) t = 0.45s

Figure 5.3 shows visualisation of the evolution of plastic strain inside the domain of the fixed model using basic MPM. The maximum of plastic strain is fixed to 1.0 for better visualisation. Overall, the results are genuinely poor. At time $t = 0.3s$ there is no plastic strain as the calculation of initial stresses has just finished. After that, at time $t = 0.31s$ after the load is applied, plastic strain started to be generated from beneath the foundation all the way down to the bottom boundary (figure 5.3b). As the simulation keeps going, more plastic strain is generated around this region (figures 5.3c to 5.3e), forming the shear band, starting at the surface point with nearly $3B$ distance away from the foundation toe, goes down to the bottom boundary, as seen in figure 5.3f. At time $t = 0.45s$, the failure zone is completely formed, and the simulation stops as failure occurs at the surface near the foundation toe.

This result is unrealistic as the shear band is forming significantly fast, just 0.01 second after the load is applied. Moreover, the failure surface goes relatively deep to the ground.

This phenomenon can also be observed in figure 5.4. It is clear that no contours of velocity can be observed, which indicates that the propagation cannot be simulated properly. Besides, at time $t = 0.32s$ (figure 5.4c) there is a dark-green coloured region of positive velocity, appeared at the bottom below the foundation. This means the wave reached the bottom and started reflecting to the surface, indicated by dark-green color. As can be seen in figures 5.4e and 5.4f, particles near the surface often have upward movement, as the surface is free, therefore it is easy to soil particles near the surface to move.

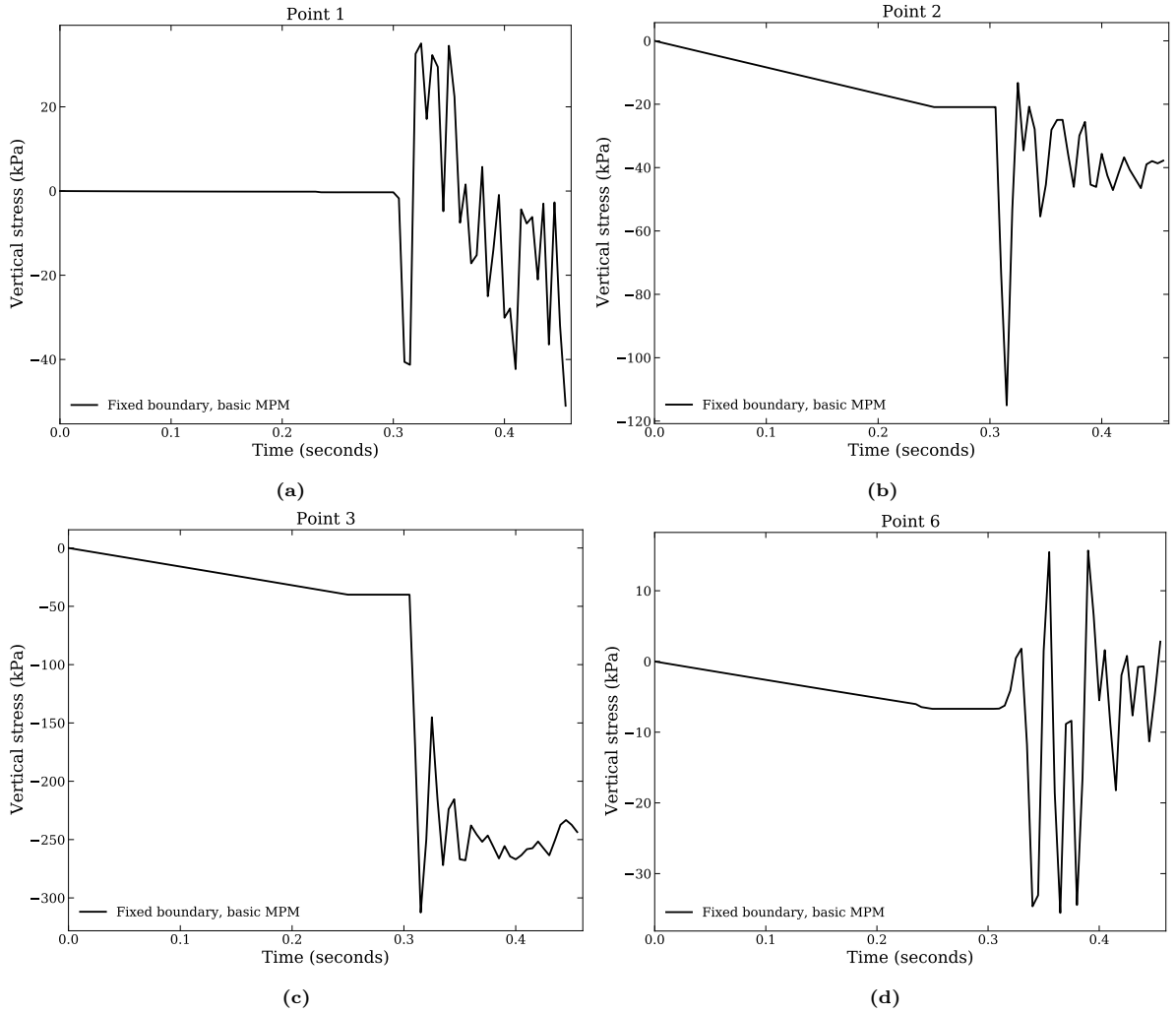

Figure 5.5: Vertical stress histories of measuring points 1, 2, 3 and 6

The vertical stress histories of different measuring points are shown in figure 5.5. The results are relatively poor. The stress at all measuring points jumped instantly after loading, with large stress oscillations. This agrees well with what has been discussed in Chapter 4 which shows that basic MPM often results in instant jumps of stress right after the load is applied, therefore plastic strain will be generated instantly after loading. The input vertical stress is about $40kPa$, which is shown to be significantly smaller than the maximum values of stress at point 2 and 3. Finally, the simulation is relatively unstable and it is terminated at time $t = 0.45s$. Summarising, basic MPM with fixed boundary conditions give poor results and it is unable to capture complex behaviours of the problem.

Next, simulations of the viscous and the viscoelastic boundary model implied using method 4 will be presented, together with outputs of the fixed model using DM-GC technique. For simplicity, *the fixed boundary with DM-GC* notation will be denoted in figures as *Fixed boundary* from now on.

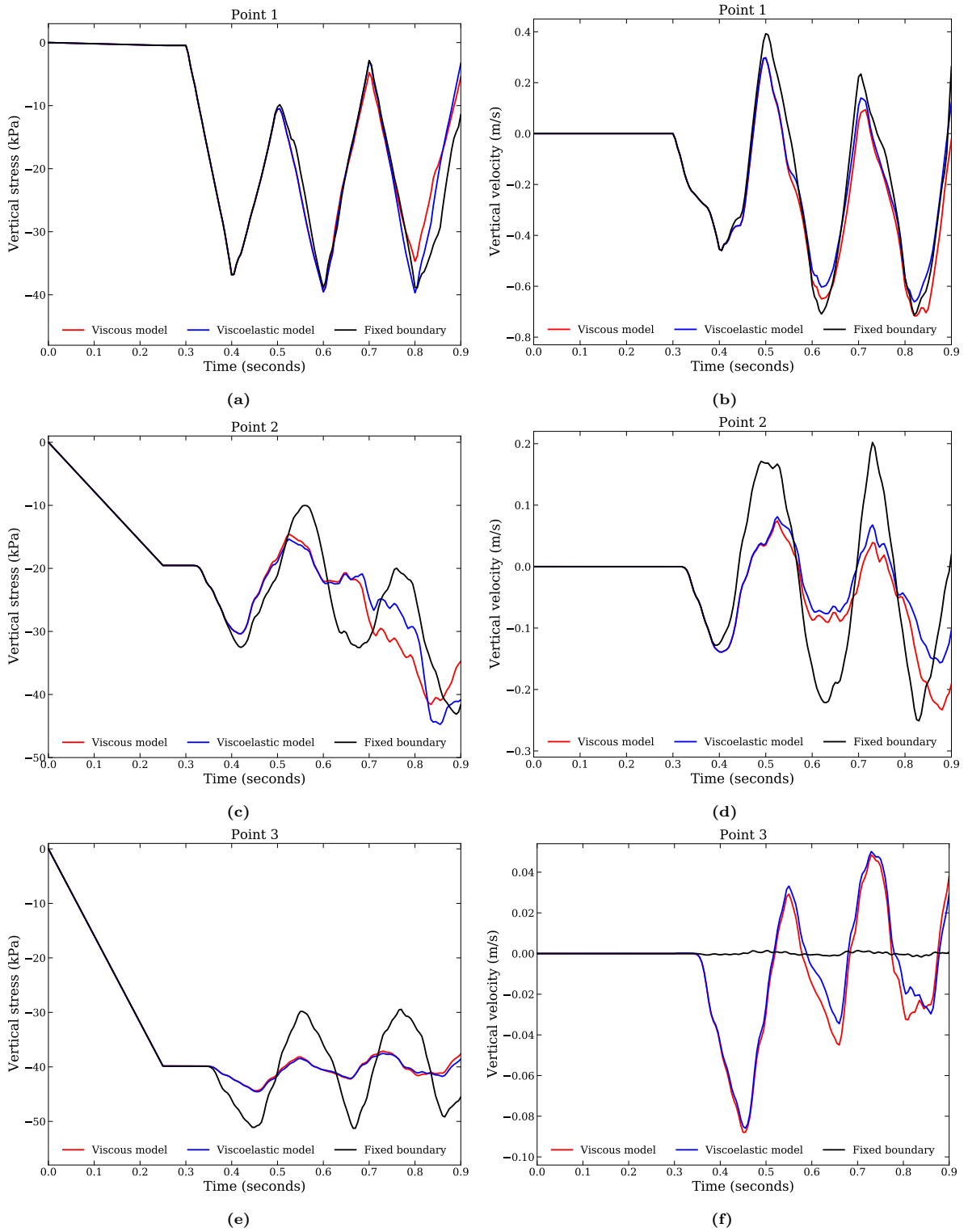

Figure 5.6: Vertical stress and velocity histories of point 1, 2 and 3, (a, b) stress and velocity at point 1, (c, d) records at point 2, and (e, f) records at the boundary

First, the stress, velocity records beneath the foundation are shown in figure 5.6. As can be seen, during the quasi-static stage, the initial stress is gradually increased from t = 0.0s until the gravitational acceleration fully reached $1g$ at t = 0.25s. During the initial stage (t < 0.3s), zero velocity condition is kept. Maximum vertical stress at the bottom of the soil domain is $40kPa$ (figure 5.6e), which is what to be expected. Overall, results of all three models have greatly improved than what has been shown with

basic MPM. The stress curves are smoother, and no significant stress oscillation is observed, simulation time lasts longer with complex behaviours inside the domain being captured.

At time t = 0.3s, the repeated load is applied. Then at t ≈ 0.34s, the load propagates to the location of point 2, resulting in increases of vertical stress and velocity as shown in figures 5.6c and 5.6d. The load keeps propagating and then reaches the bottom boundary at time t ≈ 0.38s. At the point right beneath the foundation (i.e. point 1), the stress and velocity history is recorded with only minor differences regading the peak. The differences are due to the reflection of waves, but as discussed in chapter 4, the reflection at the free surface will not result in any major inaccuracy. Nevertheless, the peak value of the first pulse is approximately 40kPa, which is what to be expected.

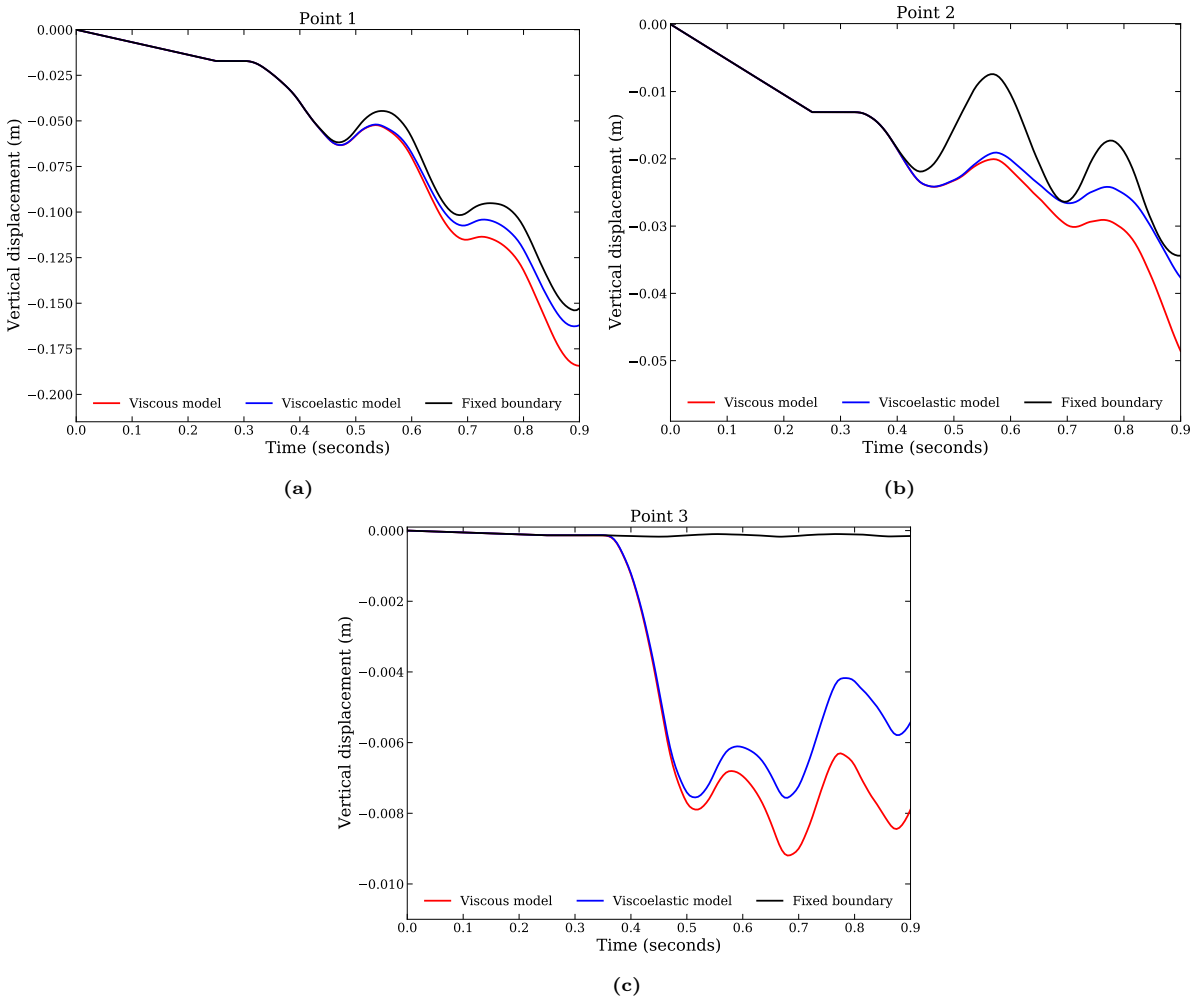

Figure 5.7: Vertical displacement at point 1, 2 and 3

The fixed boundary, again causes the spurious reflection even with the use of DM-GC technique. Moreover, it is easy to analyse the result incorrectly. In figure 5.6c it seems like the fixed boundary has the best result as it displays all 3 pulses of stress clearly. However, this is actually inaccurate, as looking at the peak time. In figure 5.6c, the first pulse arises at time t = 0.34s, then it peaks at time t = 0.42s and finally the trough is observed at time t = 0.58s. This means the first pulse has a duration of 0.24s, which is inaccurate as compared with the input load shown in figure 5.1b. The explanation for this phenomenon should be similar to what has been observed in figure 4.3, where the incoming signal meets the reflected waves, resulting in partly amplification or decrease of the magnitude of the stress waves. As can be seen in figure 5.6c, the first pulse vanishes at time t = 0.54s as obtained with the viscous and viscoelastic model. The stress records of all three boundaries at point 2 are identical until time t = 0.38s, then the fixed model starts to shows inaccuracies in stresses. This is because at that time, the reflected waves from the bottom boundary meets the incoming stress waves propagated

from the foundation. Similar phenomenon can be also seen in figures 5.6d and 5.6e, where the peak and trough velocity and stress obtained from the fixed boundary is clearly two times larger than what has seen with the viscous and viscoelastic boundary. This is similar to what has been explained with figure 4.12d.

The equivalent peak dynamic stress applied at the top is $P_{peak} = 40kPa$, with given soil properties, the compressional wave velocity of the soil is $C_p = 68.2m/s$, this results in the maximum velocity of the soil particle should be:

$$v^p \approx \frac{P_{peak}}{\rho \times C_p} = \frac{40kPa}{1000kg/m^3 \times 68.2m/s} \approx 0.58m/s \tag{5.1}$$

The peak velocity of the first pulse obtained at point 1 is $v = 0.52m/s$. This value has some deviation to the analytical solution of $v^p = 0.58m/s$. This can be attributed to the fact that the load is transferred to the soil with instant attenuation and decreases in the magnitude since parts of the load are converted into surface waves. This agrees to what is seen in at figure 5.6a, where the first pulse has the peak value of approximately $38kPa$, smaller than $40kPa$.

With the load is repeated, the vertical stress and velocity at point 1 increase with each pulse. Maximum vertical stress reached is nearly $40kPa$ right beneath the foundation, which is smaller than the Prandtl's solution obtained from the plasticity theory for the bearing capacity, i.e., $(2 + \pi)c_u \approx 51.4kPa$.

The vertical displacements at point 1, 2 and 3 are displayed in figure 5.7. The displacement of the foundation is predicted similarly for both three models. All three models have shown the accumulation of displacements after each pulse. However, the displacement at point 2 is shown to be calculated more accurately with the dynamic boundaries rather than the fixed condition. Because of the reflection coming from the bottom, the fixed model displaces less, as compared to others. This can be observed since the displacement histories of all three models are identical until time t ≈ 0.4s for point 2 and t ≈ 0.44s for point 1, in which the fixed model starts to displace less. Since the wave is reflected from the bottom, the event occurs at point 1 later than at point 2. An interesting thing is that at the bottom, the displacement shown by the viscous and viscoelastic boundary are having an increasing trend, until the second peak pulse is reached, then the boundary starts to moving upward. The reason for this should be that at this time, potential shear bands occur, and the soil beneath the foundation is pushed to the side, therefore the bottom boundary shows recovered movements.

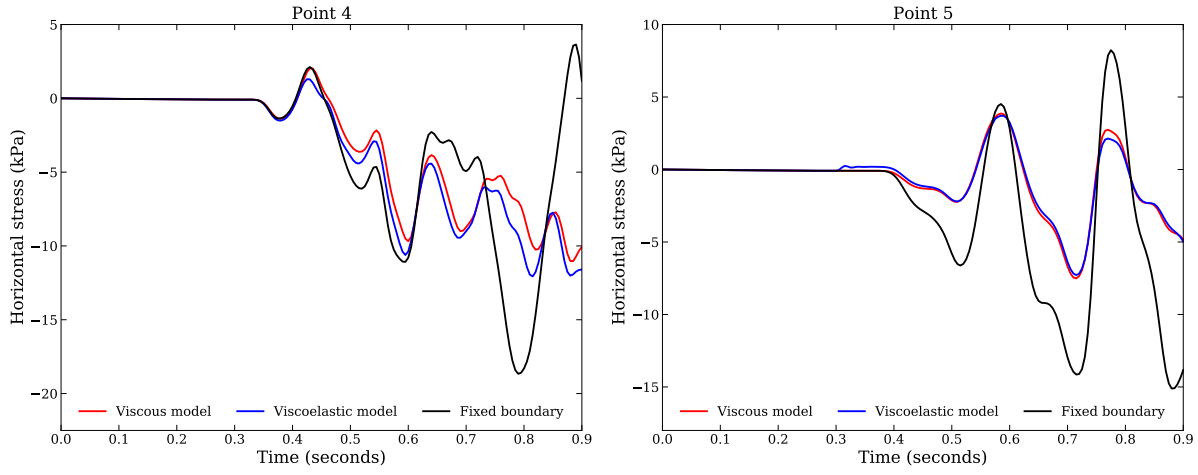

Figure 5.8: Horizontal stress histories of measuring points at the surface

The horizontal stress and displacement records are shown in figures 5.8 and 5.9. The results look relatively disorganized because the fact that the soil at the surface which is adjacent to the foundation toe is often pushed upward, leading to the oscillations during propagation of waves. As can be seen in figures 5.8a and 5.9a, the dynamic loading results in pushing soil outwards from the foundation. Both

the stress and displacement are accumulated for each pulse. The displacement and stress records of the fix boundary is identical to the dynamic boundaries until time t ≈ 0.43s when the incoming wave reacts with the reflected waves at the boundary. At the boundary (i.e. point 5), the amplification of stress is well-observed, as shown in figure 5.8b, in which the peak stress obtained with the fixed model are nearly twice as large compared to absorbing models.

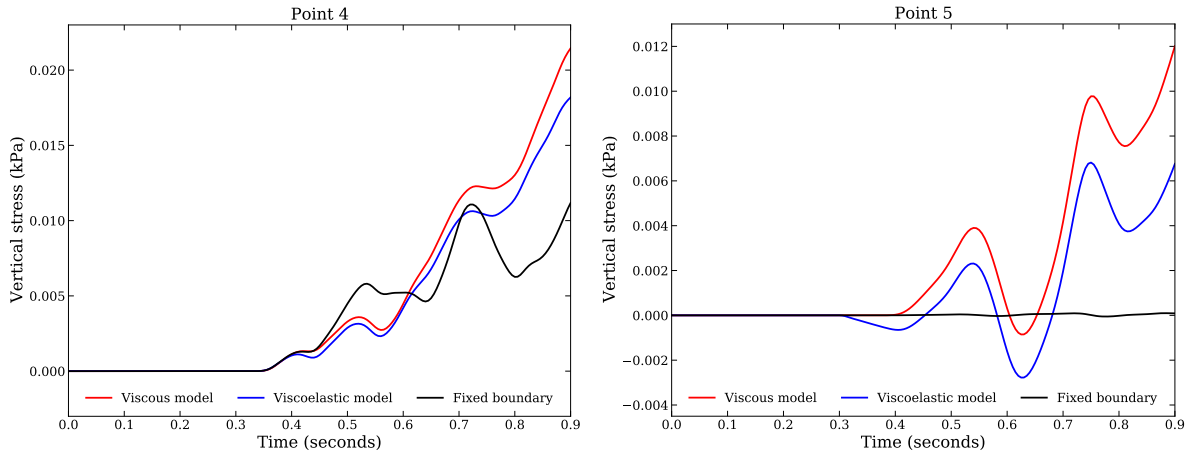

(a) **(b)**

Figure 5.9: Horizontal displacement histories of measuring points at the surface

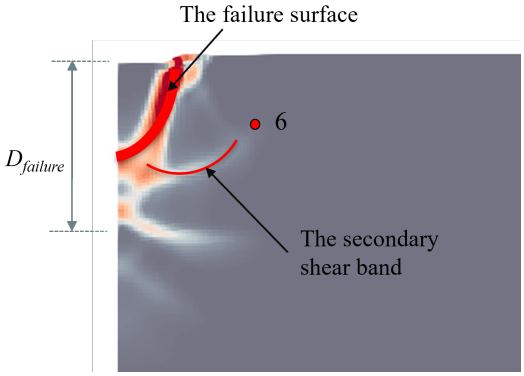

Figure 5.10: Illustration of the failure surface and secondary surface with the fixed model at $t = 0.6s$, with $D_{failure}$ is the maximum depth where the failure surface can reach

Next visualisations of the plastic strain evolution during the simulation are shown in figure 5.11. After the initial stage (i.e t = 0.3s), all models display no plastic strain. Then at time t = 0.415s, after the first pulse reaches its peak, plastic strain is developed beneath the foundation with a maximum value of $\varepsilon^p = 0.05$. More plastic strain is then developed at t = 0.6s, concentrated in a wedge shape, starting at the toe of the foundation near the surface to the maximum depth of approximately 2B beneath the foundation, as shown in figures 5.11g to 5.11i. Up until this time, all three models behave almost identically. At time t = 0.7s which the second loading pulse is applied completely, the first shear band is completely formed. Although all three models have shown the plastic region around the foundation's toe with similar shape, the maximum depth in which the failure surface is formed by the fixed model ($D_{failure} \approx 3.5B$), appears to be shallower than what is seen with the absorbing models ($D_{failure} \approx 4.5B$). At the same time, the fixed model shows a secondary shear band which is developing upwards to the surface at the depth of approximately 2.5B, while with the absorbing models, this shear band has just formed. Finally, at the end of simulation the secondary shear band is completely formed ups to the surface with the fixed model (figure 5.11m), while with the dynamic boundaries, this wedge is not developed fully towards the surface (figures 5.11n and 5.11o). Note that the foundation reaches the failure point in which the soil at the foundation's toe is completely demolished.

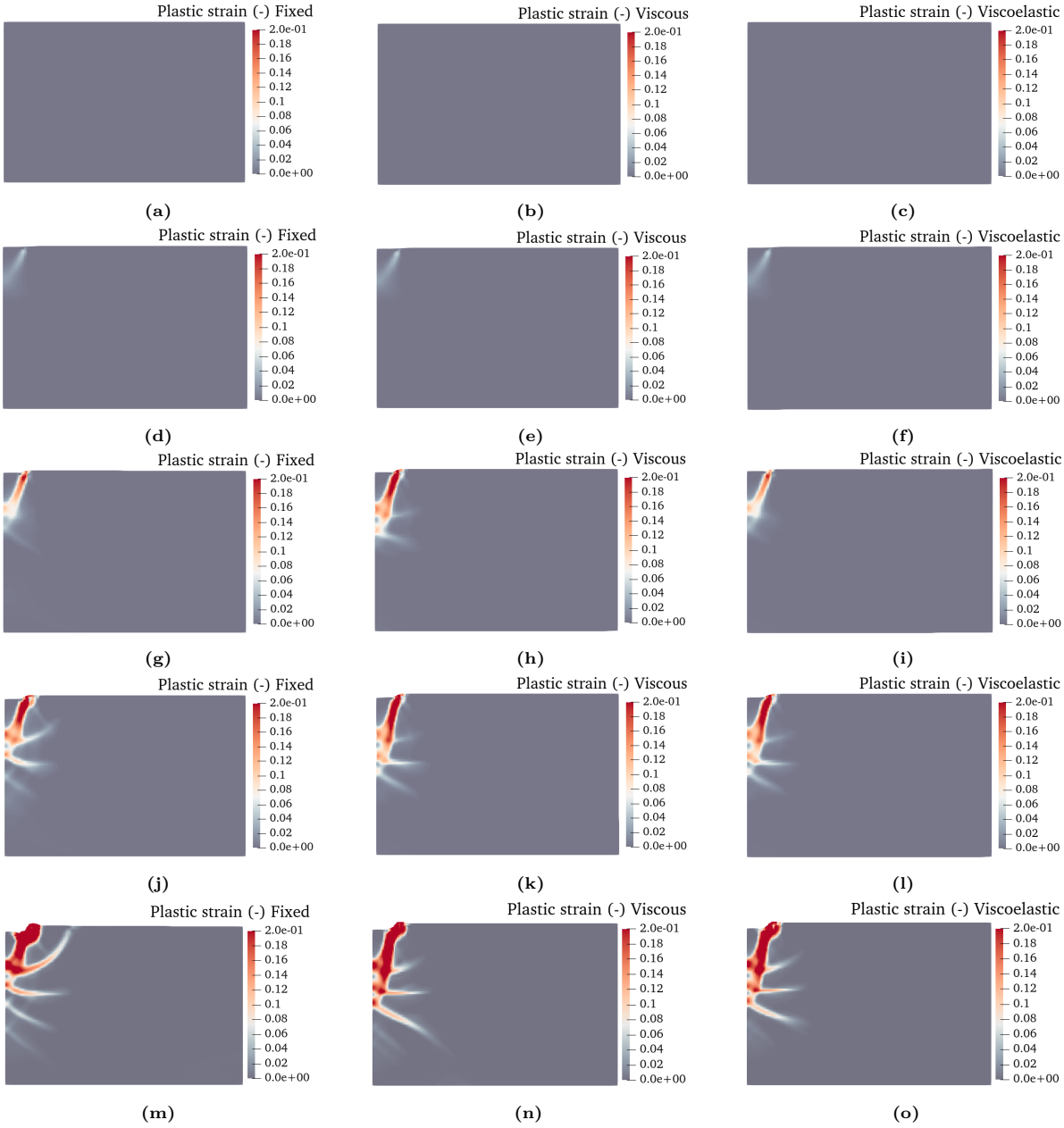

Figure 5.11: Plastic strain evolution of all three models, (a, b, c) After static analysis phase (t=0.3s), (c, d, e) t = 0.415s, (g, h, i) t = 0.6s, (j, k, l) t = 0.7s, (m, n, o) t = 0.9s

Figure 5.12 shows the evolution of deviatoric stress inside the boundary domain. Comparing to figure 5.11, the development of devatoric stress can represent the failure surface correctly. As can be seen in figures 5.12g to 5.12i, the contour with maximum magnitude of deviatoric stress ($\sigma^{peak} \approx 17kPa$)covering around the region where the secondary shear band is formed. This is correct, since the von Mises yield criterion states that: $\sigma_{dev}^{peak} < \sqrt{3}c_u \approx 17.1kPa$ with $c_u = 10kPa$ as given above, plastic strain will developed at any point that has the deviatoric stress equal or larger than: σ_{dev}^{peak}. It is interesting to note that the failure zone (red zone with maximum plastic strain as shown in figures 5.11m to 5.11o) now is characterised with light blue color region(or $\sigma_{dev} \approx 5kPa$ and surrounded by the maximum deviatoric stress contour. This is because after the soil in a region is completely sheared, the undrained strength is reduced from the peak cohesion of $c_u = 10kPa$ to the residual cohesion of $c_u = 3kPa$, leading to the yield deviatoric stress in this region be reduced to: $\sigma_{dev}^{peak} \approx 5.2kPa$.

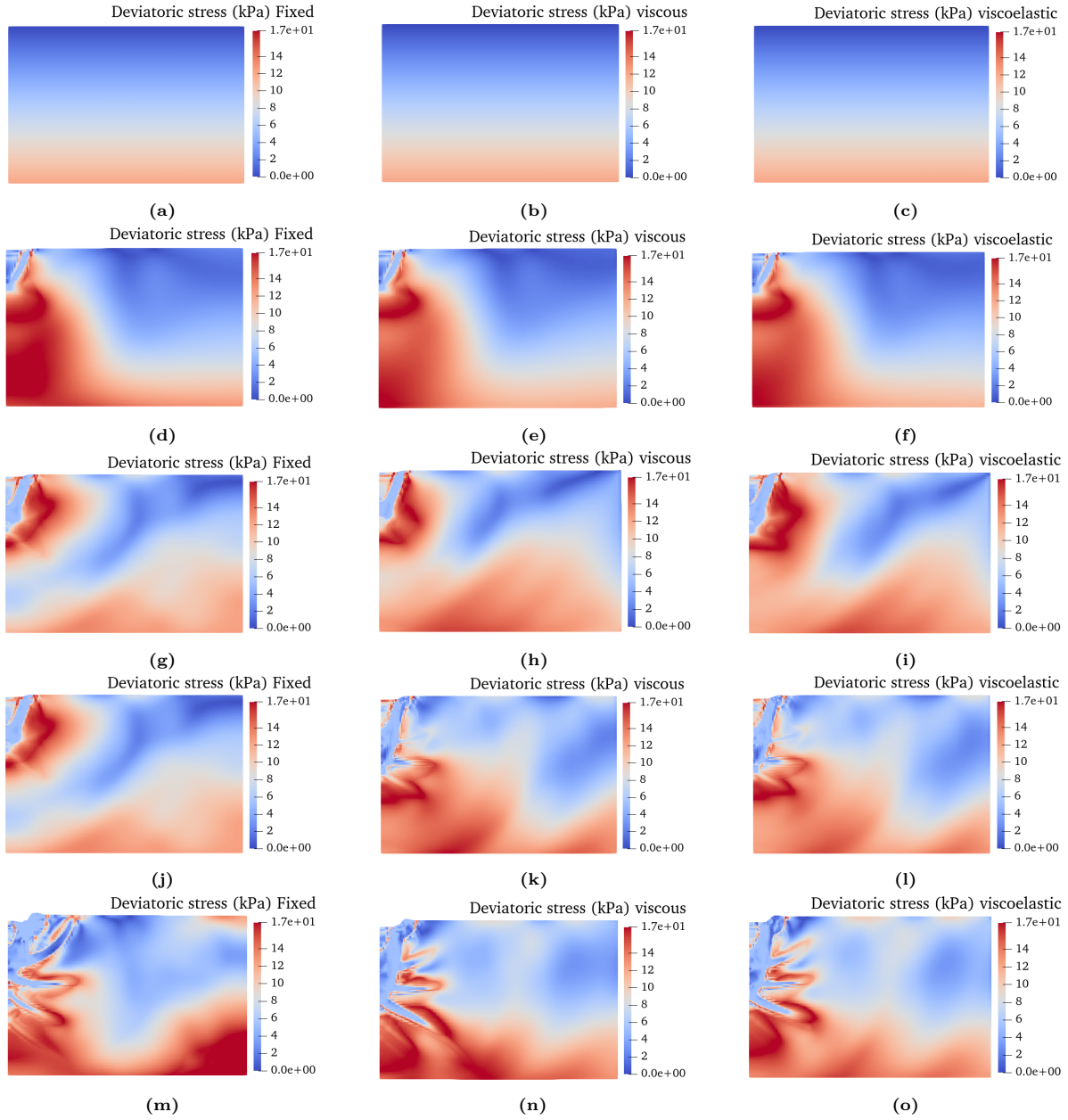

Figure 5.12: Deviatoric stress evolution of all three models, (a, b, c) After static analysis phase (t=0.3s), (c, d, e) t = 0.415s, (g, h, i) t = 0.6s, (j, k, l) t = 0.7s, (m, n, o) t = 0.9s

The secondary shear band (wedge) which is shown in figure 5.12m, however, is not realistic and it is the result of the spurious reflection. In other words, because the waves are trapped inside the model (including the surface waves as discussed above with figure 5.8), interactions between the incoming signal and the reflected waves can lead to the amplification of stress, causing the shear band to occur easier. Figure 5.13 shows how the process happens. The maximum and minimum horizontal stress are adjusted for better visualisation. At time $t = 0.73s$ (figures 5.13a to 5.13c), the horizontal stress is propagating towards the right hand side edge. This wave reaches the boundary at $t = 0.8s$ as shown in figures 5.13d to 5.13f. Right here the interaction between incoming waves and reflected waves results in the amplification of the horizontal stress at the fixed boundary (figure 5.13d), while the maximum horizontal stress at the boundary with absorbing models is nearly two times smaller. Finally, the reflected waves propagates to near the foundation and creates the secondary shear band (figure 5.13g) while the input horizontal stress is absorbed at the boundary as shown in figures 5.13h and 5.13i. This means the secondary shear band which has a wedge-shape is exactly a product of numerical artifacts.

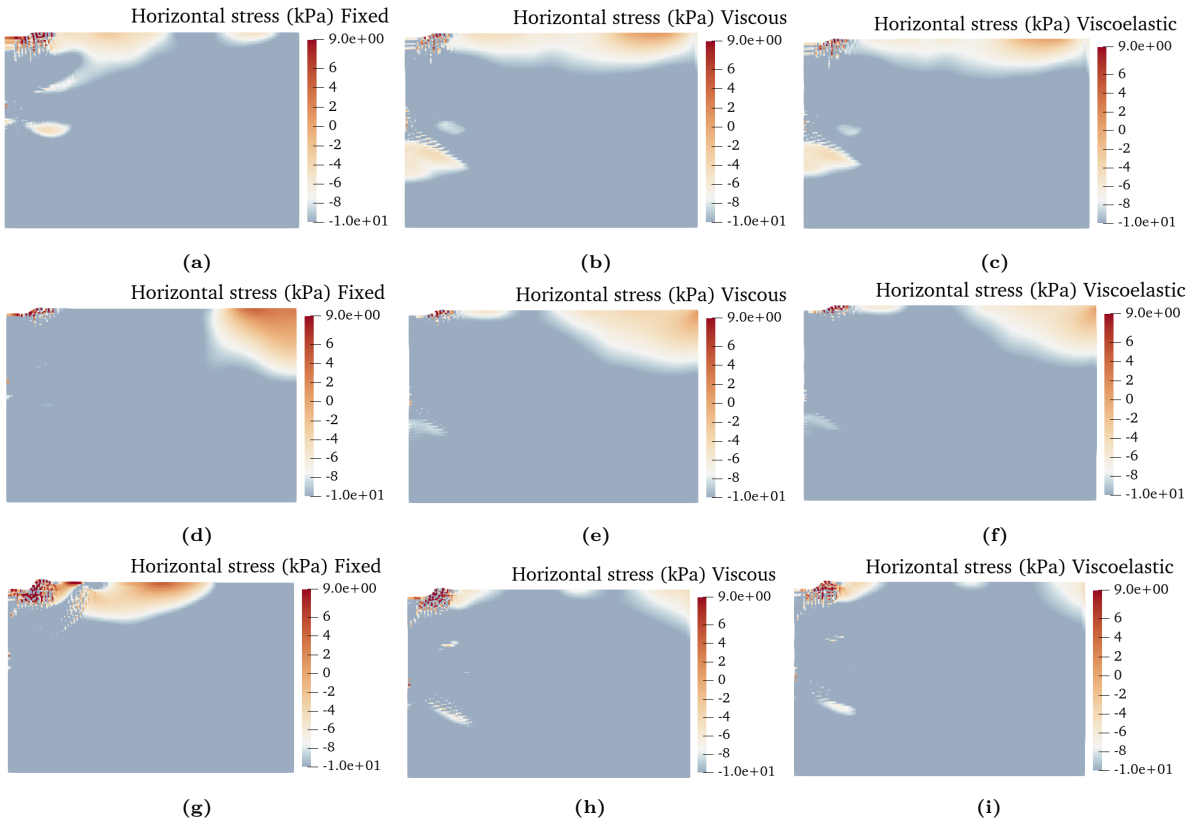

Figure 5.13: Horizontal stress propagation inside the domain, (a, b, c) At t=0.73s, (c, d, e) At t = 0.8s, (g, h, i) t = 0.88s

The deviatoric stress recorded at point 6 which is located at the middle of the secondary shear band as shown in figure 5.10, is displayed in figure 5.14. As can be seen clearly, the stress history is identical until time $t \approx 0.44s$, then the incoming stress becomes amplified and then it reaches the maximum deviatoric stress of $\approx 17.1kPa$ at time $t = 0.66s$ with the fixed boundary, while in fact, the second pulse should peak at time $t = 0.64s$ as shown with the absorbing boundaries. This means that more plastic strain has been generated with the fixed model. Together with figure 5.13, this explains why the secondary shear band can be formed easier with the fixed boundary condition compared to with the dynamic boundary conditions.

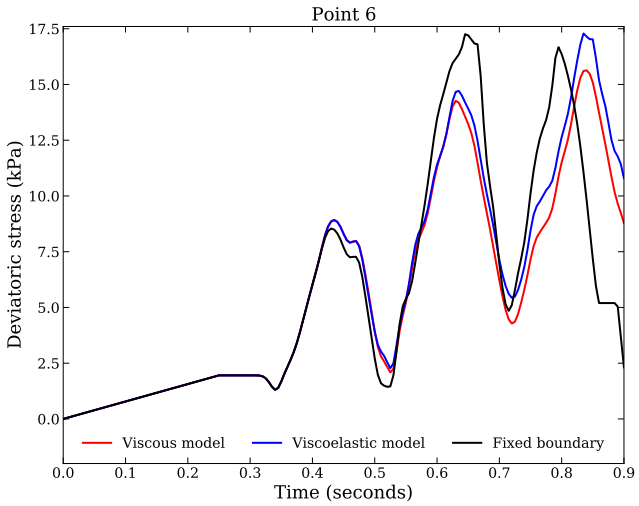

Figure 5.14: Deviatoric stress history at point 6 with different boundary conditions

The failure zones under the foundation that is shown in figures 5.11m to 5.11o and figures 5.12m to 5.12o are similar to the simplified failure surface shown by Budhu and Al-Karni (1993):

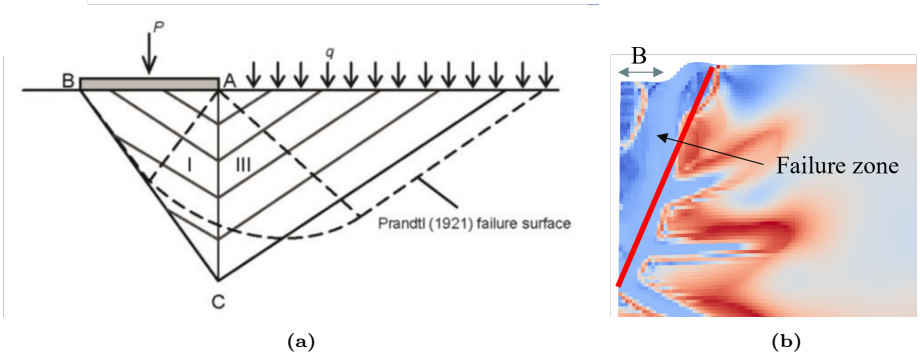

(a) (b)

Figure 5.15: Comparison of failure mechanism, a) Simplified failure zone, adapted from Budhu and Al-Karni (1993), b) Failure zone obtained with the viscoelastic model (extracted from figure 5.12o

As can be seen from figure 5.15, the failure zone obtained from the numerical model shows differences to what has been discussed in Budhu and Al-Karni (1993). The depth in which the failure occurs with the numerical result appears to be deeper than what is seen in the literature. Moreover, the failure region near the surface is also smaller than the simplified solution. While the Prandtl's solution evaluates the stress state is critical based on the Mohr-Coulomb failure criterion $\tau < c_u + \sigma tan\phi$, the von Mises yield criterion adapted in simulation is $\sigma_{dev}^{peak} < \sqrt{3}c_u$. This means the Prandtl's failure tends to develop horizontally, while the von Mises's solution often generates more plastic strain at a deeper depth. Based on the simulation, it can be concluded that the foundation failure is due to the excessive settlement which is mainly attributed to the accumulation of plastic strain. This agrees well with what has been discussed before, as shown in Richards et al., 1993.

5.4. Conclusion

The proposed method in Chapter 3 to combine the DM-CG method with dynamic boundary conditions is used to simulate a geotechnical example of a foundation under repeated dynamic loading. The method was able to capture realistic soil behaviour in the domain, in a combination with the failure mechanism beneath the foundation. It was demonstrated that even with smaller, but repeated, load magnitudes, failures of the foundation can still be triggered attributed to the accumulation of plastic strain. The dynamic boundary conditions are able to represent the radiation condition at the boundary, addressing the numerical artifact that the secondary shear band is developed with the use of the fixed boundary, thus validating the implementation for the study of foundation's stability.

6

Summary

6.1. Research questions

The main research question was formulated as:

"How can dynamic boundary conditions improve the accuracy of the material point method?"

The thesis answered this question by solving the following sub-research questions:

Why is the presence of dynamic boundary conditions necessary?
The MPM is formulated based on the finite element analysis approach, in which the domain of interest is subdivided into a set of finite elements/sub-domains, to approximate the exact solutions. With this approach, the continuity in the real domain is often replaced by a finite - dimensional domain truncated with fixed boundaries. This leads to feasible computations, but at the same time, the spurious reflections are generated because the seismic waves cannot transmit through this boundary, thus reflecting back. In order to improve the stress history calculation, it is needed to apply the absorbing boundary conditions at the domain's surface to represent the radiation conditions.

"Which boundary conditions can be implemented in MPM? How to implement them?"
The literature review about dynamic boundary condition in Chapter 3 has been conducted to review how these boundaries work, as well as giving two promising solutions: the viscous and the viscoelastic boundary. These conditions are widely known solutions to model the unbounded domain's behaviours. The first condition is equal to a set of dashpots attached normally and tangentially to the surface while the latter one is equivalent to a set of Kevin-Voigt elements attached in the normal and tangential direction to the boundary. Implementation of these boundaries to MPM can be done similar to FEM, in which the diagonal terms (corresponding to the surface nodes) of the stiffness matrix and the force vector are directly modified, as shown in section 3.2.

"How to validate these implementations?"
An example of the 1D soil column under dynamic load and a 2D model have been investigated. The ability to transmit the seismic waves through the boundary were shown to be accurate. The stress history becomes clearer when using the dynamic boundaries whereas with the fixed condition, incident waves and loading are trapped inside the domain, causing oscillations of stress, leading to amplification and decreasing in stress magnitudes, as well as proving wrong time records for peak stress values. However the conventional MPM has its own drawback that the physical domain does not coincide with the background edges. Due to this issue, implementation of dynamic boundaries at the surface nodes will give poor stress diagram with large-deformation problem where the load is sufficiently large and cell-crossing events occur.

"What can be done to improve the implementations?"
It is proposed to apply the DM-GC procedure, together with the use of the viscous boundary and the viscoelastic boundary, in order to diminish the consequence of cell-crossing problem. The technique is to determine a pre-defined particles layer, where the boundary condition is converted to traction and is interpolated to corresponding nodes using GIMP shape functions, as shown in section 3.3.2. The technique is then validated by the 1D benchmark with large deformation and a 2D plane strain model

example.

6.2. Conclusion

In order to improve the accuracy of the material point method (MPM), the implementations of dynamic boundary conditions are presented, along with the proposed technique to improve their efficiencies. It was demonstrated that the conventional MPM's accuracy is far from the desired level, particularly in solving dynamic problems involving large deformation. Hence, further improvements are necessary, not only to reduce the well-known numerical inaccuracies (i.e. stress oscillation), but also to extend the available solutions for dynamic analysis.

Focussing on the limitation that MPM with fixed boundary is unable to represent the radiation conditions with dynamic problems, a literature review of existing solutions was carried out. Two promising conditions: the viscous boundary and the viscoelastic boundary, were implemented in MPM framework in: (i) a similar way to what has been used for imposing boundary in the finite element method (FEM), and (ii) a way of having a pre-defined layer of material points, then using DM-CG procedure to interpolate the dynamic conditions.

These implementations have been tested with two benchmarks: a) a 1D soil column under dynamic load, in range of: small deformation with analytical solution and large deformation; and b) a 2D symmetrical plane strain model. These examples verify the improvements of the implementations, particularly in terms of the elimination of numerical reflections of the results. The main achievements and conclusions of the thesis are summarised as follows:

- It was demonstrated with the benchmark that the basic MPM has two main problems in performing dynamic analyses: the first one is the incapability to transmit the input signals smoothly through the boundaries, and the second one is the stress inaccuracies (which is a major drawback with common MPM). Together with the main feature as with any mesh-free method is that the boundary does not coincide with the background mesh, these issues leading to significant poor stress history in large-deformation dynamic analysis.

- To improve the accuracy of conventional MPM, the standard viscous boundary and the viscoelastic boundary were implemented into the MPM's framework. Two ways of implementing these conditions have been illustrated and tested with two benchmarks. Results claim the inability to diminish the stress oscillation of the method (i) to impose boundary condition at the surface nodes, and its undesired absorption. The method (ii) with DM-CG method to interpolate the dynamic boundary conditions with GIMP shape functions has shown its impressing result. No stress oscillations occur and the spurious reflection is completely eliminated. The 2D benchmark also demonstrated that the viscoelastic boundary has a better performance than the viscous boundary. Because of the numerical stiffness part intended to simulate the rebound effect for the unbounded domain, the viscoelastic condition does not lead to permanent displacement in case of low-frequency range, which is opposite of the standard viscous boundary. This is not a problem with formal finite element analysis since it commonly deals with small deformation. Rotations and movement of dynamic boundaries are also observed with the benchmark, however, they have not contributed to any major errors.

- It was demonstrated that realistic geotechnical problem could be simulated with the proposed method (ii). A foundation on cohesive soil under repeated load has been studied. It is observed that with the linear elastic von Mises material with the post-softening behaviour, failure mechanisms under the foundation were allowed to develop. Moreover, it can be seen that with repeated dynamic loading, the main failure zone observed was similar to the Prandtl's failure surface, but with some differences in the maximum failure depth and width. Another interesting point is that a few more shear bands started to develop from the main failure surface, however, the primary failure zone leads to failure before these bands could be fully developed. The use of dynamic boundaries also exhibits the numerical artifacts with the fixed boundary in which the spurious reflection of surface waves can lead to a secondary shear band being formed

easier. Finally, it is shown that the transformation between quasi-static stage and dynamic stage works well and could extend the applications of the dynamic boundary conditions to geotechnical examples

6.3. Recommendations

This study, like any other, has limitations, therefore to further develop the accuracy and practical use of the material point method, five recommendations are given below:

- The viscoelastic boundary is a promising solution to represent the radiation at the boundary. Since the boundary is computed related to the distance from the boundary to the excitation source, it is worth to investigate how the boundary behaves in case of rotation of the domain. In this thesis, the boundary was rotated with an angle of rotation smaller than 10° due to large deformation, however no major errors were observed. For simple problems, the use of the viscous boundary is still desirable due to its simplicity.

- Including multi-phase behaviour. This work studies the geotechnical examples and benchmark with a single phase material (i.e. only solid phase). While in reality, the water phase could significantly affect the propagation of waves and thus reduce the ability to absorb the reflections. Moreover, in unsaturated conditions in which water and air phase both play a role, the interaction of waves inside the domain could potentially be affected. However, the viscous and viscoelastic implementations (together with multi-phase modification) could still perform accurately, allowing the waves to be properly transmitted outwards from the domain.

- Since the dynamic boundary conditions are converted to the boundary traction, the material point's support domain plays an important role. However in this thesis, no deformation of the support domain was included due to its complexity. Methods such as the extension of GIMP method, i.e., CPDI, introduced by Sadeghirad et al. (2013) could be a potential solution. Additionally, recent studies have demonstrated that CPDI can be implemented using unstructured meshes, also giving the opportunity of implementing dynamic boundary with DM-G together with unstructured meshes.

- The transformation between analysis stages in this thesis is applicable for geotechnical examples such as: CPT simulation, foundation, pile installation. However, it is needed to have a better transformation method, in order to deal with problem which requires the presence of gravitation during the dynamic analysis such as: soil-structure interactions, earthquakes, landslides. The solution to this could be the combination of the penalty method at the represented boundary, using the B-spline method enhancement as introduced by Bing et al. (2019). Moreover, the cubic B-spline basis function has been proven to have similar efficiencies as GIMP shape function, giving the opportunity to apply the dynamic boundary traction with B-spline method.

- Another promising solution is using the perfectly matched layer (PML) to absorb the spurious reflection. The advantage of this approach is that the PML could be directly modified with the fixed boundary conditions, therefore giving more practical applications with its use. However, implementation of the PML could be potentially complicated as the formulation is not straightforward, and the attenuation region is best organised in the complex plane, which is complicated to apply in MPM.

References

Andersen, S., & Andersen, L. (2010). Analysis of spatial interpolation in the material-point method. *Computers and Structures*, *88*(7), 506–518.

Bardenhagen, S., Brackbill, J., & Sulsky, D. (2000). The material-point method for granular materials. *Computer Methods in Applied Mechanics and Engineering*, *187*(3), 529–541.

Basu, U., & Chopra, A. K. (2004). Perfectly matched layers for transient elastodynamics of unbounded domains. *Numerical Methods in Engineering*, *59*.

Bathe, K. J. (2004). *Finite element procedures*. Prentice Hall, Pearson Education, Inc.

Bhandari, T., Hamad, F., Moormann, C., Sharma, K., & Westrich, B. (2016). Numerical modelling of seismic slope failure using MPM. *Computers and Geotechnics*, *75*, 126–134.

Bing, Y., Cortis, M., Charlton, T., Coombs, W., & Augarde, C. (2019). B-spline based boundary conditions in the material point method. *Computers and Structures*, *212*, 257–274.

Brackbill, J. U. (1986). FLIP: A method for adaptively zoned, particle-in-cell calculations of fluid flows in two dimensions. *Journal of Computational Physics*, *65*.

Brackbill, J., Kothe, D., & Ruppel, H. (1988). FLIP: A low-dissipation, particle-in-cell method for fluid flow. *Computer Physics Communications*, *48*(1), 25–38.

Budhu, M., & Al-Karni, A. (1993). Seismic bearing capacity of soils. *Géotechnique*, *43*(1), 181–187.

Buneman, O. (1959). Dissipation of currents in ionized media. *Phys. Rev.*, *115*, 503–517.

Buzzi, O., Pedroso, D. M., & Giacomini, A. (2008). Caveats on the implementation of the generalized material point method. *Computer Modeling in Engineering and Sciences*, *1*(1), 1–21.

Ceccato, F., Beuth, L., Vermeer, P. A., & Simonini, P. (2016). Two-phase material point method applied to the study of cone penetration. *Computers and Geotechnics*, *80*, 440–452.

Charlton, T., Coombs, W., & Augarde, C. (2017). iGIMP: An implicit generalised interpolation material point method for large deformations. *Computers and Structures*, *190*, 108–125.

Clayton, R., & Engquist, B. (1977). Absorbing boundary conditions for acoustic and elastic wave equations. *Bulletin of the Seismological Society of America*, *67*(6), 1529–1540.

Cohen, M. (1980). *Silent boundary methods for transient wave analysis*. PhD thesis, Canifornia Insitute of Technology.

Davies, A. J. (2011). *The finite element method: An introduction with partial differential equations*. Oxford University Press, Oxford.

Dawson, J. (1962). One-dimensional plasma model. *The Physics of Fluids*, *5*(4), 445–459.

Deeks, A. J., & Randolph, M. F. (1994). Axisymmetric time domain transmitting boundaries. *Journal of Engineering Mechanics*, *120*(1), 25–42.

Deshpande, S., Rawat, S., & Bandewar, N. (2016). Consistent and lumped mass matrices in dynamic and their impacts on finite element analysis. *International Journal of Mechanical Engineering and Technology (IJMET)*, *7*, 135–147.

Drabkin, S., Lacy, H., & Kim, D. S. (1996). Estimating settlement of sand caused by construction vibration. *Journal of Geotechnical Engineering*, *122*(11), 920–928.

François, S., Karg, C., Haegeman, W., & Degrande, G. (2010). A numerical model for foundation settlements due to deformation accumulation in granular soils under repeated small amplitude dynamic loading. *International Journal for Numerical and Analytical Methods in Geomechanics*, *34*(3), 273–296.

Fu, X., Sheng, Q., Zhang, Y., Zhou, Y., & Dai, F. (2015). Boundary setting method for the seismic dynamic response analysis of engineering rock mass structures using the discontinuous deformation analysis method. *International Journal for Numerical and Analytical Methods in Geomechanics*, *39*(15), 1693–1712.

Gonzalez Acosta, J. L. (2020). *Investigation of MPM inaccuracies, contact simulation and robust implementation for geotechnical problems*. PhD Thesis, Delft University of Sciences; technology, The Netherlands.

Gonzalez Acosta, J. L., Vardon, P. J., & Hicks, M. A. (2017). Composite Material Point Method (CMPM) to Improve Stress Recovery for Quasi-static Problems [Proceedings of the 1st International Conference on the Material Point Method (MPM 2017)]. *Procedia Engineering*, *175*, 324–331.

Gonzalez Acosta, J. L., Vardon, P. J., & Hicks, M. A. (2021). Development of an implicit contact technique for the material point method. *Computers and Geotechnics*, *130*, 103859.

Gonzalez Acosta, J. L., Vardon, P. J., Hicks, M. A., & Guido, R. (2020). An investigation of stress inaccuracies and proposed solution in the material point method. *Computational Mechanics*, *65*, 555–581.

Griffiths, D. V. (2004). *Programming the finite element method*. John Wiley & Sons, Ltd.

Guilkey, J. E., Hoying, J. B., & Weiss, J. A. (2006). Computational modeling of multicellular constructs with the material point method. *Journal of Biomechanics*, *39*, 2074–2086.

Guilkey, J. E., & Weiss, J. A. (2003). Implicit time integration for the material point method: Quantitative and algorithmic comparisons with the finite element method. *International Journal for Numerical Methods in Engineering*, *57*(9), 1323–1338.

Harlow, F. H. (1964). The particle-in-cell computing method for fluid dynamics. *Method Computational Physics*, *3*.

Kellezi, L. (2000). Local transmitting boundaries for transient elastic analysis. *Soil Dynamics and Earthquake Engineering*, *19*.

Knappett, J., Haigh, S., & Madabhushi, S. (2006). Mechanisms of failure for shallow foundations under earthquake loading [11th International Conference on Soil Dynamics and Earthquake Engineering (ICSDEE): Part II]. *Soil Dynamics and Earthquake Engineering*, *26*(2), 91–102.

Kontoe, S. (2006). Development of the time integration and advanced boundary conditions for dynamic geotachnical analysis, phd thesis, department of civil and environmental engineering, imperial college of science, technology and medicine.

Liao, Z. P., & Wong, H. L. (1984). A transmitting boundary for the numerical simulation of elastic wave propagation. *International Journal of Soil Dynamics and Earthquake Engineering*, *3*(4), 174–183.

Løkke, A., & Chopra, A. K. (2019). *Direct-Finite-Element Method for Nonlinear Earthquake Analysis of Concrete Dams Including Dam – Water – Foundation Rock Interaction*. University of California, Berkeley.

Lysmer, J., & Kuhlemeyer, R. L. (1969). Finite dynamic model for infinite media. *Journal of the Engineering Mechanics Division*, *95*(4), 859–877.

Meyerhof, G. G. (1951). The ultimate bearing capacity of foudations. *Géotechnique*, *2*(4), 301–332.

Meyerhof, G. G. (1953). Some recent foundation research and its application to design. *The Structural Engineer*, *31*(6), 151–167.

Moghaddas, S., Gh., G. M., & Ahmadi, M. (2011). Experimental and numerical investigation on circular footing subjected to incremental cyclic loads. *International Journal of Civil Engineering*, *9*(4).

Prandtl, L. (1920). Uber die harte plastischer korper. *Nachr. Ges. Wissensch, Gottingen, math. -phys. Klasse, 1920*, 74–85.

Richards, R., Elms, D. G., & Budhu, M. (1993). Seismic bearing capacity and settlements of foundations. *Journal of Geotechnical Engineering*, *119*(4), 662–674.

Sadeghirad, A., Brannon, R. M., & Guilkey, J. E. (2013). Second-order convected particle domain interpolation (cpdi2) with enrichment for weak discontinuities at material interfaces. *International Journal for Numerical Methods in Engineering*, *95*(11), 928–952.

Sadeghirad, A., & Vaziri Astaneh, A. (2011). A finite element method with composite shape functions. *Engineering Computations*, *28*(4), 398–423.

Semblat. (2011). A simple multi-directional absorbing layer method to simulate elastic wave propagation in unbounded domains. *International Journal for Numerical Methods in Engineering*, *85*(12), 1543–1563.

Shinohara, T., Tateishi, T., & Kubo, K. (1960). Bearing capacity of sandy soil for eccerntric and inclined load and lateral resistance of single piles embedded in sandy soil. *Proceeding of 2nd World Conference of Earthquake Engineering in Tokyo*, 265–80.

Smith, W. D. (1974). A non-reflecting plane boundary for wave propagation problems. *Journal of Computational Physics*, *15*(4), 492–503.

Soubra, A. (1997). Seismic bearing capacity of shallow strip footings in seismic conditions. *Proceedings-institution of Civil Engineers Geotechnical Engineering*, 230–241.

Steffen, M., Wallstedt, P. C., Guilkey, J. E., Kirby, R. M., & Berzins, M. (2008). Examination and analysis of implementation choices within the material point method (mpm). *Computer Modelling in Engineering and Sciences*, *31*, 107–127.

Steffen, M., Kirby, R. M., & Berzins, M. (2008). Analysis and reduction of quadrature errors in the material point method (mpm). *International Journal for Numerical Methods in Engineering*, *76*(6), 922–948.

Sulsky, D., Chen, Z., & Schreyer, H. (1994a). A particle method for history-dependent materials. *Computer Methods in Applied Mechanics and Engineering*, *118*(1), 179–196.

Sulsky, D., Chen, Z., & Schreyer, H. (1994b). A particle method for history-dependent materials. *Computer Methods in Applied Mechanics and Engineering*, *118*(1), 179–196.

Sulsky, D., Zhou, S.-J., & Schreyer, H. L. (1995). Application of a particle-in-cell method to solid mechanics [Particle Simulation Methods]. *Computer Physics Communications*, *87*(1), 236–252.

Sulsky, D., Schreyer, H., Peterson, K., Kwok, R., & Coon, M. (2007). Using the material-point method to model sea ice dynamics. *Journal of Geophysical Research: Oceans*, *112*(C2).

Tezaghi. (1925). *Erdbaumechanikauf bodenphysikalischer*. F. Deuticke.

Tielen, R., Wobbes, E., Möller, M., & Beuth, L. (2017). A high order material point method [Proceedings of the 1st International Conference on the Material Point Method (MPM 2017)]. *Procedia Engineering*, *175*, 265–272.

Tono, I., & Yasuda, S. (1981). Liquefaction of the ground during the 1978 miyagiken-oki earthquake. *Journal of the Japanese Geotechnical Society*, *21*(3), 18–34.

Underwood, P. (1981). Doubly asymptotic, boundary-element analysis of dynamic soil-structure interaction. *International Journal of Solids and Structures*, *17*.

Wang, L., Coombs, W. M., Augarde, C. E., Brown, M., Knappett, J., Brennan, A., Richards, D., & Blake, A. (2017). Modelling screwpile installation using the mpm [Proceedings of the 1st International Conference on the Material Point Method (MPM 2017)]. *Procedia Engineering*, *175*, 124–132.

Wang, M. A. H., B., & Vardon, P. J. (2016). Slope failure analysis using the random material point method. *Géotechnique Letters*, *6*(2), 113–118.

Wang, P. J. V., B., Hicks, M. A., & Chen, Z. (2016). Development of an implicit material point method for geotechnical applications. *Computers and Geotechnics*, *71*, 159–167.

Wang, P. J. V., B., & Hicks, M. A. (2016). Investigation of retrogressive and progressive slope failure mechanisms using the material point method. *Computers and Geotechnics*, *78*, 88–98.

Wang, Y., Beom, H. G., Sun, M., & Lin, S. (2011). Numerical simulation of explosive welding using the material point method. *International Journal of Impact Engineering*, *38*(1), 51–60.

Zhang., S. M. X., Lian., Y., & Zhou, X. (2009). Simulation of high explosive explosion using adaptive material point method. *Computer Modelling in Engineering and Sciences*, *39*(2), 101–123.

Zhou, S., Stormont, J., & Chen, Z. (1999). Simulation of geomembrane response to settlement in landfills by using the material point method. *International Journal for Numerical and Analytical Methods in Geomechanics*, *23*(15), 1977–1994.